Doctoral Dissertation

Study of Photoexcited Carriers in Solar Cells Using Terahertz Imaging and Spectroscopy

(テラヘルツ分光およびイメージングを用いた太陽電池の光励起キャリアに関する研究)

Khandoker Abu Salek

July 2015

Graduate School of Engineering
Osaka University, Japan

Preface

Solar cells have attracted much attention due to the increasing energy demands for the future. In order to get higher solar energy conversion efficiency, characterization and inspection techniques that will help in improving device function are very important. In this thesis, we demonstrate the use of terahertz (THz) spectroscopy and imaging as promising techniques for evaluation and inspection of solar cell devices. THz techniques were applied to study the optical properties and the dynamics of photoexcited carriers in silicon and silicon-based solar cells under the illumination of continuous wave (CW) ultraviolet (UV) and near infrared (NIR) light. Parameters such as conductivity, charge carrier density and mobility, and lifetime were examined, without the need of electrical contacts, using terahertz time-domain spectroscopy (THz-TDS). The dynamics of the local photoexcited carriers in solar cell was also studied using laser terahertz emission microscope (LTEM). This thesis consists of the following chapters:

Chapter 1 covers the background, the purpose and the structure of the thesis.

In Chapter 2 we discuss some photovoltaic concepts such as the fundamentals of a *p*–*n* junction, charge carrier generation, recombination mechanisms, and quantum efficiency of solar cell.

In Chapter 3 the THz spectroscopy and imaging systems used in this thesis are explained. THz generation and detection methods are also reviewed and the theoretical concepts needed for the extraction of material parameters from data are introduced.

In Chapter 4 we investigate the optical properties (such as complex refractive index, conductivity, charge carrier density and mobility) of semi-finished single crystalline Si solar cells using transmission THz-TDS. The conductivity was analyzed using the simple Drude model. The mobility of the excess carriers increases nonlinearly with the illumination power and tends to saturate at higher illumination power for NIR laser. This phenomenon was explained by the carrier trapping effect in the impurity region in the bandgap of solar cells. The excess carriers generated by UV light illumination have minimal effect on the measured optical properties of the sample. These results were explained by considering the difference in the penetration depth of NIR and UV light.

In Chapter 5 we investigate the surface recombination velocity (SRV) and carrier lifetime in silicon wafer. The SRV was extracted using the SRH model and we observed that the charge carriers excited by UV illumination significantly changed the SRV by modifying the surface

potential. The dynamics was explained using the energy band diagram for silicon under UV light illumination. The effective lifetime of excess carriers excited by NIR laser was measured under steady state conditions and it was found that it depends on the excess carrier density.

In Chapter 6 we investigate optical properties in high resistivity doped silicon and single crystalline Si solar cell using reflection THz-TDS. The measured reflectance and refractive index of the silicon were in good agreement with reported values. The reflectance (and the refractive index) measured in the front surface of the single crystalline Si solar cell is much higher than that of silicon. In addition, no significant change in the THz reflection was observed for the samples when illuminated by UV and NIR radiation.

In Chapter 7 we present a LTEM study for a polysilicon solar cell. The THz wave emission image directly reflects the electric field distribution in solar cell when illuminated by femtosecond laser. The effects of NIR and UV illumination on the THz wave emission from solar cell were examined under different voltage bias conditions. THz wave emission images showed that the THz emission gradually decreased with increasing illumination power. These changes were explained using the band structure of the illuminated solar cell.

In Chapter 8 we draw out the conclusions based on the findings in this thesis.

Acknowledgements

There are many people whose support and advice made a significant contribution to the completion of this dissertation.

First of all, I would like to express my sincere appreciation to my supervisor, Professor Masayoshi Tonouchi at Institute of Laser Engineering, Osaka University, for his advice, support, and guidance throughout the entire duration of my doctoral research. His encouragement and help made the completion of this work possible. I am also grateful to him for his financial assistant during my time in Japan.

I would like to show my gratitude to Professor Toshimichi Ito at Department of Electrical, Electronic and Information Engineering, Osaka University, for valuable advice and suggestions on this thesis.

I would like to thank Professor Yusuke Mori, Professor Mitsuhiro Katayama, Professor Tetsuya Yagi, Professor Masanori Ozaki, Professor Toshiaki Suhara, Professor Masahiko Kondow, Professor Nobuya Mori, Professor Noriaki Miyanaga and Professor Hiroaki Nishimura for their valuable instructions on my researches.

I am thankful to Associate Professor Hironaru Murakami for his support. I received necessary suggestions from him that helped me enrich my thesis.

I would like to thank Associate Professor Iwao Kawayama for his helpful guidance and encouragement. He has always been ready to discuss matters and answer questions. Without his great support, I could never complete my study.

I would like to thank Mr. Hidetoshi Nakanishi and Mr. Akira Ito of Dainippon Screen Mfg. Co. Ltd. Japan, for their collaboration and for providing solar cell samples measured for this thesis.

A special thank you goes to current post-doctoral researcher Kazunori Serita, former post-doctoral researcher Ryuhei Kinjo, current PhD student Filchito Bagsican, and Mr. Kazuhisa Takayama in Tonouchi Laboratory for taking their time to help me.

Finally, I would also like to thank all members and staffs of Tonouchi Laboratory at Institute of Laser Engineering, Osaka University, for their ongoing help and support.

Table of Contents

Chapter 1: General introduction

Terahertz (THz) technology has been developed from much research in the fields of electronics and photonics over the past three decades. This technology utilizes terahertz waves in the frequency range from 100 GHz to 30 THz and has attracted much attention due to its unique characteristics. THz radiation is non-ionizing, and it can transmit through a wide variety of nonpolar and nonmetallic materials, which make it extremely useful for non-destructive analysis. THz wave is a low photon energy radiation (~several meV), making it useful when dealing with biological samples. Spectroscopic and imaging techniques with THz waves have been developed and applied in various fields, such as medical diagnosis, quality control, security, science, and so on [1-3].

Several novel THz techniques such as terahertz time-domain spectroscopy (THz-TDS) [4], optical pump-THz probe spectroscopy [5], and terahertz emission microscopy [6] have been developed and are widely used for materials characterization. THz-TDS is a powerful, noncontact and nondestructive tool, which is effectively applied in studies of many materials such as semiconductors, dielectrics, liquids, and superconductors [7-9]. In this technique, material properties are probed with short pulses of THz waves. Using the coherent nature of generation and detection of THz pulses, both the amplitude and phase of the THz signal transmitted through a material can be extracted. This information leads one to obtain the material's complex refractive index. Therefore both the complex dielectric constant and the complex conductivity of the material can be calculated [4]. The important properties such as charge carrier density and mobility can be determined by applying the appropriate conductivity model [10]. These properties were successfully characterized using transmission THz-TDS [4, 7, 11]. The transient properties of optically excited semiconducting materials can be studied by using optical pump-THz probe spectroscopic technique [5,12].

Many materials such as liquids and metallic materials are opaque to THz waves, though most of the materials are transparent to THz waves. Also, some materials are optically thick, and therefore THz waves cannot penetrate them. Such materials are studied using reflection THz-TDS [13]. Since optically thick semiconductors and biological materials are opaque in the THz waves, the reflection measurement is suitable for obtaining their optical properties [14].

THz waves can be used for imaging applications. The first imaging system based on THz-TDS

was reported by Hu and Nuss in 1995 [15]. Since then, many imaging techniques were developed by using THz waves. In THz wave imaging, the images are taken by either the THz waves transmitted through or reflected from a sample using THz-TDS. Another attractive tool is laser terahertz emission microscope (LTEM), which shows unique advantages as a material or device imaging [16]. This system has the advantage in spatial resolution over the conventional THz wave imaging, because the spot size of the excitation laser is much smaller than that of THz waves. In this system, the sample itself is the source of THz emission, and the THz emission properties such as amplitude and waveform reflect the nature of the material. This system can detect and image THz wave emissions from various electronic materials such as semiconductors, high-critical-temperature superconductors, or ferroelectric materials when the sample is excited by femtosecond laser [6, 16]. This system was originally developed in our laboratory and demonstrated its capability for detecting defective interconnections in IC chips [17]. The results showed that the image of broken IC chips is different from the normal chips. Recently, Nakanishi et al., applied this technique to study THz emission properties of a polysilicon solar cell [18]. Their results showed that the THz emission image gives the structural information and reflects the dynamics of the local photoexcited carriers.

On the other hand, photovoltaic (PV) technology has attracted much attention due to increasing energy demands for the future [19, 20]. The traditional sources of energy such as fossil fuels are being depleted day by day. The search for efficient and affordable methods for alternative sources of energy is important, and the conversion of solar energy into electrical power via photovoltaic devices is one of the most promising methods. However, the major challenges are to produce solar cells with high efficiency at an economically acceptable price. In order to get more efficient solar cells, much research and development is still required.

A variety of optical methods, such as photoluminescence (PL) [21], electroluminescence (EL) [22], and the laser beam induced current (LBIC) [23] have been adapted for characterizing photovoltaic cells. Most of these methods are designed for large area collection such as entire PV panel imaging. The PL technique is applied to inspect silicon wafers and solar cells. This technique uses a short laser pulse to illuminate the cell, and the PL image of the resulting luminescence is detected using a sensitive camera. The PL image permits the visualization of the minority carrier lifetime and detection of local defects, among other properties. EL is the emission of light due to an applied electrical current by connecting the cell in forward bias. This imaging technique requires electrical contact with the device. Therefore, this technique can be applied for finished solar cell or module only, not for solar cell wafers. A silicon CCD camera is

used to acquire the EL image. This technique can be used for detecting defects and measuring cell uniformity. LBIC is a conventional technique used for measuring the current generated from the solar cell and the cell uniformity by scanning with a laser beam. The major disadvantage of this method is the requirement of electrical contacts, so that this method cannot be applied for the inspection of solar cell wafers. Recently, laser superconducting quantum interference device (SQUID) microscope [24] has been used to inspect the inhomogeneity of a polysilicon solar cell. This technique uses a continuous light focused on the surface of the solar cell to measure the magnetic field induced by the photocurrent. This technique is also applicable for finished solar cells.

The performance of solar cells usually depends on the material quality and on the incident intensity and wavelength of light. Thus, the characterization of materials is of importance for design and fabrication of solar cells. It is also important to inspect finished solar cells to improve and maintain the product quality. In the photovoltaic industry, THz spectroscopic techniques can be applied to characterize solar cells and related materials. Measurements of the wavelength dependence of optical response are particularly important to understand the physical behavior of solar cells. For example, the near infrared (NIR) and ultraviolet (UV) light response are dominated by the charge carrier in the base (*p*-region) and emitter (*n*-region) of the solar cell due to the difference in their penetration depth. Therefore, the optical properties and the carrier dynamics at the surface and/or inside the solar cell can be studied. By using the transmission THz-TDS technique, the optical properties of solar materials or semi-finished solar cells can be studied under light illumination without electrical contacts. Since the finished solar cells are opaque in the THz waves, the optical properties can be determined by using reflection THz-TDS. On the other hand, LTEM can be used to inspect finished solar cells to study the dynamic behavior of photoexcited carriers.

In this thesis, the optical properties and the dynamics of photoexcited carriers in silicon and silicon-based solar cells were studied under continuous-wave (CW) 800 nm (NIR) and 365 nm (UV) light illumination. The photoexcited carriers affect a number of material parameters such as complex refractive index, conductivity, and mobility. The lifetime and surface recombination velocity (SRV) of photoexcited carriers also affects the overall performance of solar cells. Working conditions for the solar cell was simulated by illumination with CW light, and the different material parameters were then examined without the need of electrical contacts using THz-TDS. The dynamics of local photoexcited carriers in solar cell were also inspected under similar working conditions of solar cell using LTEM. A thorough knowledge of wavelength

dependence of the behavior of charge carriers helps to improve the device function to get higher efficiency in solar cells. The aim of this thesis was to explore the use of THz spectroscopy and imaging as promising techniques for the evaluation and inspection of solar cells.

The thesis is consisted of the following chapters:

Chapter 2 reviews the theoretical background for understanding the basic principles of photovoltaic cell. The fundamentals of *p*–*n* junction, charge carrier generation, recombination mechanisms, and the current-voltage characteristics and the quantum efficiency of solar cells are explained.

Chapter 3 describes the fundamentals of THz spectroscopy. The methods of generation and detection of THz radiation are briefly reviewed. The experimental setups for THz-TDS in transmission and reflection mode as well as the novel THz emission imaging tool LTEM used in this thesis are summarized. The theoretical expressions for the extraction of material parameters are introduced.

Chapter 4 gives the transmission THz-TDS study on semi-finished single crystalline Si solar cells. Measurements are carried out on the antireflection-coated and non-coated solar cells during photoexcitation by NIR and UV light. The optical properties are extracted from the time-domain THz transmission data. Drude model is used to analyze conductivity data. The mobility of excess carriers generated by NIR light is found to vary significantly for both samples and is explained by the carrier trapping effect.

Chapter 5 investigates the SRV and minority carrier lifetime in a silicon wafer using similar experimental system and the conditions presented in Chapter 4. The effects of UV illumination on SRV in silicon surface are observed and the results are explained with the energy band diagram of the silicon. The effective lifetime of excess carriers generated by NIR light is calculated under steady state conditions, and it is observed that the lifetime depends on the excess carrier density.

Chapter 6 describes a THz reflection measurement for a high resistivity doped silicon wafer and a single crystalline Si solar cell using reflection THz-TDS. The experiments are done with a special movable sample holder, which allowed the measurement of reflected THz waves with almost no phase error. The data analysis procedure and optical constants calculation are presented. The experimental results of spectroscopic and imaging are also included.

Chapter 7 performs a LTEM study on a polysilicon solar cell. LTEM is used to visualize THz wave emission from the solar cell sample when illuminated by femtosecond laser. The effects of NIR and UV illumination on the THz wave emission from the solar cell are examined under reverse bias and zero bias. The reduction of THz emission from the solar cell is observed due to the photoexcited carriers generated by NIR or UV light, and the results are explained using the energy band diagram of the illuminated solar cell. At higher excitation laser (femtosecond laser) power the screening of the electric field in the *p*–*n* junction of the solar cell is observed.

Finally, Chapter 8 provides conclusions of this thesis.

References

1. M. Tonouchi. “Cutting-edge terahertz technology,” *Nat. Photonics*, **1**, 97 (2007).
2. B. Ferguson & X-C Zhang, Materials for terahertz science and technology. *Nat. Mater.*, **1**, 26 (2002).
3. A. Y. Pawar, D. D.Sonawane, K. B. Erande and D. V. Derle, “Terahertz technology and its applications,” *Drug Invention Today*, **5**, 157 (2013).
4. M. van Exter and D. Grischkowsky, “Optical and electronic properties of doped silicon from 0.1 to 2 THz”, *Appl. Phys. Lett*., **56**, 1694 (1990).
5. M. C. Beard, G. M. Turner and C. A. Schmuttenmaer, “Transient photoconductivity in GaAs as measured by time-resolved terahertz spectroscopy,” *Phys. Rev. B*, **62**, 15764 (2000).
6. M. Yamashita, C. Otani, T. Matsumoto, Y. Midoh, K. Miura, K. Nakamae, K. Nikawa, S. Kim, H. Murakami and M. Tonouchi, “Terahertz emission characteristics from p/n junctions with metal lines under non-bias conditions for LSI failure analysis,” *Opt. Express*, **19**, 10864 (2011).
7. D. Grischkowsky, S. Keiding, M. Exter, and C. Fattinger, “Far-infrared time-domain spectroscopy with terahertz beams of dielectrics and semiconductors,” *J. Opt. Soc. Am. B*, **7**, 2006 (1990).
8. J. E. Pedersen and S. R. Keiding, “THz time-domain spectroscopy of nonpolar liquids,” *IEEE J. Quant. Electron.*, **28**, 2518 (1992).
9. M. C. Nuss, K. W. Goossen, J. P. Gordon, P. M. Mankiewich, M. L. O’Malley, and M. Bhushan, “Terahertz time-domain measurement of the conductivity and superconducting band gap in niobium,” *J. Appl. Phys.*, **70**, 2238 (1991).
10. R. Ulbricht, E. Hendry, J. Shan, T. F. Heinz and M. Bonn, “Carrier dynamics in semiconductors studied with time-resolved terahertz spectroscopy,” *Rev. Mod. Phys.*, **83**, 543 (2011).
11. C. Zhang, B. Jin, J. Chen, P. Wu and M. Tonouchi, “Noncontact evaluation of nondoped InP wafers by terahertz time-domain spectroscopy,” *J. Opt. Soc. Am. B*, **26**, A1-A5 (2009).
12. J. H. Strait, P. A. George, M. Levendorf, M. Blood-Forsythe, F. Rana, and J. Park, “Measurements of the carrier dynamics and terahertz response of oriented germanium nanowires using optical-pump terahertz-probe spectroscopy,” *Nano Lett.*, **9**, 2967 (2009).
13. S. Nashima, O. Morikawa, K. Takata, and M. Hangyo, “Measurement of optical properties of highly doped silicon by terahertz time-domain reflection spectroscopy,” *Appl. Phys. Lett*., **79**, 3923 (2001).

14. T. Jeon and D. Grischkowsky, “Characterization of optically dense, doped semiconductors by reflection THz time domain spectroscopy,” *Appl. Phys. Lett.*, **72**, 3032 (1998).

15. B. B. Hu and M. C. Nuss, “Imaging with terahertz waves,” *Opt. Lett.*, **20**, 1716 (1995).
16. H. Murakami and M. Tonouchi, “Laser terahertz emission microscopy,” *C. R. Phys.*, **9**, 169 (2008).
17. T. Kiwa, M. Tonouchi, M. Yamashita and K. Kawase, “Laser terahertz-emission microscope for inspecting electrical faults in integrated circuits,” *Opt. Lett.*, **28**, 2058 (2003).
18. H. Nakanishi, S. Fujiwara, K. Takayama, I. Kawayama, H. Murakami, M. Tonouchi, “Imaging of a polycrystalline silicon solar cell using a laser terahertz emission microscope,” *Appl. Phys. Express*, **5**, 112301 (2012).
19. P. C. Choubey, A. Oudhia and R. Dewangan, “A review: Solar cell current scenario and future trends,” *Recent Res. Sci. Technol.*, **4**, 99 (2012).
20. F. Dinçer, “The analysis on photovoltaic electricity generation status, potential and policies of the leading countries in solar energy,” *Renew. Sust. Energ. Rev.*, **15**, 713 (2011).
21. T. Trupke, B. Mitchell, J. W. Weber, W. McMillan, R. A. Bardos, R. Kroeze, “Photoluminescence imaging for photovoltaic applications,” *Energy Procedia*, **15**, 135 (2012).
22. T. Fuyuki and A. Kitiyanan, “Photographic diagnosis of crystalline silicon solar cells utilizing electroluminescence,” *Appl. Phys. A*, **96**, 189 (2009).
23. N. M. Thantsha, E. Q. B. Macabebe, F. J. Vorster, E. E. Van Dyk, “Opto-electronic analysis of silicon solar cells by LBIC investigations and current-voltage characterization,” *Physica B*, **404**, 4445 (2009).
24. Y. Nakatani, T. Hayashi, H. Itozaki, “Observation of polycrystalline solar cell using a laser-SQUID microscope,” *IEEE Trans. Appl. Supercond.*, **21**, 416 (2011).

Chapter 2: Fundamentals of photovoltaics

2.1 Introduction

Photovoltaic (PV) cells convert sunlight directly into electricity. The conversion process is based on the photovoltaic effect discovered by Alexander Becquerel in 1839 [1]. The photovoltaic effect describes the release of charge carriers in a semiconductor when light illuminates its surface. The first modern inorganic solar cell was built by Bell Laboratories in 1954 [2]. It was based on silicon and had an energy conversion efficiency of around 6%. Over the years efficiency has reached 25% for crystalline silicon solar cells [3]. There are many different types of materials are used for solar cell fabrication, the more traditional one is crystalline silicon. Generally, single crystalline Si solar cells have the highest efficiency than non-silicon based solar cells [4]. The other types of solar cells are thin film solar cells. They are made from layers of semiconductor materials such as amorphous silicon, cadmium telluride (CdTe), and copper indium gallium selenide (CIGS) only a few micrometers thick [5]. These are cheaper but the efficiency (10~20%) of the cells is lower than that of silicon-based solar cells [4]. Solar cells are also made from variety of new materials besides silicon, including nanotubes, silicon wires, organic dyes, and conductive plastics. Most of the works on these solar cells are being done in the laboratory. Another important structure of solar cell is multi-layer cells, where each layer will utilize light with different wavelengths; in this way, we can get cells with a higher efficiency. The efficiency of three layer cells (InGaP/GaAs/InGaAs) is about 40% [6].

Among the different types and concepts of solar cells, silicon solar cells are still the most popular and efficient. They comprise more than 85% of the PV market today. There are two main types in silicon solar cells: single-crystalline and polycrystalline. Single crystalline solar cells are made from a single crystal and have the highest efficiency but are the most expensive. Polycrystalline cells are made from many crystals and are more cost effective but less efficient. It typically contains a large impurity density, and crystal defects occur at the grain boundaries that act as recombination centers. The grain boundaries reduce the effective diffusion length and thus carriers recombine before they can reach the contact. Today the most efficient single crystalline solar cells have reached efficiencies up to 25%, while commercially available poly silicon solar cells have efficiencies about 20% under the global AM1.5 spectrum (1000W/m^2) [4]. The main factor affecting this efficiency is the fact that photons with energies below the band gap energy cannot contribute energy conversion. Likewise, energy in excess of the band

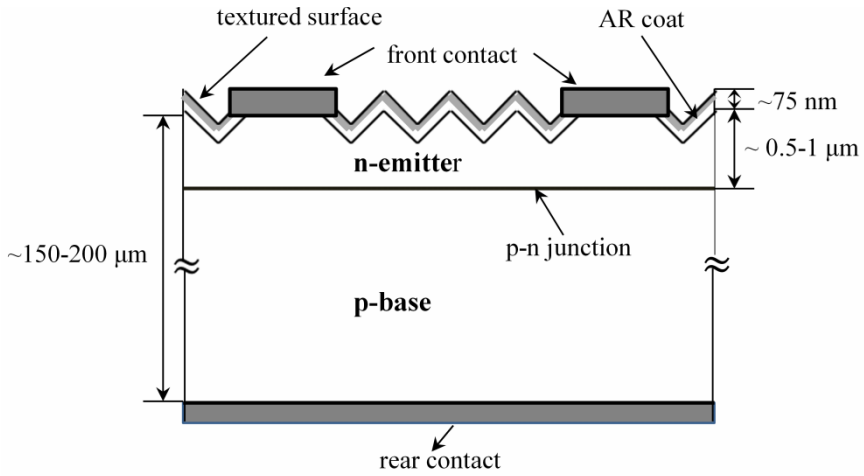

Figure 2.1: Schematic of a crystalline single junction solar cell with p-base and n-emitter on the front side.

gap is usually lost as heat by phonon absorption. It is also important to reduce the reflectance on the front surface of the solar cell. Another key factor in solar cell efficiency is the recombination of electrons and holes before charge carriers are transported to the external circuit.

The operating principle of crystalline solar cells lies in the *p*–*n* junction, which generates an electric field that enables the charge carriers photo-converted in the semiconductor to be collected by the metallic contacts as electrical current. The schematic structure of a crystalline single junction solar cell is illustrated in Fig. 2.1. The aim of this chapter is to briefly discuss the fundamental principle properties of crystalline solar cell. Details can be found in the literature [7, 8].

2.2 The *p*-*n* homojunction under dark conditions

The traditional solar cell is made from a *p*–*n* junction formed by joining *p*-type and *n*-type semiconductors together in very close contact. When the junction is formed, the majority charge carriers from both doped sides diffuse from the higher concentration area to the lower concentration area. The electrons near the *p*–*n* interface to diffuse from the *n* region to the *p* region, and holes to diffuse from the *p* region to the *n* region. Thus, a layer of net negative charge on the *p* region and net positive charge on the *n* region is formed. Together these two charge regions called depletion layer or space charge region. The depletion layer therefore creates an electric field directed from positive charge to negative charge. On both outsides of the space charge region the *n* and *p* semiconductor remains quasi-neutral. The Fermi level of the *n* region and *p* region equals at thermal equilibrium. This produces a band bending of conduction and valence band-edge energies (E_C and E_V), and a potential difference called built-in voltage or diffusion voltage (V_D). This situation is shown in Fig. 2.2.

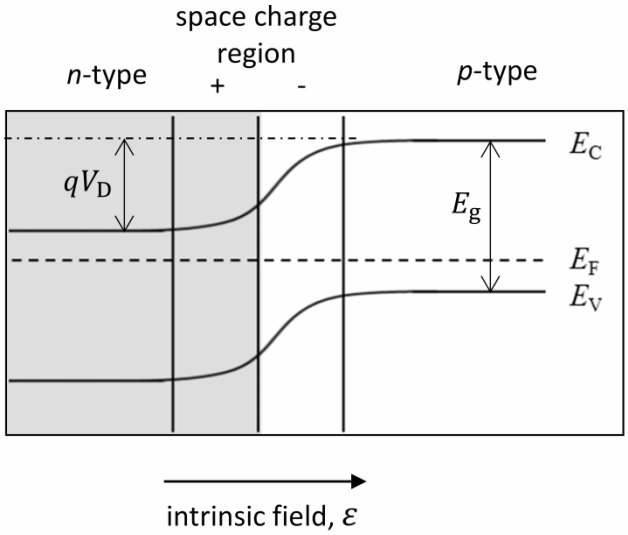

Figure 2.2: Energy band diagram of a *p*–*n* homojunction under equilibrium

The diffusion voltage can be expressed as follows [8]:

$$V_D = \frac{k_B T}{q} \ln \frac{N_A N_D}{n_i^2}, \tag{2.1}$$

where N_D and N_A are the donor and acceptor concentrations in the *n* region and *p* region, respectively, k_B is the Boltzmann constant, *T* is the temperature, and n_i is the intrinsic carrier concentration.

At the thermal equilibrium in an intrinsic semiconductor, we have $n = p = n_i$, and then the intrinsic carrier density is:

$$np = n_i^2 = N_C N_V \exp\left(\frac{E_V - E_C}{k_B T}\right)$$

$$= N_C N_V \exp\left(-\frac{E_g}{k_B T}\right), \tag{2.2}$$

where E_g is the bandgap energy, and N_C and N_V are the effective densities of states in the conduction and valence band, respectively.

The *p*–*n* junction is a diode. The current flow through a diode as a function of applied voltage *V* can be written as:

$$J = J_o \left(\exp\left(\frac{qV}{k_B T}\right) - 1\right) \tag{2.3}$$

This is the diode equation, where J_o is the saturation-current density of the *p*–*n* junction which is written as:

$$J_{\mathrm{o}} = q n_{\mathrm{i}}^2 \left(\frac{D_n}{N_{\mathrm{A}} L_n} + \frac{D_p}{N_{\mathrm{D}} L_p} \right), \tag{2.4}$$

where D_n and D_p are the diffusion coefficient of electrons and holes, respectively, and L_n and L_p are the diffusion lengths of electrons and holes, respectively given as:

$$L_n = \sqrt{D_n \tau_n} \tag{2.5}$$

$$L_p = \sqrt{D_p \tau_p} \tag{2.6}$$

where τ_n and τ_p are the lifetimes of electrons and holes, respectively.

2.3 The *p*-*n* homojunction under illumination conditions

Figure 2.3 shows the energy band diagram of a *p*–*n* homojunction solar cell under light illumination. When a *p*–*n* junction is illuminated by light, electron-hole pairs are generated in the semiconductor. The concentration of minority carriers strongly increases. The generated electrons and holes then diffuse to the junction and are swept away by the electric field. Thus the charge separation is achieved, and a voltage difference can build up between the *p* region and the *n* region. When a load is connected between the electrodes of the illuminated *p*–*n* junction, the photo-generated current will flow through the external circuit. The current density corresponding to the generation of carriers is the illumination current density J_{ph}. Then, the current density in the solar cell can be expressed as follows:

$$J = J_{\mathrm{o}} \left[\exp\left(\frac{qV}{k_{\mathrm{B}} T} \right) - 1 \right] - J_{\mathrm{ph}} , \tag{2.7}$$

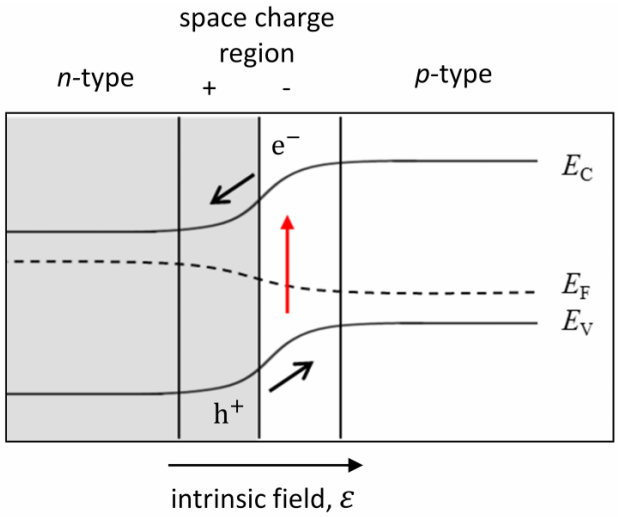

Figure 2.3: Energy band diagram of a *p*–*n* homojunction under light illumination

where J_{ph} is the photo-current given by:

$$J_{\mathrm{ph}} = qG\left(L_n + W + L_p\right) \ , \tag{2.8}$$

where G is the carrier generation rate ($\mathrm{cm^{-3}s^{-1}}$) and W is the space charge region width. Only the carriers generated in the depletion region and in the regions up to the minority carrier diffusion length from the depletion region can contribute to the photo-generated current.

2.4 Current-voltage characteristics

The current-voltage (J–V) characteristic is the most important property in order to characterize a solar cell. The main characteristic properties are short-circuit current J_{SC}, the open circuit voltage V_{OC}, the peak power P_{m}, and the fill factor (*FF*). These parameters are obtained from the J–V curve of a solar cell taken under illumination, as shown in Fig. 2.4. The energy conversion efficiency η can be obtained from these properties.

– Short circuit current J_{SC}: When the solar cell is short circuited (the voltage across the solar cell is zero), the current through the solar cell is the short circuit current. In an ideal case, J_{SC} is equal to the photo-generated current density, J_{ph}, following the equation (2.7).

– Open circuit voltage V_{OC}: When the current through the solar cell is zero, the maximum voltage that is obtained is the open circuit voltage. Setting $J = 0$ in Eq. (2.7) we obtained the open-circuit voltage:

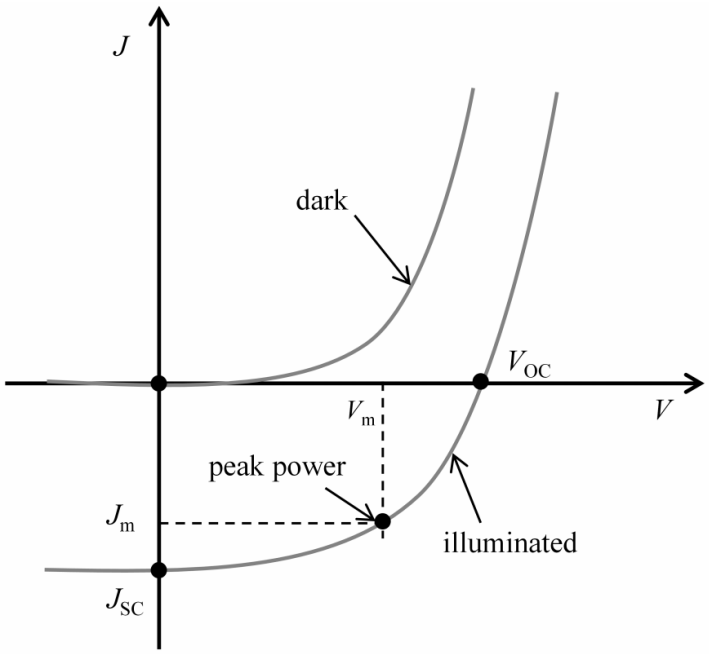

Figure 2.4: Typical J–V characteristics of a p–n junction in the dark and under illumination

$$V_{OC} = \frac{k_B T}{q} \ln\left(\frac{J_{ph}}{J_o} + 1\right), \tag{2.9}$$

This equation shows that V_{OC} depends on the saturation current of the solar cell and the photo-generated current. The saturation current is related to the recombination phenomenon in the solar cell. Then, V_{OC} depends on the recombination in the device.

– Maximum power point: It is the point of the curve where the power reaches its maximum value. At this point J_m and V_m are the corresponding current and voltage values, respectively.

– Fill factor *FF*: The fill factor is defined as the ratio between the maximum power ($P_m = J_m V_m$) generated by the solar cell and the product of J_{SC} and V_{OC}.

$$FF = \frac{J_m V_m}{J_{SC} V_{OC}} \tag{2.10}$$

In case that the solar cell behaves as an ideal diode the fill factor can be expressed approximately as a function of open circuit voltage [7]:

$$FF \equiv \frac{v_{OC} - \ln(v_{OC} + 0.72)}{v_{OC} + 1}, \tag{2.11}$$

where $v_{OC} = V_{OC} . q/(k_B T)$ is a normalized voltage. For an ideal solar cell *FF* = 1, but this is never achieved in practice.

– Efficiency η: The performance of solar cell is determined by the efficiency. Efficiency is defined as the ratio between the generated maximum power and the incident power, P_{in}:

$$\eta = \frac{J_m V_m}{P_{in}} = \frac{FF J_{SC} V_{OC}}{P_{in}} \tag{2.12}$$

Energy conversion efficiency of a crystalline silicon solar cell lies in the range of 20 to 25% [4].

2.5 Quantum efficiency and spectral response

Solar cells can also be characterized through their external quantum efficiency as a function of the wavelength of the incident light. For a solar cell, the ratio between the number of carriers collected by the solar cell and the number of photons incident on the solar cell gives quantum efficiency (QE). There are two types of QE: internal quantum efficiency (IQE) and external quantum efficiency (EQE). IQE of a silicon solar cell can be calculated from the incident photons that are not lost during reflection and transmission from the solar cells and generate collectable carriers. EQE can be calculated from the incident photons that remain after

transmission and reflection. The EQE includes the total number of incoming photons, and is given by [9]:

$$EQE = \frac{number\ of\ collected\ carriers}{number\ of\ incoming\ photons} \tag{2.13}$$

If the effect of the front reflectance R is subtracted, the internal quantum efficiency IQE can be defined as:

$$IQE(\lambda) = \frac{EQE(\lambda)}{1 - R(\lambda)} \tag{2.14}$$

Quantum efficiency depends on the material quality, the intensity, and the wavelength of light. If all photons of a certain wavelength are absorbed and all carriers are collected by the solar cell, then the QE at that wavelength is unity. However, the EQE for most solar cells is reduced because of the effects of recombination where charge carriers are not able to move an external circuit.

The *spectral response* for a solar cell is very similar to the quantum efficiency. The spectral response is defined as the ratio of the photo-current generated by a solar cell under illumination of a given wavelength to the power of the incident light on the solar cell at the same wavelength. The spectral response can be written in terms of the quantum efficiency as [9]:

$$SR(\lambda) = \frac{q\lambda}{hc} QE(\lambda) = 0.808.\lambda.QE(\lambda) \tag{2.15}$$

where SR is the spectral response in A/W, q is the charge, λ is the wavelength in μm, h is the Planck's constant, and c is the speed of light. SR in (2.15) can be either internal or external, depending which value is used for the quantum efficiency.

2.6 Light absorption and carrier generation rate

When photons strike a surface of a semiconductor, they can be absorbed, reflected, or transmitted through the material. For photovoltaic devices, reflection and transmission are typically considered loss mechanisms (photons that are not absorbed do not contribute to the operation of the devices). An absorbed photon excites an electron from the valence band to the conduction band. Photons can only be absorbed if their energy is greater than the band gap energy of the semiconductor. As the photon is absorbed in the material, electron-hole pairs are generated. An absorbing material has a complex index of refraction which can be written as $\tilde{n} = n + i\kappa$, where n and κ are the refractive index and the extinction coefficient of the

semiconductor. The fraction of light reflected from the surface can be written as [3]:

$$R = \left|\frac{\tilde{n}-1}{\tilde{n}+1}\right|^2 = \frac{(n-1)^2+\kappa^2}{(n+1)^2+\kappa^2} \tag{2.16}$$

For crystalline silicon, over 30% of the incident light is reflected. In order to obtain efficient solar cells, antireflection coating and other techniques are applied to reduce the reflection in solar cells.

The extinction coefficient κ is related to the absorption coefficient by:

$$\alpha = \frac{2\omega\kappa}{c} = \frac{4\pi\kappa}{\lambda} \tag{2.17}$$

Here α is the absorption coefficient and λ is the wavelength. Photons with different wavelengths are absorbed in different depths from the surface in the material. The absorption depth for a material is photon-energy dependent, and is defined as simply the inverse of the absorption coefficient.

Generation is an important parameter in the solar cell operation. The generation rate is related to the absorption of photons in the material and quantifies the number of electron-hole pairs. As the light enters and travels through the semiconductor, the intensity of light in the device can be calculated according to the equation:

$$I = I_o e^{-\alpha x} \tag{2.18}$$

where I_o is the light intensity at the top surface of the semiconductor and x is the distance from the surface to the depth at which the intensity of light is calculated.

Since the photons are absorbed, the intensity of light decreases and electron-hole pairs are generated. Therefore, the change in light intensity through the material gives the generation rate. The generation rate at any point in the material can be determined by differentiating the Eq. (2.18). Thus, the generation rate, *G*, is given by [10]:

$$G = \alpha\Phi e^{-\alpha x} \tag{2.19}$$

Here Φ is the photon flux at the surface. The generation rate is different with different wavelength of light.

2.7 Recombination in solar cell

As a typical case recombination is a process in which an electron falls from the conduction band to the valence band, and thereby eliminating a valence band hole. The recombination process negatively affects the obtained current and the voltage of the solar cell, and thereby the efficiency will decrease. Thus the recombination processes should be reduced. There are three main recombination mechanisms that occur in semiconductor. The recombination mechanisms

(Figs. 2.5) are the following: Radiative recombination, Auger recombination, and recombination via defects. These mechanisms are shortly explained here, but their fundamentals are described in detail in the literature [7, 8].

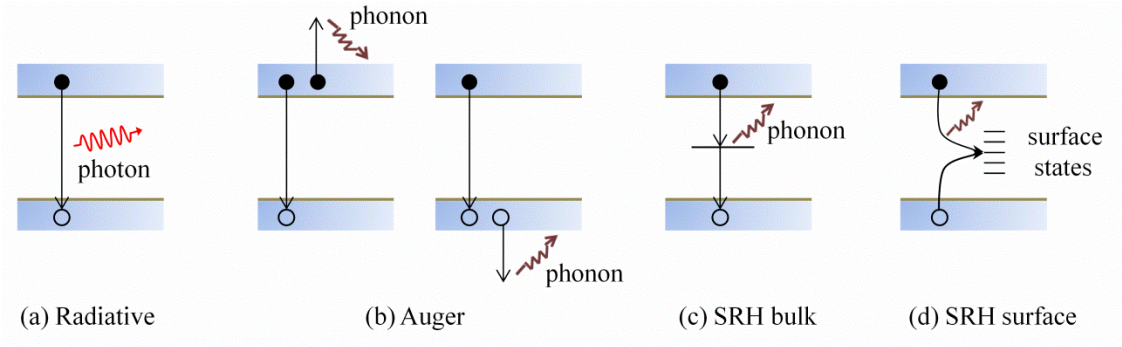

Figure 2.5: (a) Recombination mechanisms in semiconductors (a) Radiative recombination, (b) Auger recombination, (c) SRH bulk and (d) SRH surface.

2.7.1 Radiative recombination

In the radiative recombination process, an electron from the conduction band relaxes to the valence band, emitting a photon with energy close to the bandgap energy as shown in Fig. 2.5(a). It is the inverse process to optical generation. The net recombination rate due to radiative process is given by [8]:

$$U_{\mathrm{rad}} = B\left(pn - n_{\mathrm{i}}^2\right), \tag{2.20}$$

where B is the coefficient of radiative recombination which is carrier density independent and is a property of the material. Inserting non-equilibrium concentration $n = n_{\mathrm{o}} + \Delta n$ and $p = p_{\mathrm{o}} + \Delta p$ in Eq. (2.20) and assuming charge neutrality ($\Delta n = \Delta p$), the radiative recombination rate can be written in terms of radiative recombination lifetime, τ_{rad}:

$$U_{\mathrm{rad}} = B(n_{\mathrm{o}} + p_{\mathrm{o}})\Delta n + B\Delta n^2 \tag{2.21}$$

$$\tau_{\mathrm{rad}} \cong \frac{1}{B(n_{\mathrm{o}} + p_{\mathrm{o}}) + B\Delta n} \tag{2.22}$$

Radiative recombination is common in direct bandgap semiconductors. It is considered to be small or even negligible, compared to other recombination processes in indirect semiconductors. However, most solar cells are made up of silicon, which has an indirect band gap. Therefore, radiative recombination is very low in silicon solar cells.

2.7.2 Auger recombination

In Auger recombination mechanism, three carriers are involved. In this process, as a conduction band electron and a valence band hole recombine, the emitted energy is given to a third carrier in either the conduction band or the valence band, as illustrated in Fig. 2.5(b). The electron (or hole) then relaxes, and the excess energy is given up as heat. The net recombination rate due to Auger processes is given by:

$$U_{\text{Auger}} = \left(C_n n + C_p p\right)\left(pn - n_{\text{i}}^2\right), \tag{2.23}$$

where C_p is the Auger coefficient for holes and C_n for electrons. Auger recombination is dominant in low band gap materials with high carrier densities [11].

2.7.3 Recombination via defects

The presence of defects in a semiconductor crystal due to impurities or crystallographic imperfections such as dislocations produces discrete energy level within the bandgap. These defect levels are also known as traps. The recombination occurs through a two-step process, whereby a free electron from the conduction band first relaxes to the defect level and then electron can recombine with a hole at a defect. Typically trap states located in the middle of the band gap acts as a recombination centers. The recombination process via defect level is shown in Fig. 2.5(c). The dynamics of this recombination process was first analyzed by Shockley, Read, and Hall (SRH) [12]. The net recombination rate per unit volume per time through a single level trap given by:

$$U_{\text{SRH}} = \frac{np - n_{\text{i}}^2}{\tau_p(n + n_1) + \tau_n(p + p_1)}, \tag{2.24}$$

where τ_p, τ_n p_1 and n_1 are defined as

$$\tau_p \equiv \frac{1}{\sigma_p v_{\text{th}} N_{\text{t}}}; \quad \tau_n \equiv \frac{1}{\sigma_n v_{\text{th}} N_{\text{t}}} \tag{2.25}$$

$$p_1 = n_{\text{i}} \exp\left(\frac{E_i - E_T}{kT}\right); \quad n_1 = n_{\text{i}} \exp\left(\frac{E_T - E_i}{kT}\right) \tag{2.26}$$

where v_{th} is the thermal velocity of the carriers, N_{t} is the density of traps and the capture cross-sections, σ_p for holes and σ_n for electrons. The SRH lifetime is given by:

$$\tau_{\mathrm{SRH}} = \frac{\tau_p(n_{\mathrm{o}} + n_1 + \Delta n) + \tau_n(p_{\mathrm{o}} + p_1 + \Delta p)}{p_{\mathrm{o}} + n_{\mathrm{o}} + \Delta n} \tag{2.27}$$

The carrier lifetime associated with SRH mechanism depends on the density of traps. In solar cells, the SRH recombination centers are produced by the defects and impurities in the bulk and in the surface. The SRH recombination is proportional to the defect density.

2.7.4 Surface carrier recombination

Recombination at surfaces or interfaces is often enhanced relative to the bulk due to the presence of crystalline defects and impurities which act as trapping centers. Loss of carriers by recombination at surface reduces operating efficiencies of semiconductor solar cells. A surface is usually characterized by a parameter called surface recombination velocity. Surface recombination via defect levels is also described by SRH theory [13], and the recombination rate at the surface is given by:

$$U_{\mathrm{s}} = \sigma v_{\mathrm{th}} N_{\mathrm{st}} \frac{p_{\mathrm{s}} n_{\mathrm{s}} - n_{\mathrm{i}}^2}{n_{\mathrm{s}} + p_{\mathrm{s}} + 2n_{\mathrm{i}}} \tag{2.28}$$

where n_{s} and p_{s} denote the electron and hole density at the surface, n_{i} is the intrinsic carrier density, σ is the carrier capture cross section, v_{th} is the thermal velocity of carriers, and N_{st} is the density of the recombination centers per unit surface area.

The flux of minority carriers reaching the surface equals to surface recombination rate, U_{s}. For an example of a *p*-type semiconductor, we obtain [13]:

$$U_{\mathrm{s}} = D_n \frac{\partial n_p}{\partial x}\bigg|_{x=x_d} = \sigma v_{\mathrm{th}} N_{\mathrm{st}} \frac{N_{\mathrm{A}}}{n_{\mathrm{s}} + p_{\mathrm{s}} + 2n_{\mathrm{i}}} \left[n_p(x_d) - n_{p\mathrm{o}}\right], \tag{2.29}$$

$$\text{where } S = \sigma v_{\mathrm{th}} N_{\mathrm{st}} \frac{N_{\mathrm{A}}}{n_{\mathrm{s}} + p_{\mathrm{s}} + 2n_{\mathrm{i}}} \tag{2.30}$$

is the surface recombination velocity (SRV) in cms^{-1}. Here, N_{A} is the acceptor concentration, D_n is the diffusion coefficient of electrons, $n_{p\mathrm{o}}$ is the equilibrium minority carrier concentration, and $n_p(x_d)$ is the minority carrier concentration at a distance x_d from the actual surface. SRV is a complicated process because it depends not only on the density of surface states but also on the doping density and the surface charge density n_{s} and p_{s}, and it also depends on the individual treatment at the surface. In solar cell, surface recombination losses are reduced by passivating the surface using dielectric films.

2.8 Summary

In this chapter, a general overview of solar cell physics principles is given. The principle properties of crystalline solar cell, such as *p*–*n* junction, current-voltage characteristics, charge carrier generation, and recombination as well as quantum efficiency have been discussed. The recombination includes bulk process such as Auger recombination and radiative recombination, and the processes involving recombination through defects both within the bulk of the semiconductor and at its surface have also been discussed.

References

1. A.E. Becquerel, *Compt. Rend. Acad. Sci*. **9**, 561 (1839).
2. D. M Chapin, C. S. Fuller, and G. L. Pearson, "A new silicon pn junction photocell for converting solar radiation into electrical power," *J. Appl. Phys*., **25**, 676 (1954).
3. M. Grundmann, *The physics of semiconductors*, Second edition, Berlin: Springer (2010).
4. M. A. Green, K. Emery, Y. Hishikawa, W. Warta and E. D. Dunlop, "Solar cell efficiency tables (version 41)," *Prog. Photovolt: Res. Appl.*, **21**, 1 (2013).
5. K. L Chopra, P. D. Paulson and V. Dutta, "Thin-film solar cells: An overview," *Prog. Photovolt: Res. Appl.*, **12**, 69 (2004).
6. M. A. Green, K. Emery, Y. Hishikawa, W. Warta and E. D. Dunlop, "Solar cell efficiency tables (version 44)," *Prog. Photovolt: Res. Appl.*, **22**, 701 (2014).
7. A. Luque and S. Hegedus, *Handbook of Photovoltaic Science and Engineering*, 2nd edition, Ch. 3, England: John Wiley & Sons (2003).
8. J. Nelson, *The physics of solar cells*, London: Imperial College Press (2003).
9. T. Markvart and L. Castaner, "Principles of solar cell Operation," *Practical Handbook of Photovoltaic*, Chapter IA-1, Amsterdam: Elsevier (2005).
10. S.M. Sze, *Physics of Semiconductor Devices*, 3nd edition, p.726, J. Wiley & Sons (1981).
11. A. Richter, F. Werner, A. Cuevas, J. Schmidt, and S. W. Glunz, "Improved parameterization of Auger recombination in silicon," *Energy Procedia*, **27**, 88 (2012).
12. R. N. Hall, "Electron-Hole recombination in Germanium," *Phys. Rev.*, **87**, 387 (1952).
13. A. S. Grove, *Physics and Technology of Semiconductor Devices*, Chapter 5, New York: J. Wiley & Sons (1962).

Chapter 3: Terahertz experimental techniques and analysis

3.1 Introduction

Terahertz (THz) electromagnetic waves lie between the microwave and infrared regions in the electromagnetic spectrum, as shown in Fig. 3.1. The THz region covers the frequency region from 0.1 to 30 THz. A frequency of 10^{12} Hz or 1 THz corresponds to a wavelength of 300 μm and a period of 1 ps [1]. The frequency range is sometimes called the far infrared or sub-millimeter wave region. So far, the frequency range was known as 'THz gap' due to the difficulties in generation and detection of THz radiation. However, this gap has been filled up over the past two decades. THz technology is now a very attractive research area in many fields. THz waves have some interesting characteristic properties. A number of materials such as semiconductor and dielectric reveal attractive properties at THz frequencies. This allows THz waves ideal for characterizing of these materials. THz waves can transmit through various types of materials including paper, plastics, ceramics, wood, and textiles. Thus, THz waves enable non-destructive analysis of hidden internal substances. THz radiation is non-ionizing, which makes it useful for non-destructive and non-evasive imaging. THz wave is low photon energy radiation and has no harmful influence on biological tissues. Due to these described characteristics, THz radiation has many potential applications in various research field such as communication, security, medical, inspection, and science [2, 3].

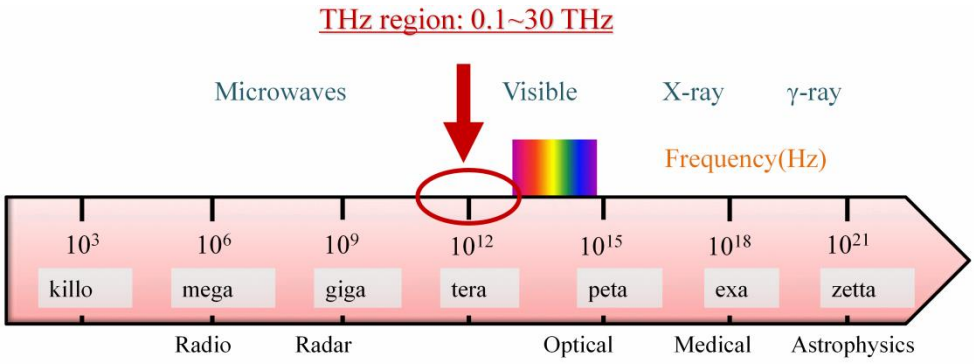

Figure 3.1: THz region in the electromagnetic spectrum [1]

Because of the wide range of applications, many different concepts have been developed for generating and detecting THz radiation. In THz spectroscopic systems, photoconductive antenna switches and semiconductor wafers are used for THz generation, and photoconductive antenna

is employed for THz detection. This technique uses ultra-short pulsed lasers. These lasers are very useful to study ultrafast phenomenon in a sub-picosecond time scale. Ultra-short pulsed laser have short durations (order of a picosecond or less). This property makes the intensity of the peak considerably high since all the energy of the optical pulse is focused on a short time period. Then, these short and high intensity pulses result in the change of the optical properties of the material.

I will now discuss some details of the THz pulse generation and detection methods and the data analysis procedures. I will also introduce experimental THz spectroscopy and imaging systems for the work in this thesis.

3.2 Generation of THz pulses

By employing femtosecond lasers, several methods for generating THz radiation are developed, such as photoconductive antenna [4,5], optical rectification, and semiconductor surface emission [5]. At present, two kinds of THz detecting methods are commonly used. One is for the photoconductive detection and the other is for electro-optic sampling [5].

3.2.1 THz generation from photoconductive antennas

The most common method of THz generation is to use photoconductive (PC) antenna in the terahertz time-domain spectroscopy (THz-TDS) system. A PC antenna is an electrical switch based on a semiconductor that shows a rapid and large electrical conductivity when exposed to light. The photon energy should be (slightly) greater than the bandgap of the semiconductor material. Figure 3.2 schematically illustrates THz pulse emission from a THz emitter structure commonly used. The PC switch is made of ultrafast semiconductor materials with short carrier recombination times. Low-temperature grown Gallium Arsenide (LT-GaAs) is the most commonly used material for fabricating PC emitters due to its sub-picosecond lifetime. Dipole antenna is fabricated on a semiconductor substrate and consists of two metallic electrodes that are deposited onto the substrate. The distance between antenna lines is called a gap. A bias voltage is applied between the electrodes. When a femtosecond laser pulse illuminates the biased PC antenna gap, photo carriers are generated and then accelerated by the biasing electric field and decay with a time constant which is determined by the carrier lifetime of the semiconductor. The acceleration and decay of the photoexcited carriers under the applied electric field create a transient photocurrent in the PC antenna. The photocurrent density J can be written as, $N(t)qv(t)$, where $N(t)$ is the density of photo-carriers, q is the elementary charge, and $v(t)$ is the average velocity of the carrier. Since the photocurrent varies in time, it

generates an electromagnetic pulse. The electric field of the radiated THz pulse at a distance r from the source and time t is directly proportional to the time derivative of the transient current and can be described as [4]:

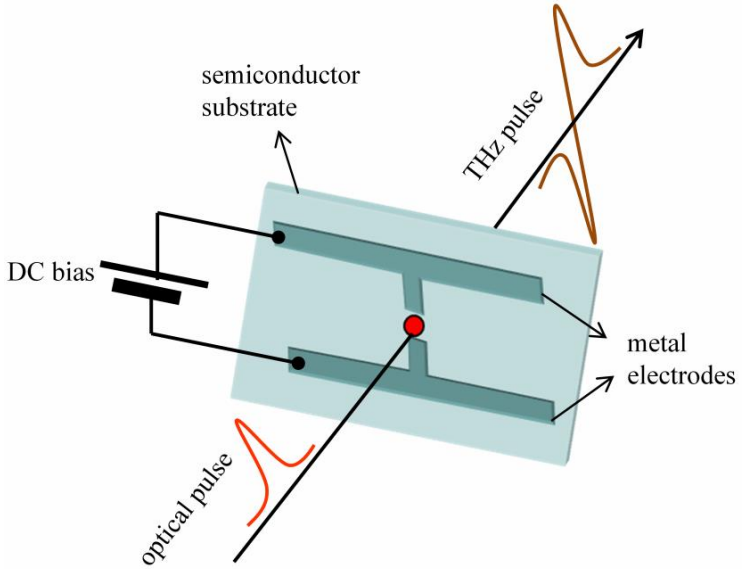

Figure 3.2: Schematic of THz pulse emission from a photoconductive antenna. The red spot indicates the focus of the femtosecond laser.

$$E(r,t) = \frac{l_e}{4\pi\varepsilon_0 c^2 r}\frac{\partial J(t)}{\partial t}\sin\theta \propto \frac{\partial J(t)}{\partial t}, \tag{3.1}$$

where l_e is the effective length of the dipole, ε_0 is the dielectric constant in the vacuum, c is the velocity of light in a vacuum, $J(t)$ is the current of the dipole at a time t, and θ is the angle from the direction of the dipole. From Eq. (3.1), it can be regarded that longer antennas have large signal amplitudes. Furthermore, in order to collimate the THz pulses, a hemispherical Si lens which has a high electrical resistivity is attached to the PC antenna. Generally, Si material is used for the lens since it has a uniform refractive index and a very low absorption coefficient. The emitter is glued to the focus of the hemispherical lens in order to minimize losses due to internal reflection. Therefore, this type of hemispherical lens provides a beam without spherical aberration. In addition, the pulsed photo-current amplitude increases linearly with the applied bias voltage and the pump laser intensity.

There are several structures of PC antennas such as spiral, bow-tie, and strip line [6] besides dipole antenna. The performance of a PC antenna depends on the substrate material, geometry of antenna, and the excitation laser pulse. Therefore, the radiation efficiencies are different among these antennas.

3.3 THz detection with photoconductive antennas

Photoconductive antenna for THz pulse emission can be used for THz pulse detection as well. In the detection of THz radiation with PC antennas, a current meter is connected instead of external bias voltage. Figure 3.3 shows a schematic diagram of THz pulse detection with PC a antenna. In the generation process of the THz pulse, an external bias voltage is applied to the PC antenna in order to accelerate the charged carriers along the transmission lines. However, in the detection process, the acceleration of the charged carriers is provided by the generated THz pulses. Optical pulse generates carriers in the semiconductor substrate of the PC antenna. The carriers are accelerated by the THz field and form an electric current. This transient current is proportional to the applied THz electric field. The gap size for PC antennas designed for detection is typically much narrower (~10 μm) than that for the PC antenna designed for emission (>50 μm), because narrow gaps require less bias voltage to apply a required electric field to generate a measurable current.

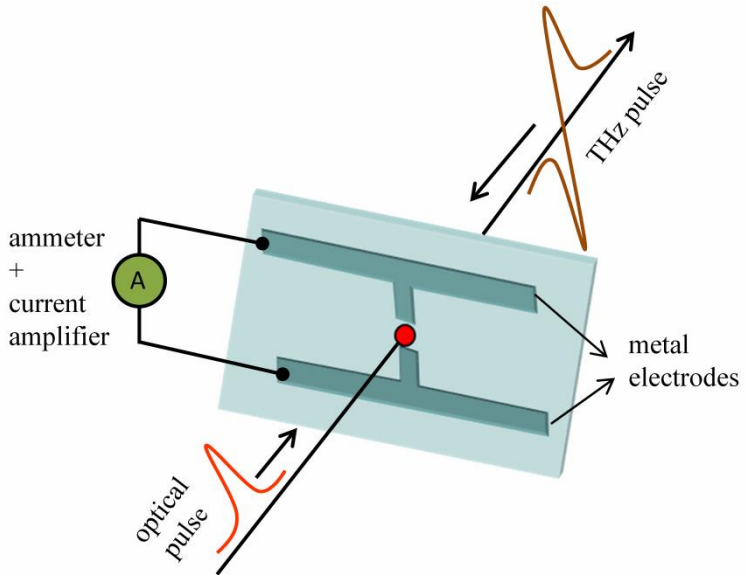

Figure 3.3: Schematic of THz pulse detection with photoconductive antenna. The red spot indicates the focus of the femtosecond laser.

3.4 Terahertz time-domain spectroscopy (THz-TDS)

THz-TDS is a nondestructive and non-contact measurement technique that is used for determining electronic and optical properties of materials in the THz frequency range. In this measurement, THz wave pulses are used to probe the properties of a material, in which the temporal electric field of THz pulses measured. In practice, there are two widely used

experimental setups for terahertz spectroscopy, transmission THz-TDS [7] and reflection THz-TDS [8]. In the transmission setup, the THz beam generated by the emitter is focused on the sample position and propagates through the sample. After that, the beam is again focused on the detector system. The transmission setup is used to measure optically thin samples. For opaque samples, the reflection setup is required. Instead of propagating through the sample, the THz pulse is reflected from the sample. Then the beam is led to the detector by a beam splitter. In this section, we will briefly discuss the THz-TDS experimental setups and revise the data analysis for material parameters extraction.

3.4.1 Transmission THz-TDS

A typical schematic of a transmission THz-TDS setup is shown in Fig. 3.4. The system is based on a mode-lock Ti:sapphire laser that produces femtosecond laser pulses. The femtosecond laser pulses are divided into two pulses. One of the laser pulses is focused on the biased photoconductive emitter to generate THz pulses. The divergent THz pulses are collected and collimated by two parabolic mirrors and focused onto the sample. The transmitted THz pulses through the sample are collected and collimated by other two parabolic mirrors and focused onto the detector. The other optical pulse is focused onto the detector through variable delay stage. The THz pulses are obtained by scanning the relative time delay between the THz pulses and the laser detection pulse. The signal from the detector is usually weak. To detect such small signals, a lock-in amplifier is used. This system requires a mechanical chopper

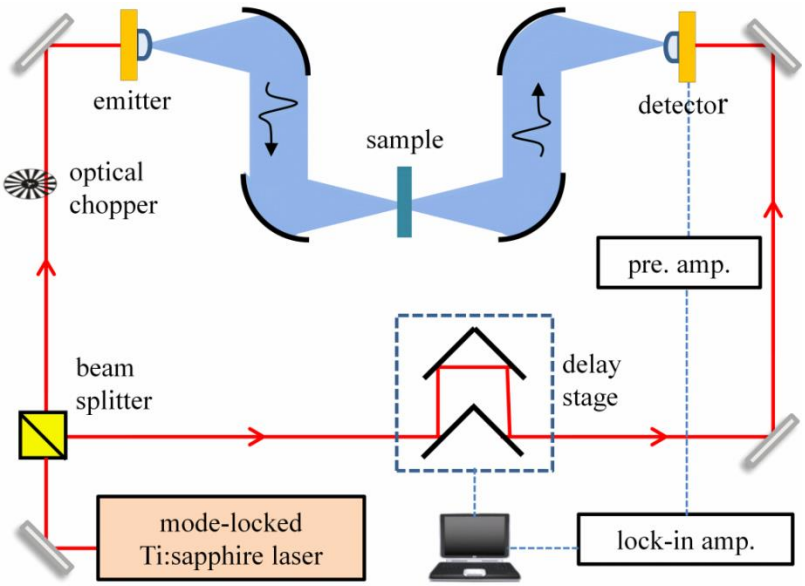

Figure 3.4: Schematic of the experimental setup employed for transmission-type THz-TDS

to be placed in the emitter or detector branch. There is setup without chopper, when an emitter is biased with an AC voltage. The typical operation frequency of the chopper is 1-2 kHz. The delay line is used for temporal scanning of the generated THz pulses. The delay line and lock-inamplifier are controlled by using a computer. The whole terahertz beam path from the transmitter to receiver is enclosed and purged with dry nitrogen, because water vapor absorbs THz radiation strongly at some frequencies.

In the transmission THz-TDS, two measurements are performed in the time-domain: one is with a sample, and the other is without a sample. The two measured signals are transferred to the frequency domain. Figure 3.5 shows the measurement of the transmitted THz pulses and an example of a data measured using this system, in which time-domain waveforms and the related frequency spectra are shown, which allows the determination of the absorption coefficient and the refractive index of the sample in the THz region. Typical THz-TDS spectra can range from 0.1 to 4 THz. The spectroscopic information obtained using THz-TDS also provides data to calculate the conductivity, charge carrier density, and carrier mobility of materials [7].

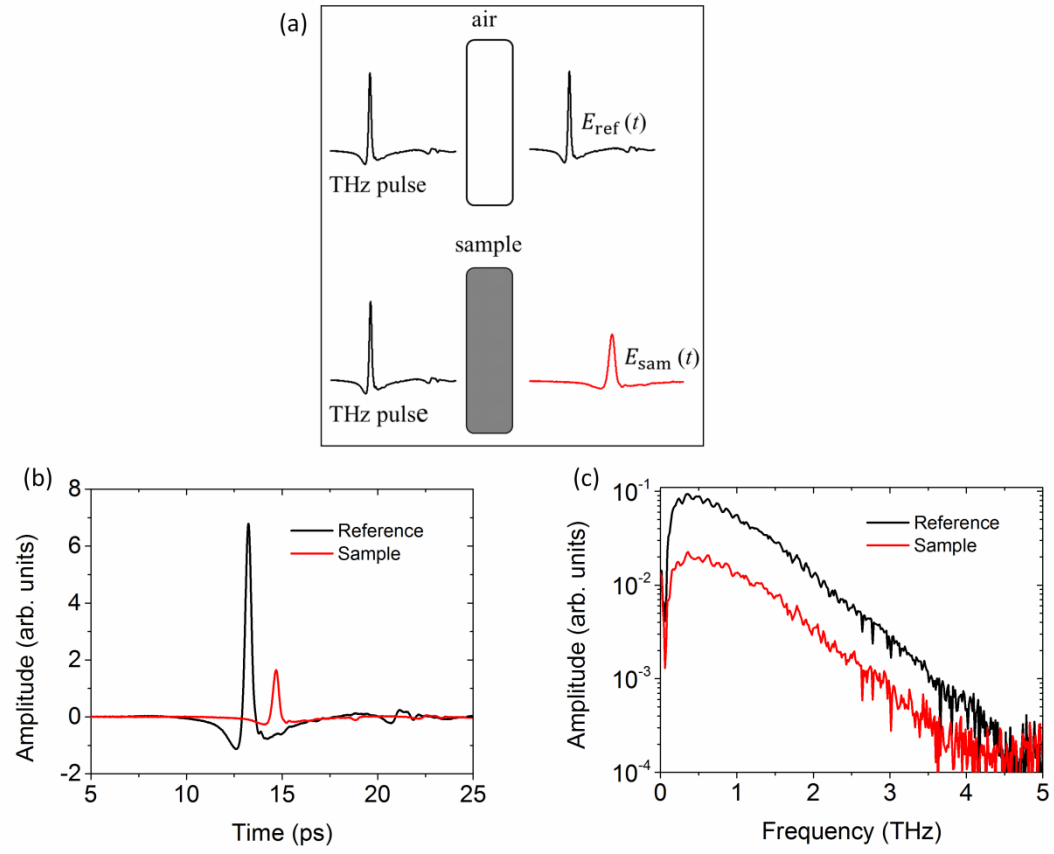

Figure 3.5: (a) THz transmission measurement, (b) time-domain THz signal and (c) related frequency spectrum by transmission THz-TDS.

3.4.1.1 Material parameter estimation

Terahertz spectroscopy allows determining optical properties of material as a function of frequency. The first step in the analysis of the THz data is the extraction of complex refractive index, $\tilde{n}(\omega)$:

$$\tilde{n}(\omega) = n(\omega) + i\kappa(\omega) \tag{3.2}$$

where $n(\omega)$ is the real part of refractive index related to the phase change in a given medium and $\kappa(\omega)$ is the imaginary part related to the amplitude of the absorption coefficient of the material $\alpha(\omega)$ determined as $\alpha(\omega) = 2\omega\kappa(\omega)/c$.

In order to determine the complex refractive index, the time-domain waveforms are converted to the frequency-domain by fast Fourier transformation (FFT) to obtain the amplitude and phase spectra. If the time-domain reference and sample signals are $E_{\mathrm{ref}}(t)$ and $E_{\mathrm{sam}}(t)$ and their complex amplitudes as $\tilde{E}_{\mathrm{ref}}(\omega)$ and $\tilde{E}_{\mathrm{sam}}(\omega)$, respectively in the frequency domain, the ratio of the sample spectrum to reference spectrum, $\frac{\tilde{E}_{\mathrm{sam}}(\omega)}{\tilde{E}_{\mathrm{ref}}(\omega)}$, is given by [4]:

$$\frac{\tilde{E}_{\mathrm{sam}}(\omega)}{\tilde{E}_{\mathrm{ref}}(\omega)} = \sqrt{T(\omega)}\,\exp[i\Delta\varphi(\omega)] \tag{3.3}$$

$$\therefore\ \frac{\tilde{E}_{\mathrm{sam}}(\omega)}{\tilde{E}_{\mathrm{ref}}(\omega)} = t_{\mathrm{as}}.t_{\mathrm{sa}}.\exp\left[\frac{i(\tilde{n}(\omega)-1)d\omega}{c}\right], \tag{3.4}$$

where $\Delta\varphi(\omega) = \varphi_{\mathrm{sam}}(\omega) - \varphi_{\mathrm{ref}}(\omega)$ is the phase difference between sample and reference phase spectra, c is the velocity of light and d is the sample thickness, t_{as} and t_{sa} are the Fresnel's transmission coefficients for electric field from air to sample and sample to air, respectively and can be written as:

$$t_{\mathrm{as}} = \frac{2}{\tilde{n}(\omega)+1}, \qquad t_{\mathrm{sa}} = \frac{2\tilde{n}(\omega)}{\tilde{n}(\omega)+1} \tag{3.5}$$

By separating the real and imaginary parts of Eq. (3.4), we can solve numerically the real and imaginary parts of refractive index as a function of frequency. The complex refractive index of real and imaginary part is then expressed as:

$$n(\omega) = \frac{c}{d\omega}\left[\Delta\varphi(\omega) + \frac{d\omega}{c} - \arg(t_{\mathrm{as}}.t_{\mathrm{sa}})\right], \tag{3.6}$$

$$\kappa(\omega) = -\frac{c}{2d\omega}.\ln\left[\frac{T(\omega)}{|t_{as}.t_{sa}|^2}\right]. \quad (3.7)$$

Once we have the real and imaginary parts of the refractive index, the relative complex dielectric constant is obtained by:

$$\tilde{\varepsilon}(\omega) = |\tilde{n}(\omega)|^2 = \varepsilon_1(\omega) + i\varepsilon_2(\omega) \quad (3.8)$$

The complex dielectric constant and the complex conductivity, $\tilde{\sigma}(\omega)$, have the following relation:

$$\tilde{\varepsilon}(\omega) = \varepsilon_\infty - i\frac{\tilde{\sigma}(\omega)}{\omega\varepsilon_0} \quad (3.9)$$

$$\tilde{\sigma}(\omega) = \sigma_1(\omega) + i\sigma_2(\omega)$$

$$\sigma_1(\omega) = -\varepsilon_0\omega\varepsilon_2(\omega)\,, \quad (3.10)$$

$$\text{and } \sigma_2(\omega) = \varepsilon_0\omega[\varepsilon_1(\omega) - \varepsilon_\infty]\,, \quad (3.11)$$

where ε_0 is the permittivity in vacuum and ε_∞ is the relative permittivity in the limit of very high frequency.

3.4.1.2 Drude model

Drude model is the most common and straightforward model for conductivity in metals and semiconductors [9]. This model treats the conduction electrons as independent particles that are free to move between scattering events. The collisions happen at the rate $\Gamma = 1/\tau$, where τ is the average time interval between the scattering events.

DC conductivity:

When no electric field is present, electrons are move randomly, thus the net velocity of one electron is zero. There is no current flow in this case. In the presence of an electric field $\vec{E}$, electrons experience a force, $-e\vec{E}$, and gain a velocity:

$$\vec{v}(t) = \frac{-e\vec{E}}{m}t\,, \quad (3.12)$$

where t is the time after the last collision. For $t = \tau$, the average time an electron travels

between collisions, the average velocity is given by

$$\vec{v}_{ave} = \frac{-e\vec{E}}{m^*}\tau\,, \tag{3.13}$$

where m^* is the effective mass since we have to consider electrons in a solid material.

For *N* free electrons per unit volume, the current density $\vec{j}$ is given as:

$$\vec{j} = -Ne\vec{v}_{ave} \tag{3.14}$$

Substituting Eq. (3.13) to (3.14) gives a general expression for the DC conductivity σ_{DC} in the Drude model.

$$\vec{j} = \left(\frac{Ne^2\tau}{m^*}\right)\vec{E} = \sigma_{\mathrm{DC}}\vec{E} \tag{3.15}$$

$$\sigma_{\mathrm{DC}} = \frac{Ne^2\tau}{m^*} \tag{3.16}$$

AC conductivity:

The electron equation of motion with a time dependent electric field $\vec{E}$ can be described as [10]:

$$\frac{d\vec{p}(t)}{dt} = -\frac{\vec{p}(t)}{\tau} - e\vec{E}(t) \tag{3.17}$$

The equation of motion under an applied electric field $\vec{E}(t) = \vec{E}(\omega)\exp(-i\omega t)$ and a momentum of the form $\vec{p}(t) = \vec{p}(\omega)\exp(-i\omega t)$, leads to:

$$-i\omega\vec{p}(\omega) = -\frac{\vec{p}(\omega)}{\tau} - e\vec{E}(\omega)$$

$$\Rightarrow\ \vec{p}(\omega) = -\frac{e\vec{E}(\omega)}{1/\tau - i\omega}$$

Again use $\vec{j}(\omega) = -Ne\vec{p}(\omega)/m^*$, we get:

$$\vec{j}(\omega) = \frac{(Ne^2/m^*)\vec{E}(\omega)}{1/\tau - i\omega} = \frac{Ne^2\tau}{m^*}\frac{1}{1-i\omega\tau}\vec{E}(\omega) \tag{3.18}$$

Then the frequency dependent conductivity in Drude model:

$$\tilde{\sigma}(\omega) = \frac{Ne^2\tau}{m^*}\frac{1}{1-i\omega\tau} = \frac{\sigma_{\mathrm{DC}}}{1-i\omega\tau} \tag{3.19}$$

An important parameter to present the electron density oscillation in the conducting media is called plasma frequency [1] and given by:

$$\omega_{\mathrm{p}} = \left(\frac{Ne^2}{\varepsilon_0 m^*}\right)^{1/2} \tag{3.20}$$

The frequency dependent conductivity can be rewritten as:

$$\tilde{\sigma}(\omega) = \frac{i\varepsilon_0 \omega_{\mathrm{p}}^2}{(\omega + i\Gamma)} \tag{3.21}$$

where ω_p is plasma frequency and Γ is the scattering or damping rate. These two parameters are optimized to fit the measured THz data and can be used to calculate carrier concentration and mobility.

$$N = \frac{\omega_{\mathrm{p}}^2 \varepsilon_0 m^*}{e^2} \tag{3.22}$$

$$\mu = \frac{e}{m^* \Gamma} = \frac{e\tau}{m^*} \tag{3.23}$$

3.4.2 Reflection THz-TDS

Terahertz spectra are detectable using both transmission and reflection types of THz-TDS systems. Transmission measurements are often used to obtain absorption spectra. However, some samples, particularly liquids and metallic materials as well as the optically thick samples cannot be measured by transmission THz-TDS system. Therefore, the reflection THz-TDS is required for such samples. Many materials reported in literature such as semiconductor [11], liquid [12] have been measured by reflected THz pulses. In the reflection THz-TDS system, a metal mirror with high reflectivity is used as the reference measurement. During the measurement, the front surface of the reference mirror should be placed exactly where the front surface of the sample in order to minimize the displacement error between the sample and reference. However, it is quite difficult to totally avoid the misplacement error in practice. To overcome this limitation, a special sample holder is used, which allows the reflection measurements with almost no phase error. In the system described below, I adopted the geometry of normal incidence [13]. This geometry is favorable for both spectroscopy and imaging.

3.4.2.1 Reflection THz-TDS setup

The schematic configuration of the experimental setup for the reflection THz-TDS system is shown in Fig. 3.6. A mode-lock Ti:sapphire laser, which provided 70 fs pulses and a wavelength of 800 nm at a repetition rate of 82 MHz, was used as an optical source. The femtosecond laser beam is divided into two beams by using a cubic beam splitter. One of the beams illuminates the (100) InAs wafer at an incident angle of 45° for generating THz pulses. Two parabolic mirrors are used to collimate and focus the generated THz pulses onto the sample (or the reference mirror) surface at normal incidence and the reflected THz pulses from the surface is focused onto the detector by wire-grid polarizer (wire-grid 1) and a third parabolic mirror. The polarized reflectivity can be measured using two wire-grid polarizers. The other laser beam passes through a variable delay-stage and is focused onto the detector. The detector consists of a photoconductive dipole antenna on a LT-GaAs substrate. The THz pulse wave is obtained by varying the optical length of the femtosecond laser. In order to avoid the misplacement error, the reference mirror and the sample are placed on the sample holder and their positions are changed using a computer-controlled *x-y* translation stage. For imaging, the time-delay stage is generally fixed at the maximum amplitude of the THz signal, and then the THz beam is scanned over the sample surface using the computer controlled *x-y* stage.

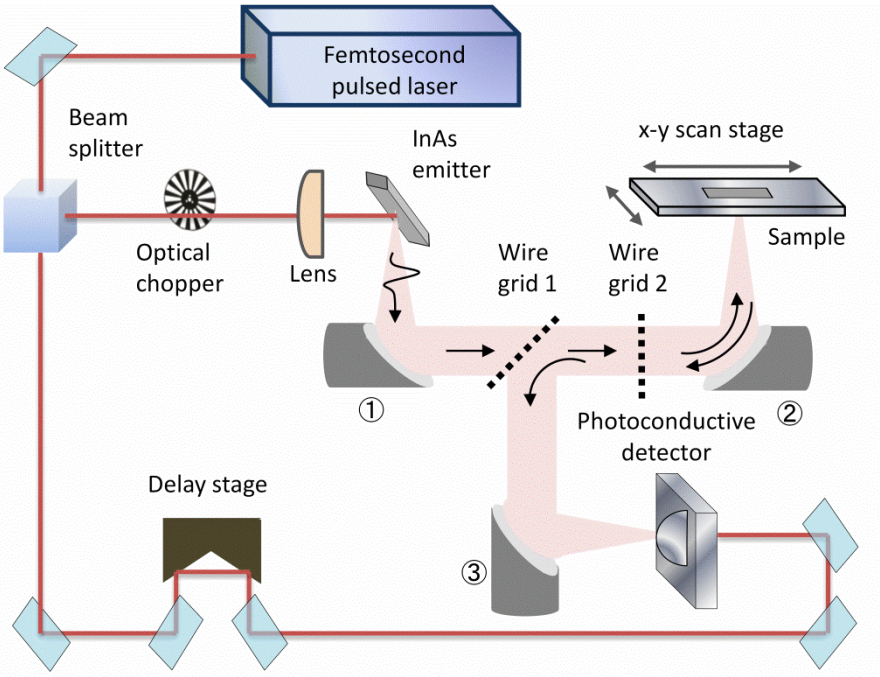

Figure 3.6: schematic of the experimental setup employed for reflection THz-TDS

Figure 3.7 shows the measurement of the reflected THz pulses and an example of the temporal waveforms of the detected THz pulses from a gold mirror and a sample. From these measurement results, the reflectance and the optical constant of the sample can be determined.

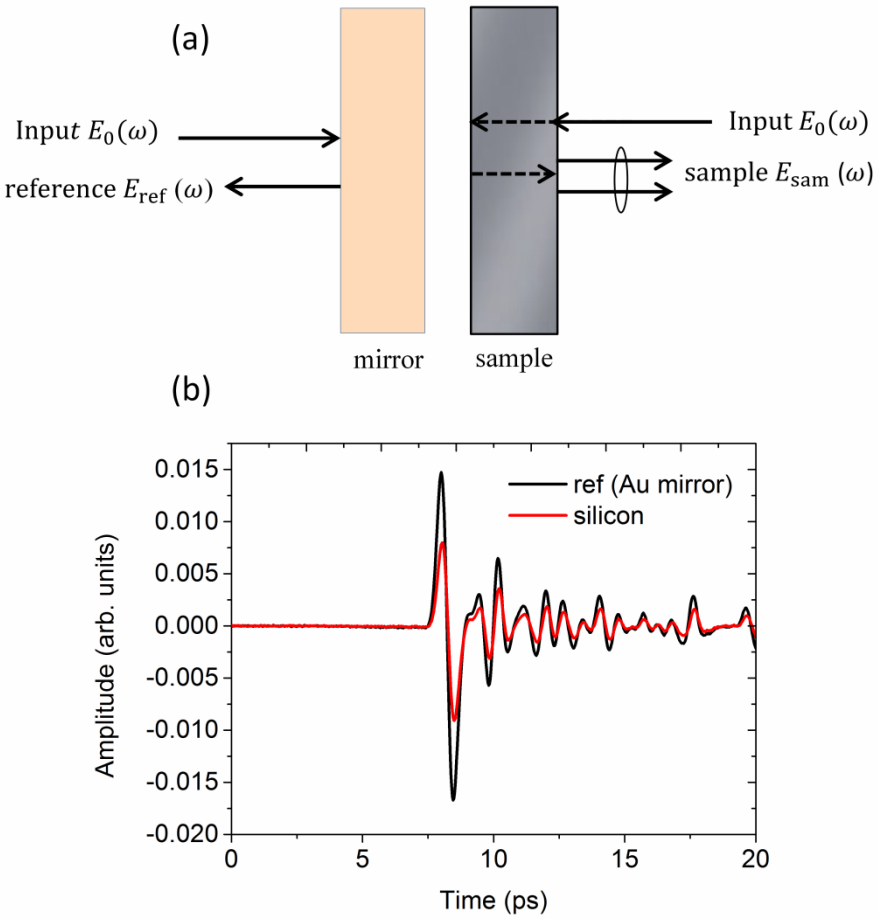

Figure 3.7: (a) Reflection of normally incident THz wave and (b) the THz temporal waveforms obtained from a reference mirror and a sample.

3.4.2.2 Data analysis

In the measurements, two waveforms with and without sample, $E_{\mathrm{sam}}(t)$ and $E_{\mathrm{ref.}}(t)$, are measured in the time-domain and are Fourier-transformed into complex electric fields $\tilde{E}_{\mathrm{sam}}(\nu)$ and $\tilde{E}_{\mathrm{ref}}(\nu)$ in the frequency domain. For reference measurement, the THz signal is recorded from a gold mirror. Since the refractive index of air is $n = 1$ and the gold mirror is almost perfect reflector in the THz frequencies, the complex reflection coefficient $\tilde{r}$ at normal incidence is given by [13]

$$\tilde{r} = \frac{|E_{\text{sam}}(\nu)|}{|E_{\text{ref}}(\nu)|}\exp(i[\phi_{\text{sam}}(\nu) - \phi_{\text{ref}}(\nu)]) \equiv r(\nu)\exp[i\phi(\nu)]$$

$$= \frac{n(\nu) + i\kappa(\nu) - 1}{n(\nu) + i\kappa(\nu) + 1} \tag{3.24}$$

where ν is terahertz frequency, ϕ is phase difference, r is the amplitude ratio of the sample spectrum to the reference spectrum, and $\tilde{n} = n + i\kappa$ is the complex refractive index of the sample, n is the refractive index and κ is the extinction coefficient. By solving equation (3.24), the refractive index of the sample can be obtained as:

$$n(\nu) = \frac{1 - r(\nu)^2}{1 + r(\nu)^2 - 2r(\nu)\cos\phi(\nu)}, \tag{3.25}$$

$$\kappa(\nu) = \frac{2r(\nu)sin\phi(\nu)}{1 + r(\nu)^2 - 2r(\nu)\cos\phi(\nu)} \tag{3.26}$$

The absorption can be calculated as:

$$\alpha = \frac{4\pi\nu\kappa}{c} \tag{3.27}$$

3.5 Laser terahertz emission microscope (LTEM)

THz spectroscopic imaging techniques have received great attention in various fields ranging from medical to industry. The most attractive imaging tool for THz applications is laser terahertz emission microscope (LTEM). In this system, the sample itself is the source of THz emission. This is a nondestructive tool that can detect and image THz pulse emission from various electronic materials such as semiconductors, high-critical-temperature superconductors, or ferroelectric materials by femtosecond laser pulse excitation [14-16]. LTEM can analyze the dynamic behavior of photoexcited carriers and local distribution of electric field in the materials or devices by reflecting THz emission properties such as amplitude and waveform. One of the main futures of this system is spatial resolution, which can be determined by the pump laser spot size. Therefore, it is necessary to minimize the focused beam size to improve the spatial resolution. Thus, it is possible to obtain a sub-micrometer order resolution. T. Kiwa et al., [17] inspected a defective interconnection in IC chip using this system. The LTEM image of the broken IC chips show different pattern from the normal chips. This system was also applied to

study THz wave emission from a solar cell and visualize THz wave emission image of the cell [18]. With this system, we can study the dynamics of the photoexcited carriers at the surface as well as inside the solar cell illuminated by additional CW light.

3.5.1 Principle of LTEM

The principle of LTEM can be explained by considering the semiconductor material. When femtosecond laser pulse irradiates a semiconductor sample with a higher energy than the energy gap of the material, the photoexcited carriers are accelerated by an externally applied bias field or by the internal static field such as Schottky field, *p–n* junction field, and then decay with a time constant determined by the carrier's lifetime. This induces a transient photo-current that generates THz wave radiation according to the classical formula of electrodynamics,

$$E_{\mathrm{THz}}(t) \propto \frac{\partial J(t)}{\partial t}, \tag{3.28}$$

where $E_{\mathrm{THz}}(t)$ is the radiated electric field and $J(t)$ is the transient current. The amplitude of the terahertz pulse is proportional to the local electric field. Thus, this enables visualization of the local field distribution in photoexcited samples by mapping the amplitude of THz pulse [19].

3.5.2 LTEM setup

The basic LTEM imaging setup is shown schematically in Fig. 3.8. As a laser source, the Ti:sapphire femtosecond laser (800 nm wavelength, 100 fs pulse width and 82 MHz repetition rate) is used. The femtosecond laser pulse is divided into pump pulse and trigger pulse by using a beam splitter. To generate THz pulse, the pump pulse is focused a 45° angle of incidence through an optical lens onto a sample surface mounted on computer-controlled *x-y* stage. The emitted THz waves are collimated and focused onto a detector by a pair of parabolic mirrors. A low-temperature-grown gallium arsenide PC antenna is used as a detector. The detector consists of a spiral type PC antenna on a LT-GaAs substrate. THz signal is acquired by varying the delay between the pump and trigger pulses. The amplitude of the THz wave emission is monitored using a lock-in amplifier. By fixing the time delay at the maximum amplitude of the THz emission and scanning the sample by the pump beam, the THz emission image is obtained.

Figure 3.9 shows an experimental result of THz wave emission image of a poly crystalline silicon solar cell. The image was obtained at the pump laser power of 70 mW and a reverse bias voltage of 10V. The image clearly shows different THz emission between crystalline (yellow) and other area (green).

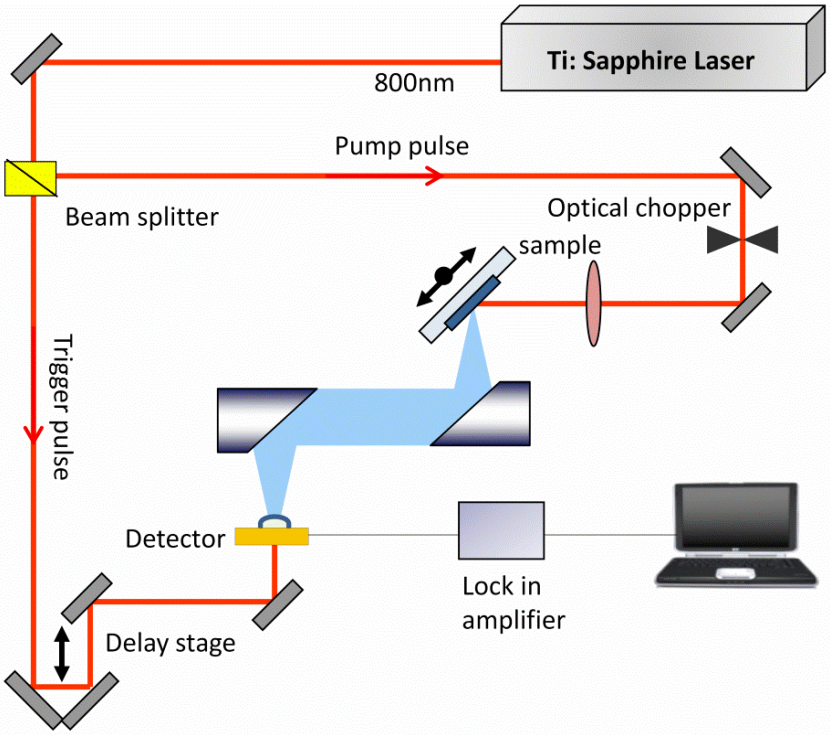

Figure 3.8: Schematic of simple laser terahertz emission microscope (LTEM) system employed in the present study

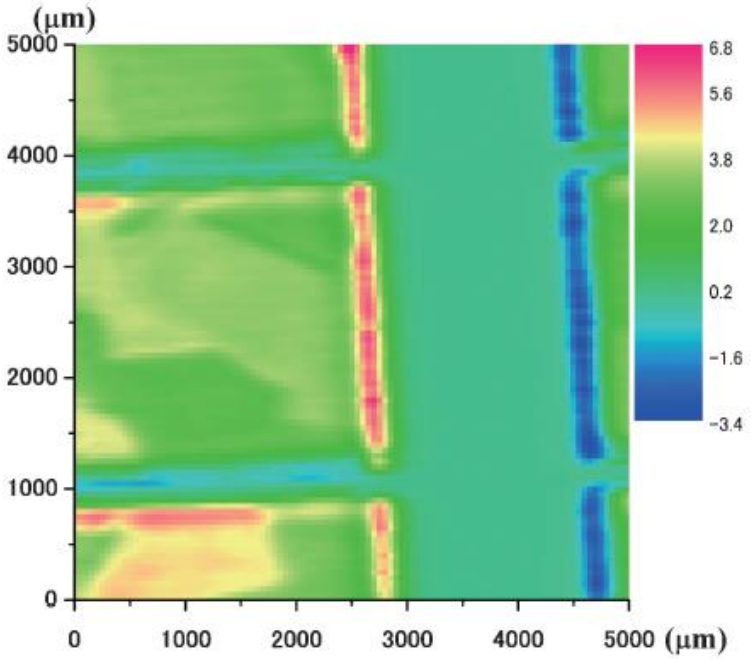

Figure 3.9: Typical LTEM image of poly crystalline silicon solar cell [18]. The image was obtained at an excitation laser power of 70 mW and a reverse bias voltage of 10V.

3.6 Summary

In this chapter, the most commonly used techniques and the principles of generation and detection of THz pulses have been discussed. The mechanisms of photocarriers generation and the consequent THz pulse generation, as well as a brief description of the method of detection are reviewed. A common setup for transmission THz-TDS is presented. The data analysis for transmission geometry is thoroughly revised. The fundamental analytical expressions for material parameters extraction have been highlighted. The reflection THz-TDS is presented and briefly discussed the measurement and data analysis procedure. Laser terahertz emission microscope (LTEM) technique is also reviewed. The experimental setup and the principle of LTEM have been discussed.

References

1. Y-S Lee, *Principles of Terahertz Science and Technology*, New York: Springer (2009).
2. M. Tonouchi. "Cutting-edge terahertz technology," *Nat. Photonics*, **1**, 97 (2007).
3. B. Ferguson & X-C Zhang, "Materials for terahertz science and technology," *Nat. Mater,* **1**, 26 (2002).
4. K. Sakai (Ed.), *Terahertz Optoelectronics*, Berlin: Springer (2005).
5. M. Tani, M. Herrmann and K. Sakai, "Generation and detection of terahertz pulsed radiation with photoconductive antennas and its application to imaging," *Meas. Sci. Technol.*, **13**, 1739 (2002).
6. F. J. Gonzalez and G. D. Boreman, "Comparison of dipole, bowtie spiral and log-periodic IR antennas," *Infrared Phy. Technol.*, **46**, 418 (2005).
7. M. van Exter and D. Grischkowsky, "Carrier dynamics of electrons and holes in moderately doped silicon," *Phys. Rev. B*, **41**, 12140 (1990).
8. T. Jeon and D. Grischkowsky, "Characterization of optically dense, doped semiconductors by reflection THz time domain spectroscopy," *Appl. Phys. Lett.*, **72**, 3032 (1998).
9. M. van Exter and D. Grischkowsky, "Optical and electronic properties of doped silicon from 0.1 to 2 THz", *Appl. Phys. Lett.*, **56**, 1694 (1990).
10. C. Kittel, *Introduction to Solid State Physics*, John Wiley and Sons (2002).
11. M. Khazan, R. Meissner and I. Wilke, "Convertible transmission-reflection time-domain spectrometer," *Rev. Sci. Instrum.*, **72**, 3427 (2001).
12. A. Nakanishi, Y. Kawada, T. Yasuda, K. Akiyama and H. Takahashi, "Terahertz time domain attenuated total reflection spectroscopy with an integrated prism system," *Rev. Sci. Instrum.*, **83**, 033103 (2012).
13. S. Nashima, O. Morikawa, K. Takata and M. Hangyo, "Measurement of optical properties of highly doped silicon by terahertz time domain reflection spectroscopy," *Appl. Phys. Lett.*, **79**, 3923 (2001).
14. H. Murakami and M. Tonouchi, "Laser terahertz emission microscopy," *C. R Physique*, **9**, 169 (2008).
15. M. Tonouchi, M. Yamashita and M. Hangyo, "Terahertz radiation imaging of supercurrent distribution in vertex-penetrated $YBa_2Cu_3O_{7-\delta}$ thin films strips," *J. Appl. Phys.*, **87**, 7366 (2000).
16. M. Yamashita, K. Kawase, C. Otani, T. Kiwa, M. Tonouchi, "Imaging of large-scale integrated circuits using laser-terahertz emission microscopy," *Opt. Express*, **13**, 115 (2005).

17. T. Kiwa, M. Tonouchi, M. Yamashita and K. Kawase, “Laser terahertz-emission microscope for inspecting electrical faults in integrated circuits,” *Opt. Lett.*, **28**, 2058 (2003).
18. H. Nakanishi, S. Fujiwara, K. Takayama, I. Kawayama, H. Murakami, M. Tonouchi, “Imaging of a polycrystalline silicon solar cell using a laser terahertz emission microscope,” *Appl. Phys. Express*, **5**, 112301 (2012).
19. H. Murakami, K. Serita, Y. Maekawa, S. Fujiwara, E. Matsuda, S. Kim, I. Kawayama and M. Tonouchi, “Scamming laser THz imaging system,” *J. Phys. D: Appl. Phys.*, **47**, 374007 (2014).

Chapter 4: Transmission THz-TDS study on solar cell under light illumination

4.1 Introduction

The performance of a photovoltaic cell is usually determined by its energy conversion efficiency [1]. The efficiency depends on the material quality and on the incident intensity and wavelength of the incident light. The majority of today's commercial solar cells are made up of crystalline silicon. Characterization of materials is of importance for design and fabrication of photovoltaic cell. Usually, the finished solar cells are tested and characterized to improve and maintain product quality. However, it is also important to understand the physical behavior of solar cells under light illumination. Efficient photovoltaic cells are required to have efficient photoexcited carrier collection from the cell absorber. Measurements of the wavelength dependence of optical properties are valuable for evaluating the material and device characteristics of photovoltaic cells. For example, the near infrared (NIR) light response is dominated by the charge carrier in the base (*p*-region) of the solar cell. This is because the penetration depth in silicon for NIR light is about 10 μm [2], which is much larger than the thickness (~ 0.5 μm) of the solar cell emitter (*n*-region). On the other hand, the penetration depth in silicon for ultraviolet (UV) light is about is 0.01 μm [2], which is much smaller than the solar cell emitter thickness. Thus, the UV light response is governed by the charge collection from the emitter and also depends on the surface recombination velocity. Therefore, the wavelength dependence response is an important characterization of photovoltaic cells. The spectral effects on multi-junction photovoltaic cells have been investigated using photoluminescence, where each layer utilizes light with different wavelengths [3]. The goal is to measure the wavelength dependence of optical properties to understand the performance of the photovoltaic cells. Therefore, photovoltaic industry needs noncontact and nondestructive techniques for precise measurement of optical properties in solar cells. THz spectroscopy is an effective technique to characterize Si based materials and devices. Over the past few decades, this technique has been used to characterize a wide variety of materials including semiconductors [4-6]. Frequency dependent response can be obtained from the detected signal and gives information on the absorption coefficient and refractive index of the material in the THz range. From this, the complex dielectric constant and complex conductivity can be deduced. Moreover, carrier density, carrier mobility, and the plasma frequency can be estimated from the spectroscopic data [7]. By making use of the THz

technique, we can measure the optical properties of solar materials or semi-finished solar cells without electric contacts at the beginning as well as during the production process of the solar cells in the THz frequency range. This technique was effectively applied to study the properties of the irradiated silicon wafer for the application of space solar cells [8]. Here in this chapter, using transmission THz-TDS, I studied the optical properties such as complex refractive index, conductivity, charge carrier density and mobility of single crystalline Si solar cells under continuous-wave (CW) 800 nm (NIR) and 365 nm (UV) light illumination.

4.2 Samples

The solar cells used in this study are made of single crystalline silicon. It was made from *p*-type base and *n*-type emitter to create *p*–*n* junction. In this study, two single crystalline Si solar cells were used: one was without antireflection (AR) coating and the other had a silicon nitride (SiN_x) AR coating on the surface with thickness of 70 nm. The front surface of each sample was textured and the rear surface was of unpolished rough surface. Both samples had no electrodes. Typical doping densities were 1×10^{19} cm^{-3} in the *n*-type region and 1×10^{16} cm^{-3} in the *p*-type region and the thickness of the emitter (*n*-region) was the ~0.5 μm [9]. Schematic structures of the single crystalline solar cells are shown in Fig. 4.1.

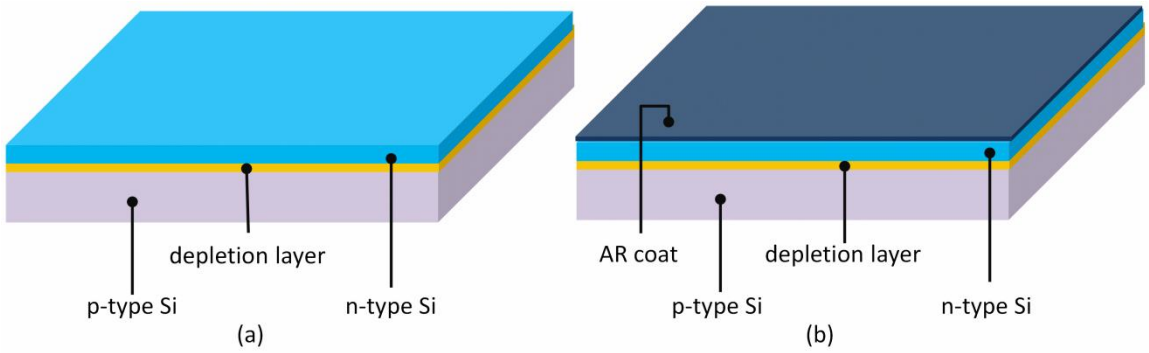

Figure 4.1: Schematic structure of single crystalline Si solar cells (a) without and (b) with AR coating; both samples have no electrodes.

4.3 Experimental procedure

The experimental setup and how the THz-TDS system works were explained in Chapter 3. The system (Otsuka Electronics TR-1000) used in this work is schematically shown in Fig. 4.2. A femtosecond pulsed laser operating at a wavelength of 780 nm and repetition frequency of 50 MHz was used as an optical source. The laser pulses were divided by a beam splitter into pump and probe pulses. The pump pulses were incident on a low-temperature-grown GaAs (LT-GaAs)

photoconductive antenna to generate terahertz pulses. Four off-axis parabolic mirrors were guided the generated THz wave to the detector. A similar photoconductive antenna was used for detection. LT-GaAs photoconductive antenna emits THz wave with the frequency range of 0.04 - 4 THz in this system. In addition, a CW light was introduced into the system, and sample was illuminated by the CW light with wavelength of 800 nm (NIR) or 365 nm (UV) at various powers to generate charge carriers. Illumination with NIR light favors charge generation in the base while illumination with UV light favors charge generation at the surface region of the solar cell. The illumination area on the sample was 0.5 cm^2 and 0.88 cm^2 for NIR and UV light, respectively. The THz radiation was focused onto the sample with a spot diameter of about 5 mm. The illumination area was larger than that of THz beam spot, so that the THz wave was incident in a uniformity of illumination of photoexcitation. Measurements were carried out at various illumination powers of illumination light on both surfaces of the non-coated and the AR-coated samples. Table 4.1 indicates the measurement conditions at two wavelengths of light illuminating on the two sample surfaces. Two types of measurements were taken in the time-domain, with and without the sample (which serves as the reference). The optical properties of the sample can be deduced by analyzing the fast Fourier transformation (FFT) spectrum of the time-domain signals. All measurements were performed at room temperature with relative humidity of 30-35%.

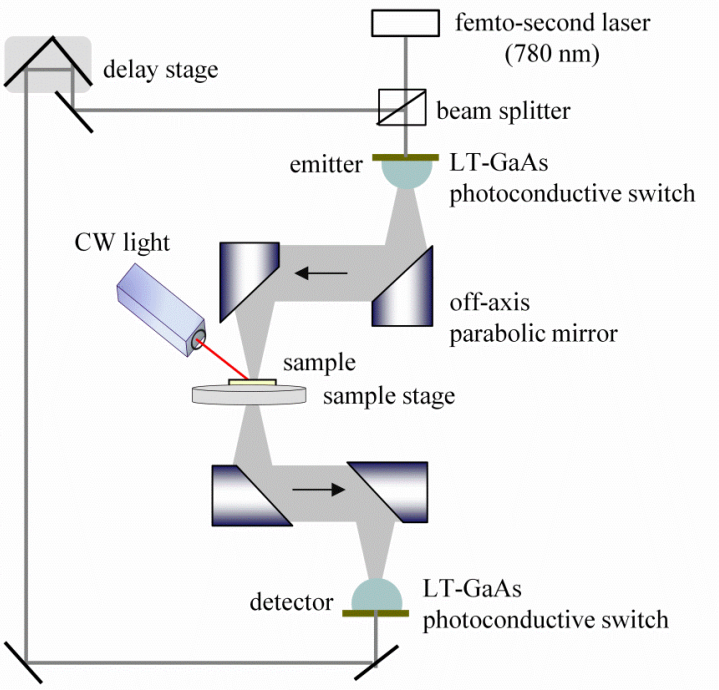

Figure 4.2: Schematic experimental setup for transmission-type THz-TDS system employed in the present study.

Table 4.1: Measurement conditions for experiment

Sample	Surface incident	Illumination light
Single crystalline Si solar cell	without AR coating	◆ no illumination ◆ 800 nm (NIR) illumination ◆ 365 nm (UV) illumination
	with AR coating	◆ 800 nm (NIR) illumination
	rear surface	◆ 800 nm (NIR) illumination

4.4 Results and discussion

4.4.1 Measurements of surface roughness

Commercially available silicon solar cells are fabricated on low-cost substrates that contain relatively high concentration of impurities and defects. The surface of the substrate has very high reflection and surface recombination velocity, which are serious problems for solar cells. Several methods such as chemical etching, deposition of antireflection coatings, and texturing of a surface can fix these problems [10, 11]. Generally, the solar cells are textured by etching the front surface with alkaline solution to obtain pyramids [12]. Light reflected at a textured surface hits another surface and reenters, reducing the total reflection of light and increasing the absorption inside the solar cells. However, texturing cannot reduce the reflection sufficiently; therefore, an antireflection coating is used on the textured surface to reduce further reflection. To measure the surface roughness of the single crystalline Si solar cells studied in this chapter, an atomic force microscope (AFM) was used.

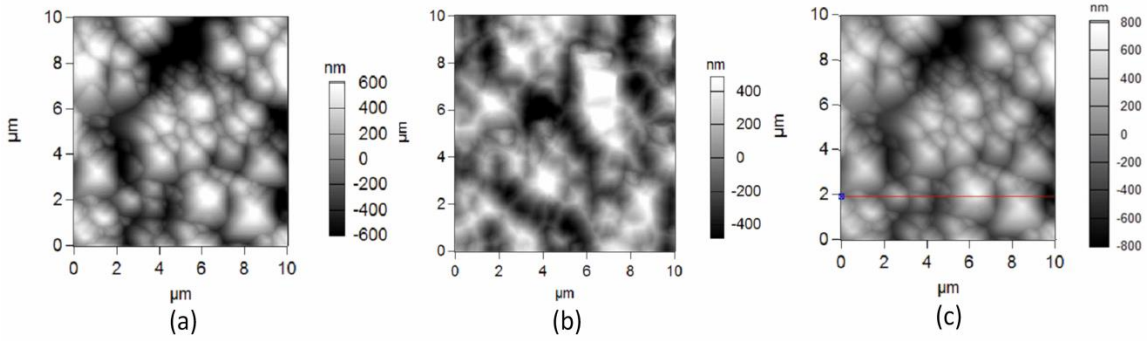

Figure 4.3: AFM images of single crystalline Si solar cell (a) front surface without AR coating (b) rear rough surface and (c) front surface with AR coating.

Table 4.2: Surface roughness of single crystalline Si solar cells measured by AFM

Surface	Without AR coating	With AR coating	Rear surface
RMS (nm)	150	310	240

Figure 4.3 shows the AFM surface images of the single crystalline Si solar cells. The measured area was randomly selected for each surface. Surface roughness is usually defined as root-mean-square (RMS) roughness in the direction perpendicular to the surface. Table 4.2 shows the surface roughness (RMS) values measured to the samples. The image of front surface without AR coating (Fig. 4.3(a)) showed that the textured surface with different sizes of pyramidal structures was randomly distributed over the entire surface with a RMS value of 150 nm. The rear surface image (Fig. 4.3(b)) showed an unpolished rough surface with RMS value of 240 nm, which was higher than that in the front surface. The AFM image of a AR coating surface (Fig. 4.3(c)) also showed pyramidal structure with RMS value of 310 nm. This value was much high compared to that of the non-coating sample, meaning that the front AR coating surface was relatively rough.

4.4.2 Measurements of sample thickness

Terahertz spectroscopy is usually used to measure the optical properties of a sample. The accuracy of a THz measurement mainly depends on precise sample thickness determination. Therefore, it is crucial to determine the thickness of the sample with high precision. THz-TDS in transmission as well as reflection mode can be used to measure the thickness of sample. However, these methods have a common limitation, that is, the refractive index of the material needs to be known for the determination of thickness accurately. In the THz-TDS transmission measurement, the sample thickness *d* can be calculated by the known refractive index and the time delay of a THz pulse propagating through the sample using the following equation [13]:

$$d = \frac{c\Delta t_t}{n_{\mathrm{sam}} - n_{\mathrm{ref}}}, \tag{4.1}$$

where $\Delta t_{\mathrm{t}} = t_{\mathrm{sam}} - t_{\mathrm{ref}}$, and t_{sam} & t_{ref} are the times of THz peaks for the sample and reference (no sample), respectively, as shown in Fig. 4.4, and *c* is the speed of light in a vacuum. If air is used as the reference, $n_{\mathrm{ref}} = 1$, and the refractive index of sample is determined at THz frequencies, $n_{\mathrm{sam}} = n_{\mathrm{THz}}$, equation (4.1) can be rewritten as:

$$d \approx \frac{c\Delta t_{\mathrm{t}}}{\mathrm{n_{THz}} - 1} \tag{4.2}$$

Figure 4.4 shows the waveforms obtained by THz-TDS in transmission mode. The red curve is the delayed waveform of the THz pulse transmitted through the single crystalline Si solar cell while the black curve shows the free space propagation of the THz waves. The time delay between the reference and sample pulses is $\Delta t_{\mathrm{t}} = 1.45$ ps.

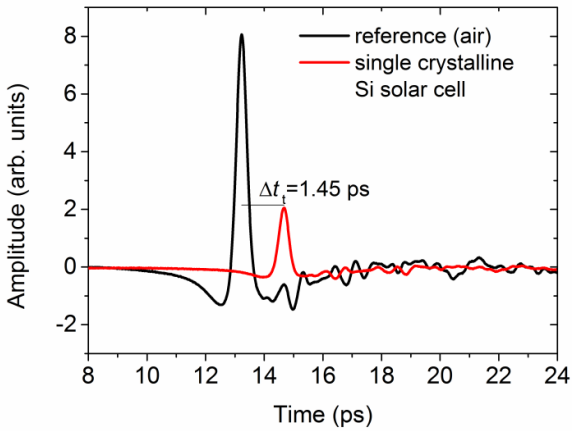

Figure 4.4: Time variations of THz pulses transmitted through air (no sample) and single crystalline Si solar cell.

In the THz-TDS in the reflection mode (system described in detail in section 3.4.2), first the sample is placed normal to the THz beam and the reflections are measured. The measurement principle is as follows: a part of the THz beam is reflected from the front surface while the rest penetrates into the sample and reflects back from the rear surface. Figure 4.5 shows the waveform of the THz pulses reflected from the single crystalline Si solar cell. The thickness of the sample is determined by using Δt_{r} , defined as the temporal difference between the front and rear surface reflections by Eq. (4.3) [14]. The front and rear surface reflections are clearly visible and the temporal difference of the reflections, $\Delta t_{\mathrm{r}} = 4.16$ ps.

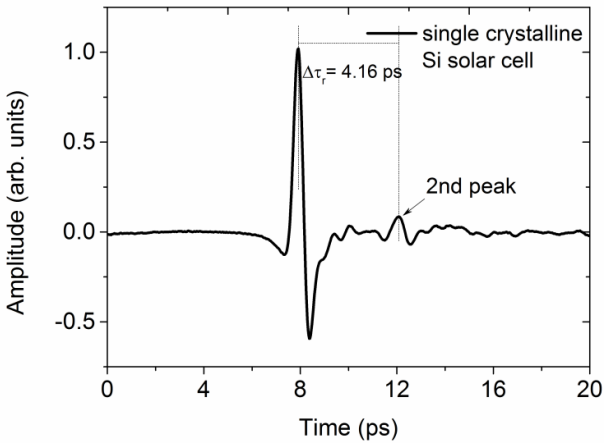

Figure 4.5: Time dependence of THz pulse reflected from single crystalline Si solar cell surface at normal incidence.

$$d = \frac{c\Delta t_{\mathrm{r}}}{2n_{\mathrm{THz}}} \tag{4.3}$$

By means of the above measurements, the thickness of the sample can be deduced with Eqs. (4.2) and (4.3). The accuracy in thickness measurement depends on the precision of the delay stage used for mechanical scanning. The positioning accuracy of the delay stage is 15 μm and the corresponding time is 0.05 ps. Therefore, the thickness of the sample measured to be 188±7 μm.

4.4.3 Single crystalline Si solar cell without AR coating layer

4.4.3.1 THz-TDS measurements without illumination

THz-TDS enables the measurement of a THz pulse transmitted through the sample and a reference pulse in the absence of the sample. Figure 4.6(a) shows the time-domain waveforms of the reference pulse and the pulse transmitted through single crystalline Si solar cell. It can be

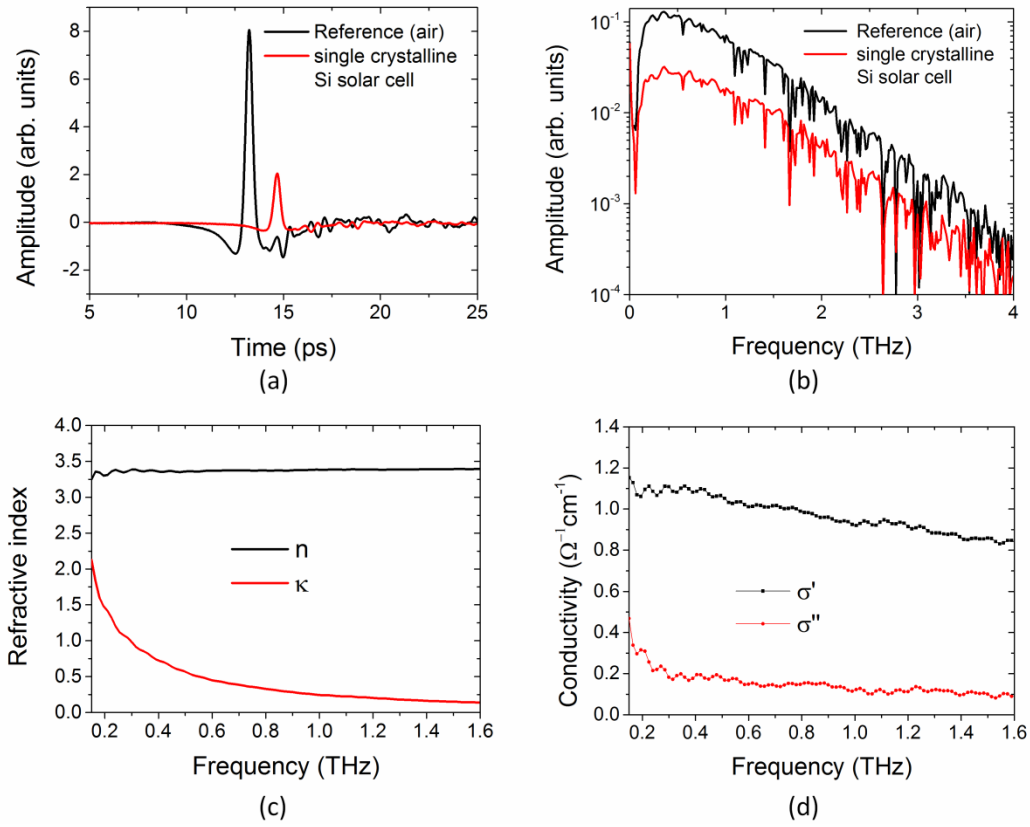

Figure 4.6: (a) Waveforms of the THz pulse transmitted through single crystalline Si solar cell and the reference pulse with no sample, (b) their amplitude spectrum, (c) complex refractive index, and (d) complex conductivity with real and imaginary part of the solar cell.

seen that the amplitude is attenuated in comparison to the reference pulse. The pulse amplitude and shape measured for the sample changed due to reflection losses, frequency dependent absorption, and dispersion of the sample. Figure 4.6(b) shows the amplitude spectra after applying fast Fourier transform (FFT) to the time-domain data. In order to determine the complex refractive index, the amplitude and phase spectra can be used in the transmission Eq. (3.4). The frequency dependence of the real part *n* and imaginary part κ (extinction coefficient) deduced complex refractive index in the THz region is shown in Fig. 4.6(c). The real part of the refractive index is related to the phase change in the medium while the imaginary part is directly related to the amplitude of the THz wave absorption in the material. The average value of the refractive index is obtained as 3.39 in the THz frequency region between 0.15 and 1.6 THz. This value is very close to the reported value of 3.41 for crystalline silicon [4]. The dielectric constant can be obtained by squaring the refractive index, and then the complex conductivity can be calculated with Eqs. (3.8) and (3.9). The dielectric constant of undoped silicon in the THz frequency region is 11.6 [15]. The real and imaginary conductivities are shown in Fig. 4.6(d). Both the real and imaginary parts of the conductivity are frequency dependent and decrease with increasing frequency in the THz region.

4.4.3.2 THz-TDS measurements with 800 nm (NIR) CW laser illumination

I studied the behavior of photoexcited carriers in the sample illuminated by a NIR CW laser at various illumination powers. In silicon, the absorption depth is about 10 μm for a 800-nm CW laser [2]. Thus, the photoexcited carriers are generated in the base region of the solar cell. Figure 4.7(a) shows the waveforms of the THz pulses transmitted through the single crystalline Si solar cell under illumination of a NIR CW laser at various powers. It can be seen that the amplitude of the THz waveforms transmitting through the photoexcited sample is greatly reduced in the presence of photoexcited carriers. By using the data analysis procedure described in section 3.4.1.1, the transmittance, complex refractive index and complex conductivity can be obtained. The transmittance of the THz wave at various illumination powers is presented in Fig. 4.7(b). The THz transmission decreases with the power of the NIR laser due to increase of photoexcited carriers in the sample. Figure 4.7(c) shows the frequency dependence of the complex refractive index at different power levels of the illumination. The real part of refractive index shows only insignificant changes while the imaginary part relatively strongly depends on the photoexcited carrier absorption. This is because of the absorption increases with increasing the photoexcited carriers. Figure 4.7(d) shows the frequency dependence of complex conductivity of the solar cell at various illumination powers. Both real and imaginary part of

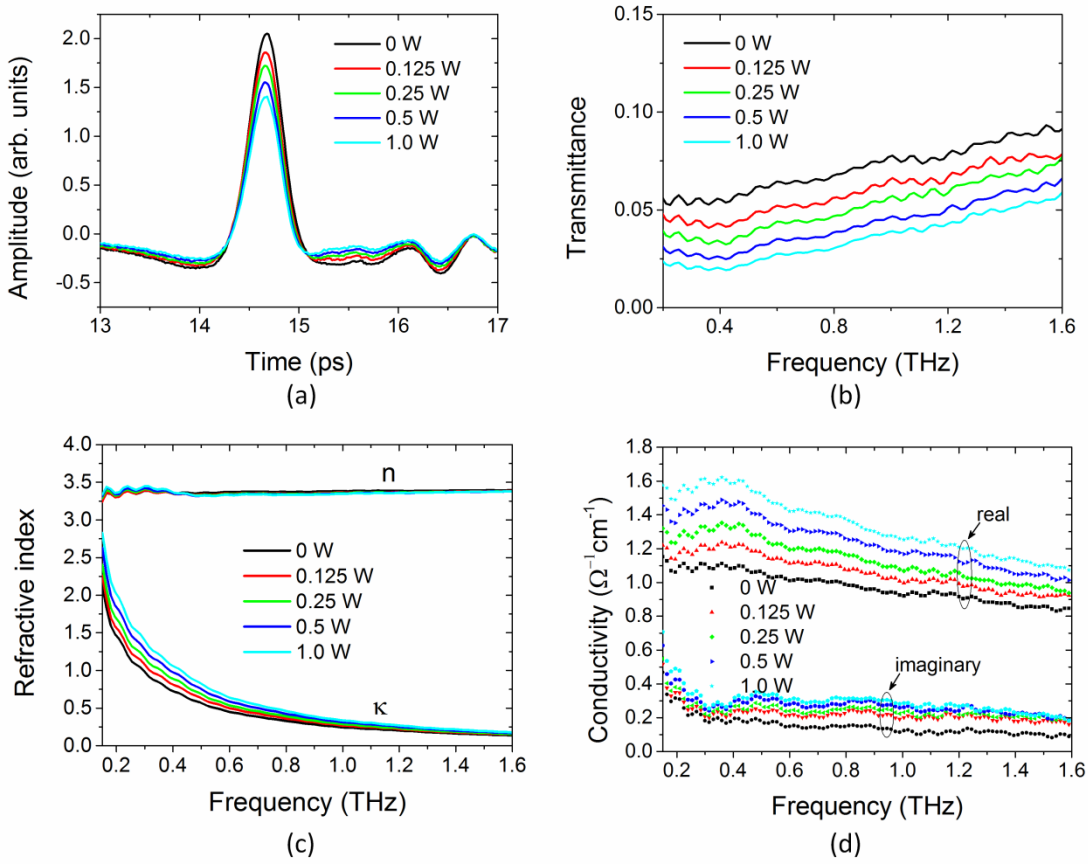

Figure 4.7: (a) Waveforms of the THz pulses transmitted through the excited single crystalline Si solar cell under NIR laser with various illumination powers, (b) frequency dependence of the transmittance, (c) complex refractive indices and (d) complex conductivities obtained from the waveforms in (a).

conductivity decreases with increasing frequency in the THz range. It is also evident that both the real and imaginary part of conductivity increases with different level of illumination due to the increase of photoexcited carriers in the sample.

The free carrier conduction in semiconductors can be well described by a simple Drude model [16]. The real part of conductivity data fitted with the Drude model using Eq. (3.19). Solid lines in Fig. 4.8 are fitting lines to the real part of conductivity at each level of illumination power using the simple Drude model. The fitting parameters DC conductivity σ_{DC} and the carrier scattering time τ were extracted from the fitted curves and presented in Table 4.3. The excess carrier density and the mobility were calculated by Eqs. (3.22) and (3.23) using the fitting parameters of σ_{DC} and τ with the effective mass $m^* = 0.26m_0$ for silicon [16].

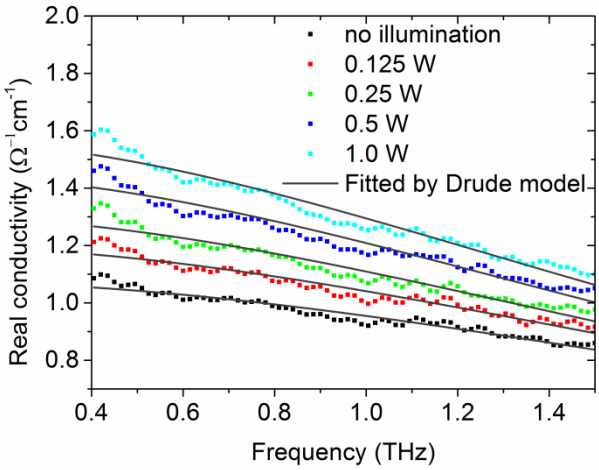

Figure 4.8: Real part of conductivity of single crystalline Si solar cell under NIR laser with various illumination powers; the solid lines are fitted curves using simple Drude model.

Table 4.3: Fitting parameters based on simple Drude model under NIR laser illumination. The excess carrier density Δn (cm^{-3}) and the mobility μ ($cm^2V^{-1}s^{-1}$) determined by σ_{DC} and τ.

NIR laser illumination power (mW)	DC conductivity; σ_{DC} (Ω^{-1} cm^{-1})	Carrier scattering time; τ (ps)	Excess carrier density; Δn (cm^{-3})	Carrier mobility; μ ($cm^2V^{-1}s^{-1}$)
125	1.20	0.062	4.0×10^{14}	417
250	1.30	0.066	6.0×10^{14}	449
500	1.45	0.071	1.4×10^{15}	478
1000	1.57	0.073	2.3×10^{15}	495

The deduced DC conductivity, excess carrier density, and mobility are plotted in Fig. 4.9 as functions of illumination power. It is shown in Fig. 4.9(a) that the DC conductivity rises nonlinearly with the illumination power of the NIR laser and tends to saturate with the increase of illumination power. It is also found in Fig. 4.9(b) that the excess carrier density increases linearly, and the mobility increases and tends to saturate with the illumination power of NIR laser. This tendency to saturate in mobility may be explained in terms of the saturation effect of photoexcited carrier trapping at the impurity region in the band gap of the solar cell [17-21]. Minority carrier traps are often present in the solar grade crystalline silicon [19, 20]. Due to laser illumination, electron-hole pairs are generated in the base (*p*-type) region of the solar cell. A part of minority electrons would be captured or scattered by impurity states which

temporarily hold electrons. As the illumination power increases, impurity states progressively trap electrons and become neutral. Therefore, the capture and scattering cross sections for electrons are reduced significantly with increasing excess carrier density, which increases the mobility of minority carriers.

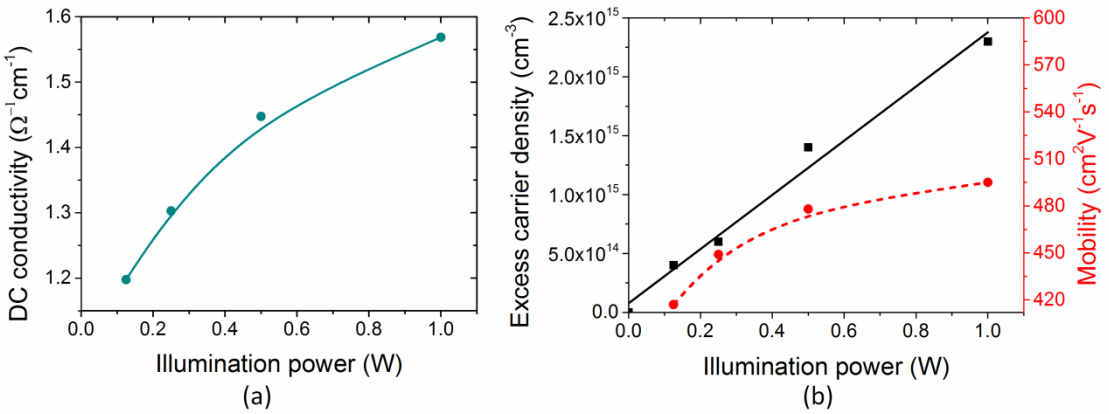

Figure 4.9: NIR laser illumination power dependence of (a) DC conductivity and (b) excess carrier density and mobility deduced from the simple Drude model fitted to the real conductivity.

4.4.3.3 THz-TDS measurements with 365 nm (UV) CW light illumination

The same experiments were performed under UV light illumination. In silicon, the penetration depth is about 0.01 μm for 365 nm light [2]. Therefore, the photoexcited carriers are generated in a surface region. Figure 4.10 shows the waveforms of the THz pulses transmitted through the solar cell under illumination of UV light at various powers. It can be seen that the illumination reduced the absorption is very small. After applying a similar analysis procedure to the

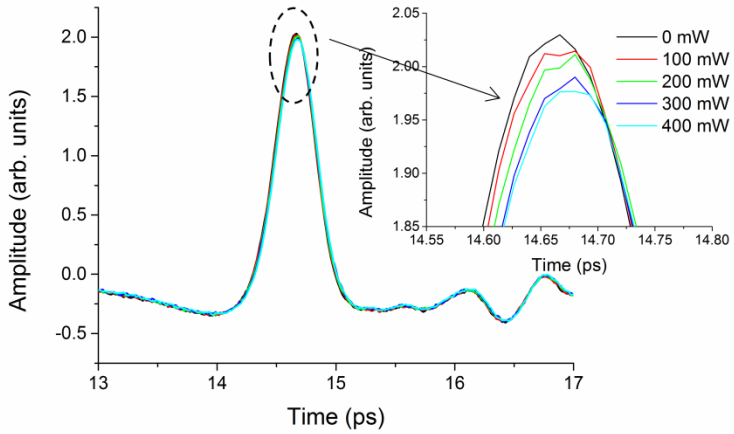

Figure 4.10: Waveforms of the THz pulses transmitted through the excited single crystalline Si solar cell under UV light illumination with various powers.

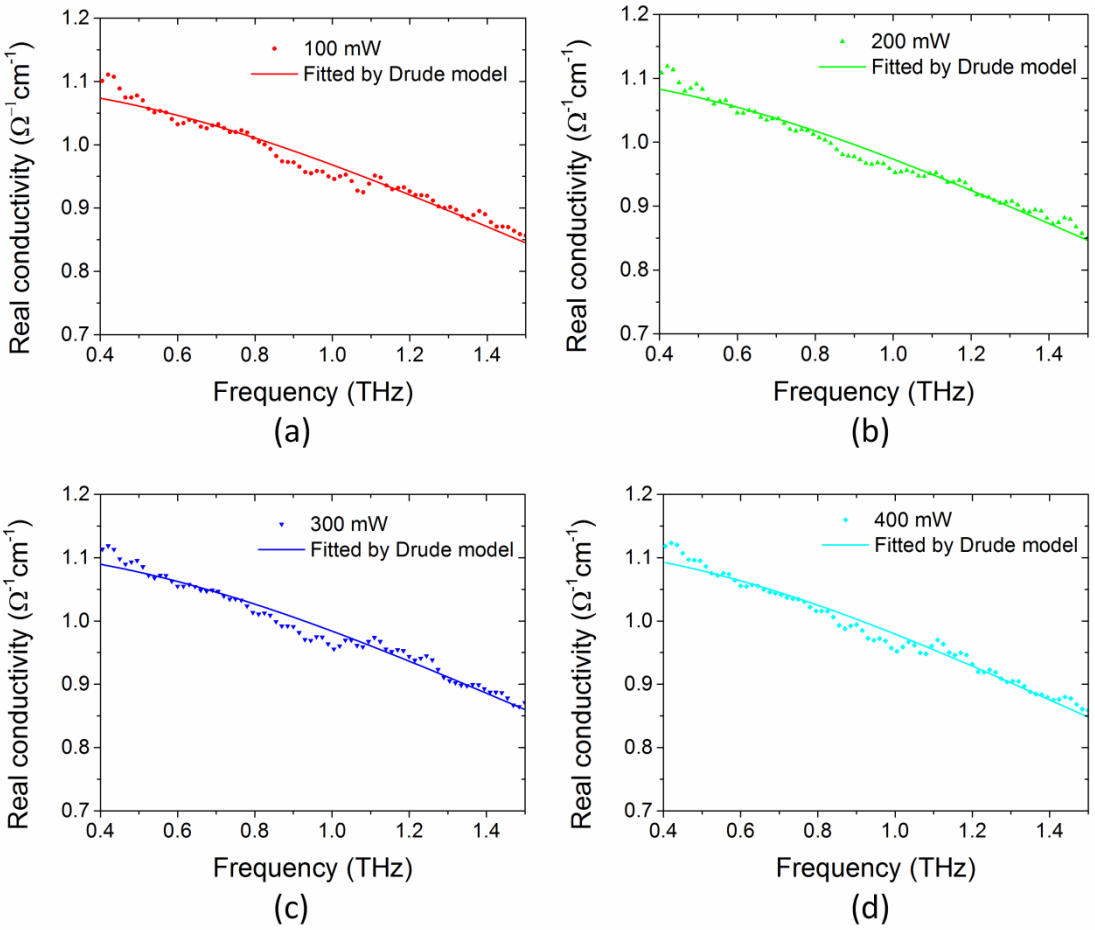

Figure 4.11: Real part of conductivity under UV light at different level of illumination. The solid lines are fitted curves with simple Drude model.

Table 4.4: Fitting parameters based on simple Drude model under UV light illuminations. The excess carrier density Δn (cm^{-3}) and the mobility μ ($cm^2V^{-1}s^{-1}$) determined by σ_{DC} and τ.

UV light illumination power (mW)	DC conductivity; σ_{DC} ($\Omega^{-1}cm^{-1}$)	Carrier scattering time; τ (ps)	Excess carrier density; Δn (cm^{-3})	Carrier mobility; μ ($cm^2V^{-1}s^{-1}$)
100	1.096	0.057	2.0×10^{14}	392
200	1.107	0.059	1.0×10^{14}	398
300	1.113	0.058	5.0×10^{14}	389
400	1.118	0.059	-3.0×10^{14}	404

time-domain waveforms data, the frequency dependence of the complex conductivity in the THz region was obtained. The frequency dependent real part of the conductivity data fitted by simple Drude model at different illumination level is shown in Fig. 4.11. From the fitting procedures, the excess carrier density and mobility were estimated using Eqs. (3.22) and (3.23), and the results are presented in Table 4.4. The excess carrier density and mobility are smaller for the UV light illumination than that for the NIR light one. These can be explained by considering the penetration depth, photoexcited carrier generation, and recombination. Due to the short penetration depth of UV light, the photoexcited carriers are generated within 10 nm from the surface, and their lifetime is strongly shorten by high surface recombination values.

4.4.4 Single crystalline Si solar cell with AR coating layer

Anti-reflection (AR) coating plays an important role for the improvement of solar cell energy conversion efficiency. It is well known that bare Si has a high surface reflection of more than 30% due to high refractive index. An efficient AR coating (layer of non-absorbing material with lower refractive index) on the surface reduces reflection and allows more light to enter into the solar cell, thereby increasing the energy conversion efficiency. THz-TDS measurements were also performed on the single crystalline Si solar cell with AR coating layer under NIR CW laser illumination.

4.4.4.1 THz-TDS measurements with 800 nm (NIR) CW laser illumination

Figure 4.12 (a) shows the waveforms of the THz pulses transmitted through the solar cell with AR coating layer under illumination of NIR CW laser at various powers. The THz amplitude decreases with increasing the illumination power. This is because the increase in illumination power resulted in higher photoexcited carriers in the solar cell and therefore greater THz amplitude attenuation due to absorption by the photoexcited carriers. Figure 4.12(b) shows the modulation of the THz transmission at different excitation powers due to an increase of photoexcited carriers in the sample. The reference signal (without sample) was also measured. In order to get the optical constants, the time-domain data converted to the frequency domain by FFT to obtain amplitude and phase spectra. After analyzing these spectra, the frequency dependent optical constants such as complex refractive index can be obtained. The deduced imaginary part of complex refractive index in Fig. 4.12(c) shows modulation due to the absorption of the photoexcited carriers. The complex conductivity data can be calculated from the complex refractive index data by Eqs. (3.8) and (3.9). Figure 4.12(d) shows the frequency dependence of complex conductivity of the solar cell at various illumination powers.

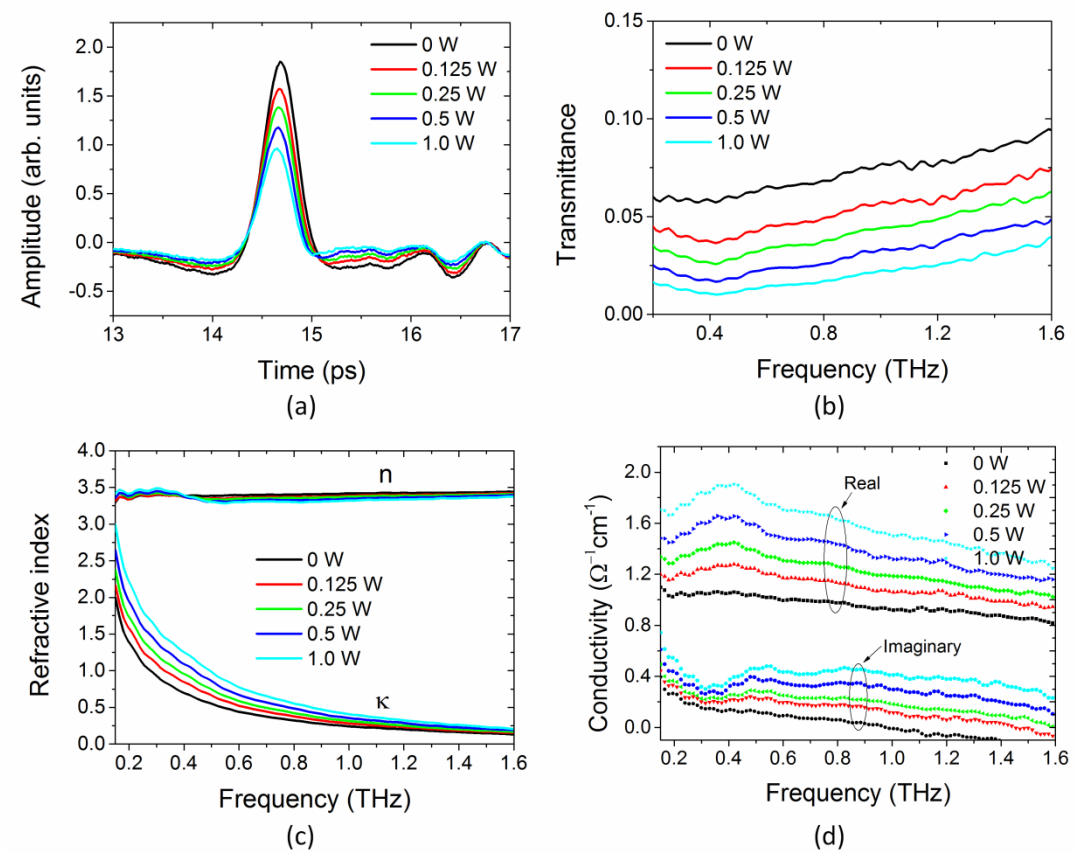

Figure 4.12: (a) Waveforms of THz pulses transmitted through the excited single crystalline Si solar cell with AR coating layer (b) transmittance, (c) complex refractive indices and (d) complex conductivities under NIR laser with various illumination powers obtained from the waveforms (a).

To extract the carrier density and mobility, the real part of conductivity data fitted with the simple Drude model. Solid lines in Fig. 4.13 are the fitted curves to the real part of conductivity at each level of NIR illumination power using the simple Drude model. The fitting parameters of the DC conductivity σ_{DC} and carrier scattering time τ were extracted from the fitting curves and presented in Table 4.5. Using Eqs. (3.22) and (3.23) with the fitting parameters, the excess carrier density and mobility can be determined. Figure 4.14 shows the NIR illumination power dependence of DC conductivity, excess carrier density, and mobility. The DC conductivity in Fig. 4.14(a) shows a nonlinear increase with the illumination power. It is evident in Fig. 4.14 (b) that the carrier density increases linearly and the mobility of the photoexcited carriers also increases nonlinearly and tends to saturate with the increase of illumination power. These behaviors are similar to the results of the non-coated sample. However, the carrier density is larger for AR coated sample. This is because the AR coating reduces the reflection by increasing the light coupling into the active region and generates more photo carriers in the solar cell.

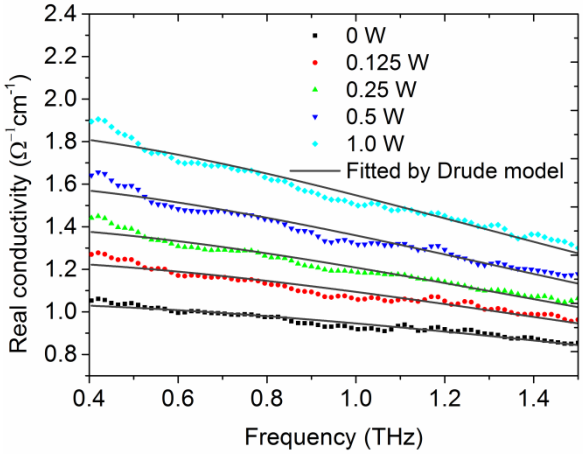

Figure 4.13: Real part of conductivity of single crystalline Si solar cell with AR coating layer under NIR laser with various illumination power; the solid lines are curves fitted with simple Drude model.

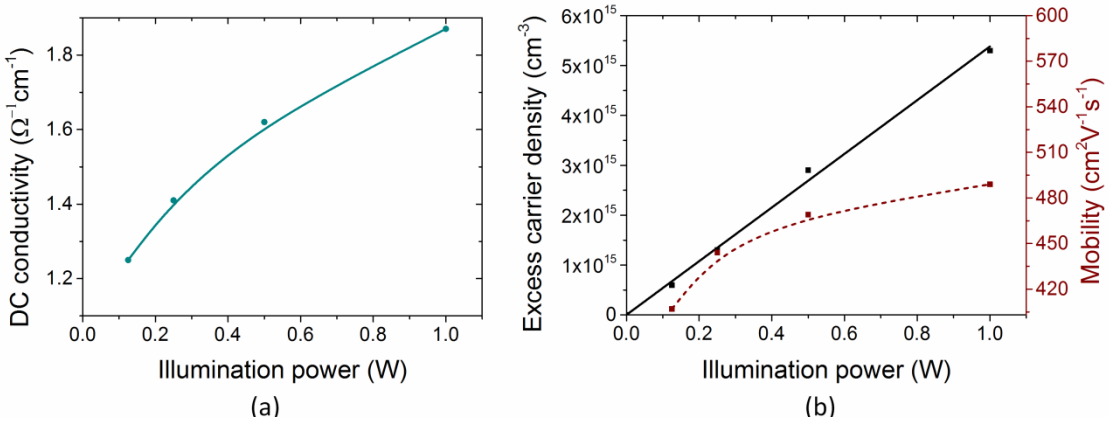

Figure 4.14: NIR laser illumination power dependence of (a) DC conductivity and (b) excess carrier density and mobility deduced from the simple Drude model fitted to the real part of conductivity of single crystalline Si solar cell with AR coating layer.

Table 4.5: Fitting parameters based on simple Drude model under NIR laser with various powers. The excess carrier density Δn (cm^{-3}) and the mobility μ ($cm^2V^{-1}s^{-1}$) determined by σ_{DC} and τ.

NIR laser illumination power (mW)	DC conductivity; σ_{DC} ($\Omega^{-1}cm^{-1}$)	Carrier scattering time; τ (ps)	Excess carrier density; Δn (cm^{-3})	Carrier mobility; μ ($cm^2V^{-1}s^{-1}$)
125	1.25	0.060	6.0×10^{14}	407
250	1.41	0.065	1.3×10^{15}	444
500	1.62	0.069	2.9×10^{15}	469
1000	1.86	0.072	5.3×10^{15}	489

4.4.5 THz-TDS rear surface measurements of single crystalline Si solar cell

Crystallographic defects and impurities are often present in the solar grade crystalline silicon. These imperfections would have a significant effect on the functionality of the device. The rough surface causes the incident light to reflect in different directions. Hence, the absorption of the incident photon is greatly reduced. THz-TDS measurements were also performed on the rear rough surface of the single crystalline Si solar cell with NIR CW laser illumination.

4.4.5.1 THz-TDS measurements with 800 nm (NIR) CW laser illumination

In these measurements, the THz pulses were transmitted from the rear surface to the front surface of the single crystalline Si solar cell. Figure 4.15 shows the waveforms of the THz pulses transmitted through the single crystalline Si solar cell under NIR illumination with various powers from the rear surface. The amplitude of the waveforms is attenuated more with the increasing illumination power due to the photoexcited carrier absorption. The reference waveform (without sample) was also measured. Time-domain waveforms were converted to the frequency-domain by FFT. These spectra were analyzed and the properties such as transmittance, complex refractive index and conductivity were calculated. It is seen from Fig. 4.16(a)-(c) that the frequency dependence of the transmittance, imaginary part of refractive index and conductivity changes in the sample due to photoexcited carriers generated by the NIR laser illumination. Figure 4.16(d) shows the real part of the conductivity data fitted with the simple Drude model.

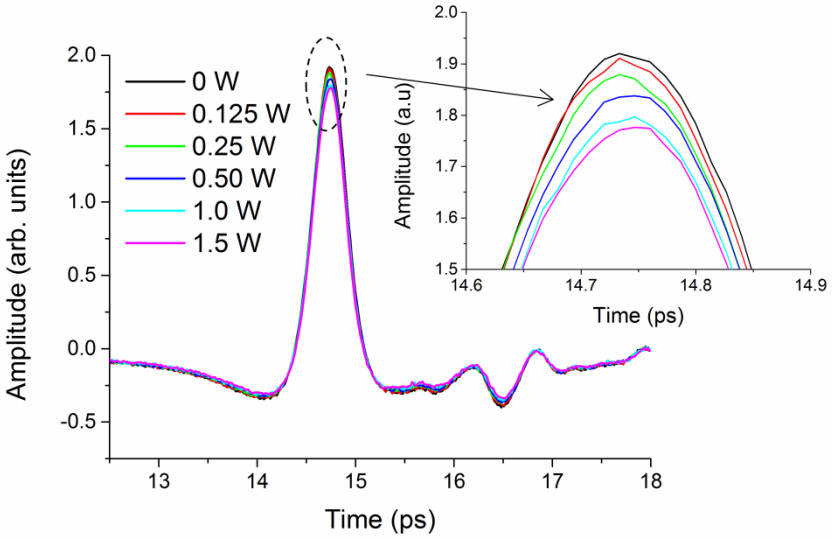

Figure 4.15: Waveforms of the THz pulses transmitted through single crystalline Si solar cell under NIR laser with various illumination powers from rear surface.

Using the fifing parameters σ_{DC} and τ, the excess carrier density and mobility were calculated by Eqs. (3.22) and (3.23) and presented in Table 4.6. From these results, it is seen that the carrier density and mobility increase with increasing illumination power, which are similar to the illumination results of the samples with and without AR coating layer. However, the value of the carrier density and mobility are smaller than those of illumination results of the samples with and without AR coating layer. For example, at 1-W illumination the carrier density decreased by one order of magnitude, and the mobility decreased by 4.7% and 5.9%, compared to the corresponding values deduced from the samples with and without AR coating layer. This is because the reflectance of rear surface is much larger than that of textured and textured with AR coating front surface [22]. Textured or textured with AR coating surface reduces the reflection of light and generated more photo carriers. The recombination in the unpolished rear rough surface is thought to be higher than that of the textured or AR coating surface, because it contains a large number of defects and impurities that act as a recombination centers, which decrease the carrier density and mobility.

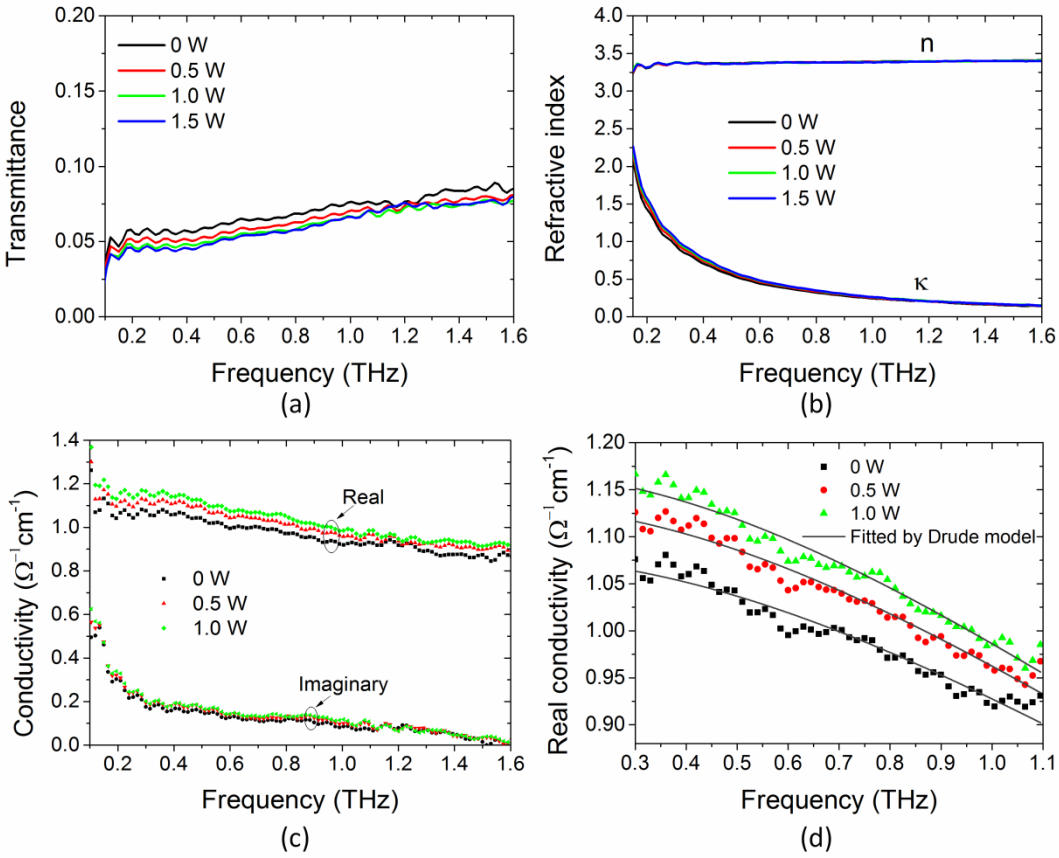

Figure 4.16: Measured (a) transmittance, (b) complex refractive index, (c) complex conductivity and (d) real part of conductivity fitted by simple Drude model under NIR laser illumination with various powers on the rear surface of single crystalline Si solar cell.

Table 4.6: Fitting parameters based on simple Drude model under NIR laser with various illumination powers on rear surface. The excess carrier density Δn (cm^{-3}) and the mobility μ ($cm^2V^{-1}s^{-1}$) determined by σ_{DC} and τ.

NIR laser illumination power (mW)	DC conductivity; σ_{DC} ($\Omega^{-1}cm^{-1}$)	Carrier scattering time; τ (ps)	Excess carrier density; Δn (cm^{-3})	Carrier mobility; μ ($cm^2V^{-1}s^{-1}$)
500	1.13	0.067	1.0×10^{14}	455
1000	1.17	0.068	2.0×10^{14}	466

4.5 Summary

In this chapter, transmission THz-TDS was used to measure optical properties of single crystalline Si solar cells during photoexcitation by NIR and UV CW light. Before THz measurement, the surface roughness of the samples was measured by AFM. The thickness of the sample was measured by terahertz peak delay techniques. The THz transmission was greatly reduced by the absorption of photoexcited carriers generated by NIR but only slightly reduced by UV light illumination. This difference in the measured response of sample to NIR and UV illumination was due to the difference in their penetration depth. The analysis of transmission data yields complex refractive index as well as complex conductivity. The conductivity showed frequency dependence and decreases with increasing frequency in the THz region. It was also found that the conductivity increases with different levels of CW light illumination power. The conductivity data were fitted with the simple Drude model, and from the fitting results, the excess carrier density and mobility were deduced. The excess carrier density was higher for AR-coated sample compared to the non-coated sample when illumination by NIR light. In both AR-coated and non-coated samples, the carrier mobility increases nonlinearly with the illumination power and tends to saturate at higher illumination power for the NIR laser. This phenomenon was explained in terms of the effect of carrier trapping in the impurity region in the band-gap of the solar cell. The carrier density for rear rough surface of the sample under NIR laser with same illumination power was one order smaller, and the mobility decreased by 4.7% and 5.9% compared to with and without AR coating sample due to the surface recombination.

References:

1. P. C. Choubey, A. Oudhia and R. Dewangan, "A review: Solar cell current scenario and future trends," *Recent Res. Sci. Technol.*, **4**, 99 (2012).
2. D. E. Aspnes and A. A. Studna, "Dielectric functions and optical parameters of Si, Ge, GaP, GaAs, GaSb, InP, InAs, and InSb from 1.5 to 6.0 eV," *Phys. Rev. B.*, **27**, 985 (1983).
3. H. Nesswetter, P. Lugli, A. W. Bett, and C. G. Zimmermann, "Electroluminescence and Photoluminescence characterization of multijunction solar cells," *IEEE J. Photovol.*, **3**, 353 (2013).
4. D. Grischkowsky, S. Keiding, M. Exter, and C. Fattinger, "Far-infrared time-domain spectroscopy with terahertz beams of dielectrics and semiconductors," *J. Opt. Soc. Am. B.*, **7**, 2006 (1990).
5. C. Zhang, B. Jin, J. Chen, P. Wu and M. Tonouchi, "Noncontact evaluation of nondoped InP wafers by terahertz time-domain spectroscopy," *J. Opt. Soc. Am. B*, **26**, A1 (2009).
6. L. V. Titova and F. A. Hegmann, "Probing ultrafast carrier dynamics and transient conductivity of semiconductors and semiconductor nanostructures using time-resolved terahertz spectroscopy," *Physics in Canada*, **65**, 101 (2009).
7. M. van Exter and D. Grischkowsky, "Optical and electronic properties of doped silicon from 0.1 to 2 THz," *Appl. Phys. Lett.*, **56**, 1694 (1990).
8. N. Nagai, M. Sumitomo, M. Imaizumi, and R. Fukasawa, "Characterization of electron- or proton-irradiated Si space solar cells by THz spectroscopy," *Semicond. Sci. Technol.*, **21**, 201 (2006).
9. J. Nelson, *The Physics of Solar Cells*, London: Imperial College Press (2003).
10. Y. Han, X. Yu, D. Wang and D. Yang, "Formation of various pyramidal structures on monocrystalline silicon surface and their influence of the solar cells," *J. Nanomater.*, Article ID 716012 (2013).
11. B. Swatowska, T. Stapinski, K. Drabczyk and P. Panek, "The role of antireflection coatings in silicon solar cells-the influence on their electrical parameters," *Optica Applicata*, Vol. XLI, No. 2 (2011).
12. Z. Xi, D. Yang, W. Dan, C. Jun, X. Li and D. Que, "Investigation of texturization for monocrystalline silicon solar cells with different kinds of alkaline," *Renew. Energy*, **29**, 2101 (2004).
13. C-Y Jen and C Richter, "Sample thickness measurement with THz-TDS: Resolution and Implications." *J Infrared Milli Terahz Waves*, **35**, 840 (2014).
14. I-S. Russe, D. Brock, K. Knop, P. kleinebudde, and J. A. Zeitler, "Validation of terahertz

coating thickness measurements using X-ray microtomography," *Mol. Pharmaceutics*, **9**, 3551 (2012).

15. K. Sakai (Ed.), *Terahertz Optoelectronics* (pp. 203-212), Berlin: Springer (2005).
16. M. Exter and D. Grischkowsky, "Carrier dynamics of electrons and holes in moderately doped silicon," *Phys. Rev. B.*, **41**, 12140 (1990).
17. E. Fabre, M. Mautref and A. Mircea, "Trap saturation in silicon solar cells," *Appl. Phys. Lett*., **27**, 239 (1975).
18. H. Y. Fan, "Effect of traps on carrier injection in semiconductors," *Phys. review*, **92**, 1424 (1953).
19. D. Macdonald and A. Cuevas, "Trapping of minority carriers in multicrystalline silicon," *Appl. Phys. Lett.*, **74**, 1710 (1999).
20. J. Schmidt and A. Cuevas, "Electronic properties of light-induced recombination centers in boron-doped Czochralski silicon," *J. Appl. Phys*., **86**, 3175 (1999).
21. D. Macdonald, M. Kerr and A. Cuevas, "Boron-related minority-carrier trapping centers in p-type silicon," *Appl. Phys. Lett*., **75**, 1571 (1999).
22. R. Barrio, N. González, J. Cárabe, J. J. Gandía, "Optimisation of NaOH texturisation process of silicon wafers for heterojunction solar-cells applications," *Solar energy*, **86**, 845 (2012).

Chapter 5: Transmission THz-TDS study on silicon wafer under light illumination

5.1 Introduction

Evaluation of minority carrier lifetime and surface recombination velocity (SRV) in a semiconductor are quite important for many semiconductor devices e.g. solar cells, *p*–*n* junctions [1]. The lifetime of photogenerated minority carriers in a base region of a solar cell greatly affects the overall conversion efficiency. Loss of carriers by recombination at the surface and interfaces reduces the energy conversion efficiency of solar cell. Thus, carrier lifetime and SRV are demanded for developing novel solar cell design. The measurements of these parameters can be performed using optical methods, where excess free carriers are generated in the sample under illumination of light. The excess carrier concentration is affected by a number of material parameters, such as the complex refractive index and conductivity. The excess carrier concentration depends on the recombination parameters. The recombination process occurs not only in the bulk but also on the surface of the sample. Most of the lifetime measurement techniques determine the effective lifetime consisting of bulk and surface components [2-4] that are difficult to separate. Separation is possible by changing the wafer thickness because the bulk and surface recombination can be written with the following expression [5]:

$$\frac{1}{\tau_{\text{eff}}} = \frac{1}{\tau_{\text{bulk}}} + \frac{2S}{d} \tag{5.1}$$

where d is the thickness of the sample, τ_{bulk} is the bulk lifetime, and S is the surface recombination velocity. As expressed in the equation, the effective lifetime depends on the surface recombination of the wafer. If the wafer is not passivated, the SRV is high which implies the effective lifetime is mainly indicates the surface characteristic of the wafer. Whereas when the wafer is well passivated, the SRV is zero and the effective lifetime is corresponded to the bulk characteristic of the wafer. In actuality, it is more useful to individually identify the bulk and surface components. This can be achieved by illuminating the wafer at different wavelengths of light to excite free carriers at different depths during measurement using QSSPC technique [6]. But this technique requires electric contacts for evaluating the electrical properties. However, a noncontact and nondestructive measurement system is attractive for such a purpose. THz-TDS, an effective noncontact and nondestructive method, is widely used to

probe a variety of physical properties in semiconductors [7, 8]. With this technique, it is possible to deduce the bulk minority carrier lifetime and SRV of a semiconductor material under ultraviolet (UV) and near infrared (NIR) light illumination. The UV light generates charge carriers at the surface region of semiconductors and their recombination is strongly influenced by the surface recombination. The NIR light is deeply absorbed and generates charge carriers in the bulk, and therefore is less sensitive to the surface. In this chapter, the optical properties such as the complex refractive index, charge carrier density and mobility as well as the parameters carrier lifetime and SRV in a silicon wafer were studied under UV and NIR light illumination.

5.2 Samples

The *p*-type (100) oriented silicon wafer with a thickness of 531 μm and a resistivity of about 150–300 Ωcm was used in this experiment. The sample was mirror polished on one side. Two kinds of samples were prepared, whose surfaces were processed with and without Ar ion bombardment using an electron cyclotron resonance (ECR) ion shower machine under the conditions: acceleration voltage of 400 V and etching time of 30s. Measurements were performed on the mirror polished surface as well as damaged surface of the samples.

5.3 Experimental procedure

The similar experimental setup for transmission THz-TDS as explained in the previous chapter was used in this work. The current system is schematically illustrated in Fig. 5.1. The optical

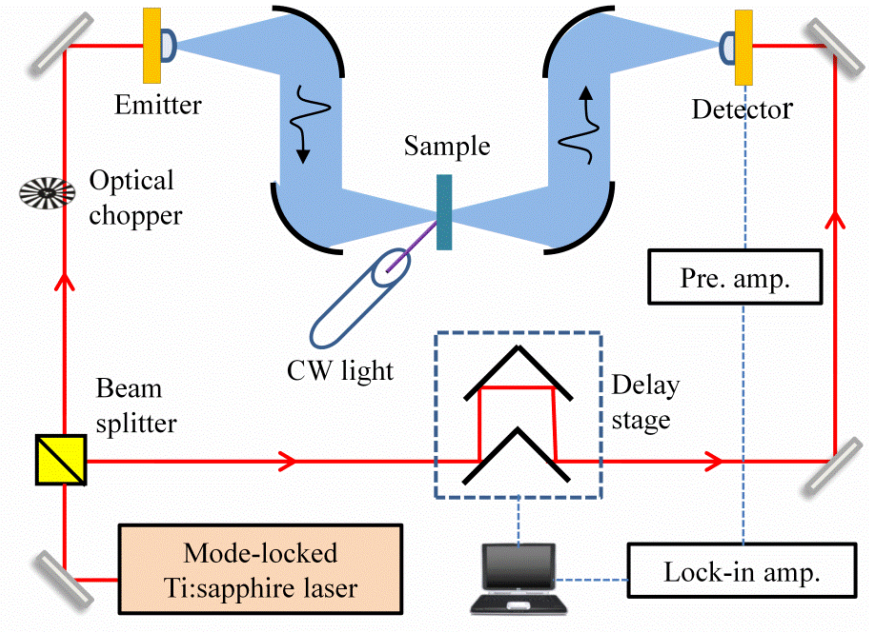

Figure 5.1: Schematic of experimental setup for THz-TDS of Si sample under CW light illumination.

pulses were generated by a mode-locked Ti:sapphire laser having a central wavelength, pulse width and repetition rate of 800 nm, 70 fs and 82 MHz, respectively. Dipole type photoconductive antennas fabricated on low temperature grown gallium arsenide (LT-GaAs) were used both as a THz emitter and detector. The Si sample was placed at the focus of the THz beam between two sets of parabolic mirrors. The spot diameter of the THz beam at the sample position was about 5 mm. In order to generate free carriers, the sample was illuminated at an incidence angle of 45° and 35° by CW light with wavelength of either 365 nm or 800 nm, respectively. The illumination area on the sample surface was 0.5 cm^2 and 0.88 cm^2 for 365 nm and 800 nm light, respectively. The area of the illumination light was larger than the THz beam spot so that the THz beam sampled a uniform region of photoexcitation. Table 5.1 summarizes the samples and measurement conditions that were used in this study. In the THz-TDS data analysis, the complex refractive index and dielectric constants as well as the conductivity were directly deduced from the waveform measurements with and without the sample and their fast Fourier transformation (FFT). The excess carrier density was estimated by the fitting to the conductivity data using a simple Drude model. The SRV was determined using the Shockley-Read-Hall (SRH) model which is explained in Chapter 2. The entire THz path from transmitter to receiver was enclosed and purged with dry nitrogen gas to reduce the relative humidity to below 8%.

Table 5.1: Experimental conditions on sample surfaces under light illumination

Sample	Surface	Illumination light
p-type Silicon wafer (resistivity: 150-200 Ωcm, thickness: 531 μm)	mirror polished surface	◆ no illumination ◆ 365 nm (UV) illumination ◆ 800 nm (NIR) illumination
	damaged surface	◆ 365 nm (UV) illumination

5.4 Results and discussion

5.4.1 Polished silicon wafer

5.4.1.1 Measurements without illumination

The time-domain waveforms measured with the THz waves transmitted through silicon wafer

sample together with the reference pulse are shown in Fig. 5.2(a). The black and red lines are the reference and transmitted pulses, respectively. Figure 5.2(b) shows the amplitude spectra in the frequency domain. The transmission coefficient of the sample was obtained by dividing the sample spectra by the reference spectra using Eq. (3.4). The complex refractive index with real part n and imaginary part κ of the sample can then be extracted from the complex transmission coefficient by solving the Eqs. (3.6) and (3.7). The measured complex refractive index of the silicon wafer sample is shown in Fig. 5.3. The real part of refractive index of the sample is 3.41, while the imaginary part of the refractive index (extinction coefficient) is 0.0023 in the frequency region from 0.1 to 2.0 THz. The absorption is mainly due to photoexcited carriers in the silicon wafer. The reported value for the refractive index of a *p*-type silicon wafer is 3.4175 [9]. The experimental value is excellent agreement with the reported value of refractive index for the *p*-type silicon wafer.

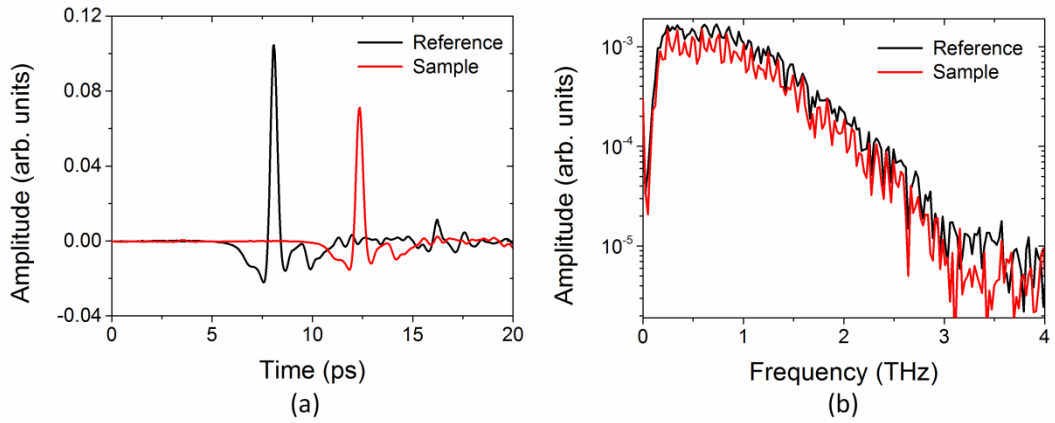

Figure 5.2: (a) Waveforms of the THz pulse transmitted through silicon wafer (red line) and reference pulse (black line) and (b) their amplitude spectra in the frequency domain.

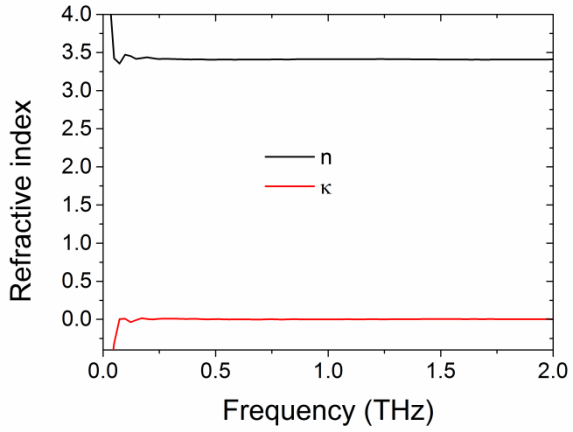

Figure 5.3: The real part n and imaginary part κ of complex refractive index obtained for a *p*-type silicon wafer.

5.4.1.2 Measurements with 365 nm (UV) CW light illumination

In this measurement, the sample was illuminated with UV light to generate carriers in the surface region. The temporal waveforms of the THz pulse transmitted through the Si wafer excited by UV light at different levels of illumination power are shown in Fig. 5.4 (a). It can be seen that the amplitude of the waveforms is smaller in the presence of UV illumination than that in its absence and it decreases with increasing illumination power. These changes occurred because the increase in illumination power resulted in higher photoexcited carrier densities in the wafer and therefore greater THz attenuation due to absorption by the photoexcited carriers. Figure 5.4(b) shows the amplitude spectra in the frequency domain. The transmission coefficient of the sample was obtained by dividing the sample spectra by the reference spectra and shown in Fig. 5.5(a). The transmittance of the THz wave decreases with increasing the illumination powers due to more photogenerated carriers in the sample. Using the Eq. (3.4) and the frequency dependent data of the screening of amplitude and phase, the complex

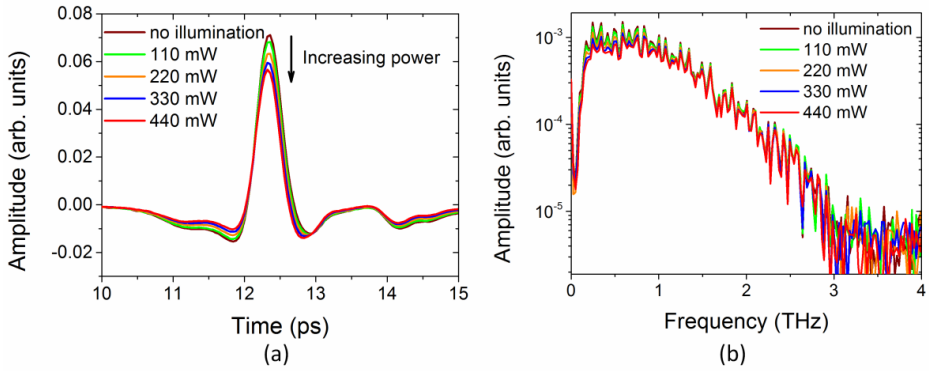

Figure 5.4: (a) THz waveforms of Si wafer at different level of UV illumination power showing efficient THz attenuation and (b) the frequency dependence of their amplitude spectrum.

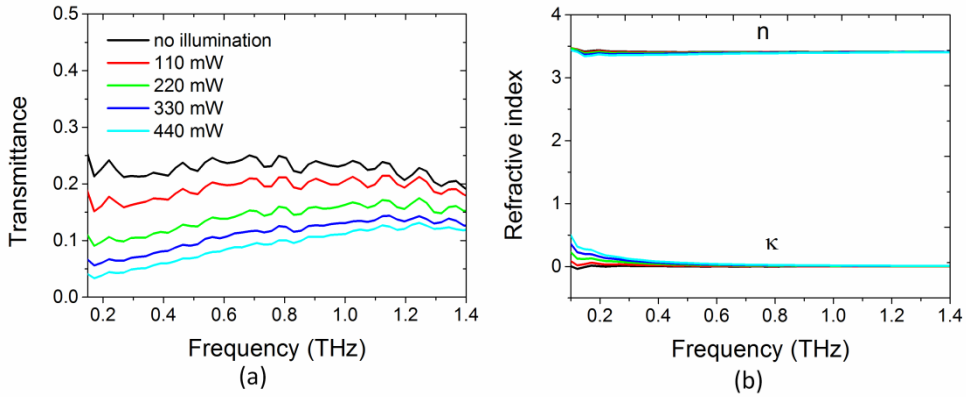

Figure 5.5: (a) Transmittance and (b) complex refractive index of Si wafer at different level of UV illumination powers.

refractive index was obtained. Figure 5.5(b) shows the complex refractive index of the silicon wafer with different illumination powers. It is seen that the real part of refractive index is independent of the photoexcited carrier density while the imaginary part in the lower frequency region (below 0.4 THz) depends with photoexcited carrier absorption.

5.4.1.3 Extraction of Drude parameters

Using the frequency dependent complex refractive index, the complex dielectric constants can be calculated using Eq. (3.8). The complex dielectric constant is directly related to the complex conductivity via Eq. (3.9). The frequency dependent real part of conductivity of the sample at different level of illumination power is shown in Fig. 5.6 (a). It is obvious that the conductivity increased as the power of the light is increased. The complex conductivity depends on the carrier density and scattering time, which is explained by a simple Drude model that provides a good description of free carrier conduction in metals and semiconductors [7]. The characteristics of doped and/or illuminated silicon are close to those of metal. Thus, the simple Drude model is suitable for explaining the free carrier conduction in optically excited silicon. Solid lines are fitted to the real part of conductivity at each level of illumination power to the simple Drude model as shown in Eq. (3.19). Fitting parameters, the carrier scattering time τ and the DC conductivity σ_{DC}, can be extracted from the best fit of the real part of conductivity data. A combination of the carrier scattering time and DC conductivity and the electron effective mass taken as $m^* = 0.26m_0$ for silicon yields the carrier density by Eq. (3.22) and presented in Table 5.2. The estimated excess carrier density is plotted in Fig. 5.6(b) as a function of the illumination power. It is found that the excess carrier density increases linearly with the level of illumination power in the power range studied.

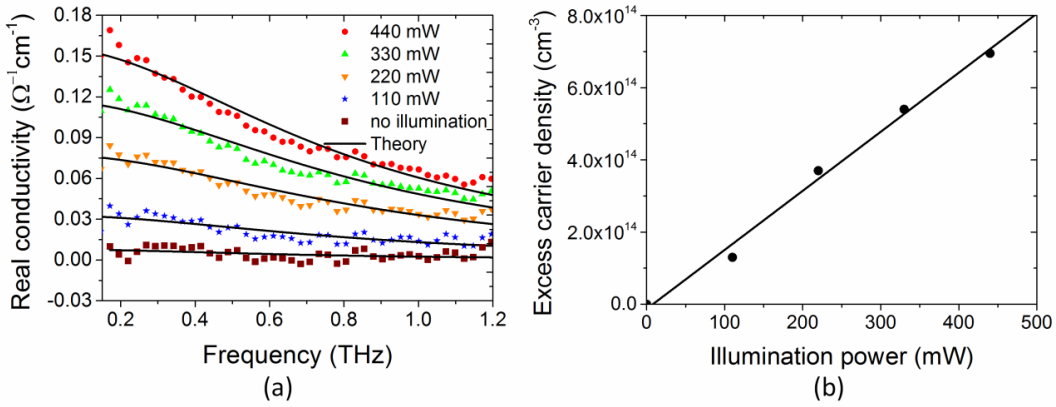

Figure 5.6: (a) Real part of conductivity of *p*-type silicon wafer at different level of UV illumination power. Solid lines are the fitted curves using simple Drude model and (b) UV illumination power dependence of excess carrier density.

Table 5.2: Fitting parameters based on simple Drude model at 365 nm with various illumination powers. The excess carrier density Δn (cm^{-3}) determined by σ_{DC} and τ.

Illumination power (mW)	DC conductivity; σ_{DC} ($\Omega^{-1}cm^{-1}$)	Carrier scattering time; τ (ps)	Excess carrier density; Δn (cm^{-3})
110	0.157	0.20	1.3×10^{14}
220	0.117	0.19	3.7×10^{14}
330	0.078	0.18	5.39×10^{14}
440	0.033	0.19	6.95×10^{14}

5.4.1.4 Effect of UV illumination on SRV

At the surface of silicon, impurities and crystalline defects are often present. These may increase surface recombination in a silicon wafer. The recombination of carriers at the surface is usually characterized by the surface recombination velocity. The SRV is denoted as *S*, defined as the ratio of recombination rate per unit area per unit time (U_s) to the excess carrier concentration in the surface region (Δn_s):

$$S = \frac{U_s}{\Delta n_s} \tag{5.2}$$

Surface recombination via defect levels is described by SRH theory, and the net recombination rate at the surface is given by [10]:

$$U_s = \frac{\sigma_p \sigma_n v_{th} N_{st} [p_s n_s - n_i^2]}{\sigma_n [n_s + n_i e^{(E_t - E_i)/kT}] + \sigma_p [p_s + n_i e^{(E_i - E_t)/kT}]} \tag{5.3}$$

For simplicity, if we assume all the centers are located at energy $E_t = E_i$ and the same capture cross sections for electrons and holes, $\sigma_n = \sigma_p = \sigma$, Eq. (5.3) express as:

$$U_s = \sigma v_{th} N_{st} \frac{p_s n_s - n_i^2}{n_s + p_s + 2n_i} \tag{5.4}$$

where n_s and p_s are the electron and hole density at the surface, n_i is the intrinsic carrier concentration, v_{th} the thermal velocity of carrier and N_{st} the density of surface states. For *p*-type silicon, Eq. (5.4) can be rewritten as

$$U_{\mathrm{s}} = \sigma v_{\mathrm{th}} N_{\mathrm{st}} \frac{N_{\mathrm{A}}}{n_{\mathrm{s}} + p_{\mathrm{s}} + 2n_{\mathrm{i}}} [n_p(x_{\mathrm{d}}) - n_{po}] \tag{5.5}$$

$$\text{where } S = \sigma v_{\mathrm{th}} N_{\mathrm{st}} \frac{N_{\mathrm{A}}}{n_{\mathrm{s}} + p_{\mathrm{s}} + 2n_{\mathrm{i}}} \tag{5.6}$$

Here N_{A} is the acceptor concentration, N_{po} is the equilibrium minority carrier concentration, and $n_p(x_d)$ is the minority carrier concentration at a distance x_{d} from the surface.

In this experiment, UV light was used to illuminate the silicon wafer, which has an optical absorption coefficient of about 10^6 cm^{-1} and the corresponding penetration depth is 10 nm [11]. Thus, the photoexcited carriers are generated at the surface region, and the concentration of electrons and holes are equal ($n_s = p_s = \Delta n$). An estimation of the diffusion length from the values of electron diffusion coefficient, 36 cm^2s^{-1}, and the typical electron lifetime, 2.5 μm of silicon gives the diffusion length ~0.3 cm [12]; this value is much larger than wafer thickness. This means that the gradient of electron distribution is very low. Therefore, the photoexcited carrier density can be considered as a surface carrier density. Then, the value of SRV can be calculated by using the photoexcited carrier density by Eq. (5.6). For the calculations, doping density N_{A} = 5×10^{15} cm^{-3}, surface trap density N_{st} = 10^{11} cm^{-2}, carrier capture cross section σ_{s} = 10^{-15} cm^2, and thermal velocity of carrier v_{th} = 10^7 cms^{-1} were assumed [10]. The calculated value of SRV in the presence of UV illumination is shown in Fig. 5.7. It can be seen that the SRV decreases linearly with an increase of the excess carrier density. This indicates that UV illumination is effective for reducing the effect of surface recombination in the silicon wafer, depending on the excess carrier density.

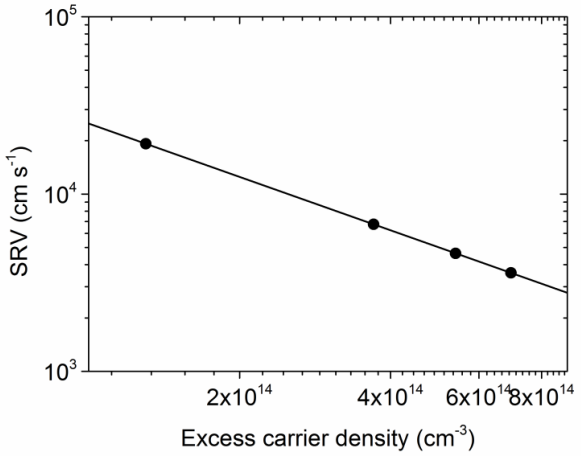

Figure 5.7: Excess carrier density dependence of surface recombination velocity (SRV) of *p*-type silicon wafer.

Bare (nonpassivated) Si surfaces have very high SRV in the range of 10^3 to 10^4 cms^{-1} or higher. Bail and Brendel measured the SRV values (593±167) ms^{-1} for nonpassivated Si wafer by the quasi-steady-state photoconductance technique [6]. Usually, thermal oxidation is used for surface passivation to reduce the SRV. An oxidized Si surface has been reported with SRV from 0.25 [5] to 45.8 cms^{-1} [13]. Ling and Ajmera reported that the value of SRV for a polished etched silicon surface is 500–1400 cms^{-1} [14]. In this experiment, the values of SRV are much smaller than that for nonpassivated and larger than that for a passivated silicon wafer. This means that UV illumination partially passivates the surface of the silicon wafer. This tendency corresponds to results reported elsewhere [15-18], where the effective carrier lifetime increased under UV irradiation.

The effect of UV illumination on SRV can be discussed with the energy band diagram of the *p*-type silicon wafer. Fig. 5.8(a) and (b) show the energy band diagram of a *p*-type silicon wafer without and under UV light illumination, respectively. Silicon wafers are normally covered with native oxide layers formed at room temperature at the oxide/silicon interface. The native oxide layer contains a positive charge at the oxide/silicon interface, as indicated in Fig. 5.8(a). Under UV light illumination [Fig. 5.8(b)], the photoexcited carriers are generated at the surface region. The minority electrons are captured by the oxide layer and consequently decrease the surface band bending and resulting in an increase in the surface potential. [16, 18]. This change in surface potential in the presence of UV illumination results in a decrease of SRV in the *p*-type silicon wafers.

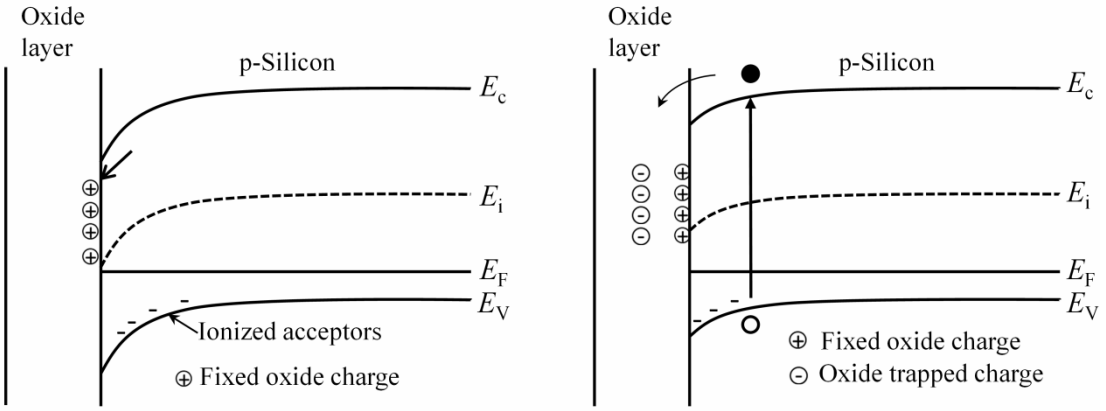

Figure 5.8: Energy band diagram of *p*-type silicon (a) without illumination and (b) under UV illumination

5.4.1.5 Measurements with 800 nm (NIR) CW laser illumination

The same sample was measured under NIR laser illumination. At this wavelength, the absorption coefficient is 10^3 cm^{-1} [11]; so that the photoexcited carriers are generated in the bulk region of the sample. Figure 5.9(a) shows the waveforms of the THz pulses transmitted through the silicon wafer measured by varying the illumination laser power from 0 to 1000 mW. The reference waveform (no sample) was also measured. Applying the analysis procedure described in section 3.4 to the time-domain waveforms, the conductivity was obtained. Figure 5.9(b) shows the real part of conductivity for the silicon wafer and the conductivity data fitted by simple Drude model at different level of NIR illumination powers. The excess carrier density was calculated from the fitting measurement results using Eq (3.22) and presented in Table 5.3.

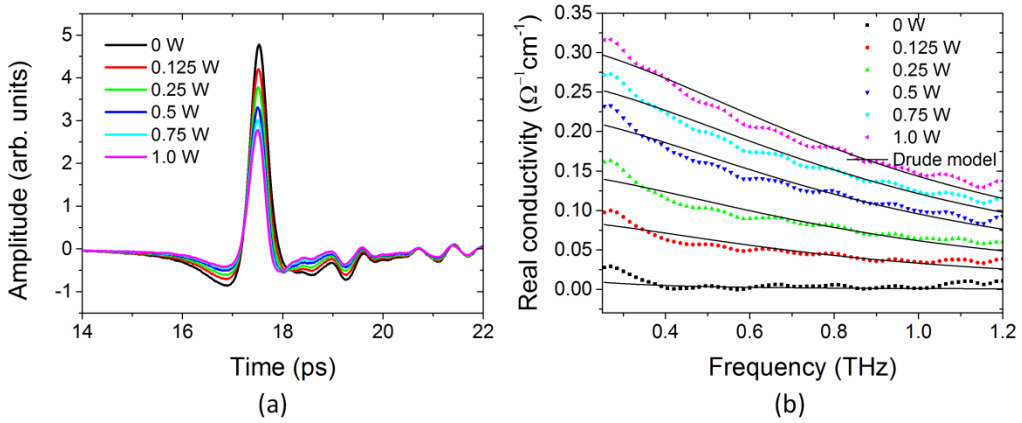

Figure 5.9: (a) Waveforms of the THz pulses transmitted through the Si wafer illuminated by NIR laser and (b) the real part of conductivity of the Si wafer fitted by simple Drude model. The excitation powers are listed in the graph.

Table 5.3: Fitting parameters based on simple Drude model under NIR laser with various illumination powers. The excess carrier density Δn (cm^{-3}) determined by σ_{DC} and τ.

Illumination power (mW)	DC conductivity; σ_{DC} ($\Omega^{-1}cm^{-1}$)	Carrier scattering time; τ (ps)	Excess carrier density; Δn (cm^{-3})
125	0.091	0.211	3.72×10^{14}
250	0.152	0.193	7.01×10^{14}
500	0.226	0.186	1.09×10^{15}
750	0.271	0.177	1.38×10^{15}
1000	0.320	0.176	1.65×10^{15}

5.4.1.6 Carrier recombination lifetime

The excess carrier concentration of silicon depends on the wavelength of illumination light. The penetration depth of 800 nm (NIR) light for silicon is about 10 μm. The photoexcited carriers are generated in the deep level, and their recombination is affected at the surface and in the bulk of the wafer. The effective lifetime of excess carriers is generally defined as [19]:

$$\frac{1}{\tau_{\text{eff}}} = \frac{1}{\tau_{\text{bulk}}} + \frac{1}{\tau_{\text{surf}}}, \tag{5.7}$$

where τ_{bulk} and τ_{surf} represent the carrier lifetime in the bulk and the surface effect on lifetime, respectively. Accordingly, the increase in τ_{eff} can be attributed to the increase in the τ_{surf}, or decrease in the SRV. When the surfaces are well passivated, the effect of surfaces can be neglected and then the effective lifetime, $\tau_{\text{eff}} = \tau_{\text{bulk}}$. For high SRV (S > 10^5 cms^{-1}), the lifetime measured with IR becomes independent of the SRV and depends only on the bulk lifetime and minority carrier diffusion length. The effective lifetime τ_{eff} of the charge carriers in the silicon wafer under steady state illumination conditions is calculated by using the following equation:

$$\tau_{\text{eff}} = \frac{\Delta n}{G}, \tag{5.8}$$

where Δn the excess carrier density, and G is the carrier generation rate defined as the following expression:

$$G = \Phi(1 - R)\frac{1}{\delta}, \tag{5.9}$$

where the photon flux Φ defined as the number of photons per unit time per unit area, the reflectivity R = 0.23 determined at an incident angle of 35° (in this experiment) by using the Fresnel equation [20] and the absorption length δ = 10 μm for silicon at the wavelength of 800 nm. The carrier generation rate for 1 mW is estimated to be 6.2×10^{18} $\text{cm}^{-3}\text{s}^{-1}$. The excess carrier density and their effective lifetime under NIR illumination light are shown in Fig. 5.10. It can be seen in Fig. 5.10(a) that the excess carrier density linearly increases with the illumination powers. As shown in Fig. 5.10(b), the effective lifetime decreases as the excess carrier density increases for *p*-type silicon wafer.

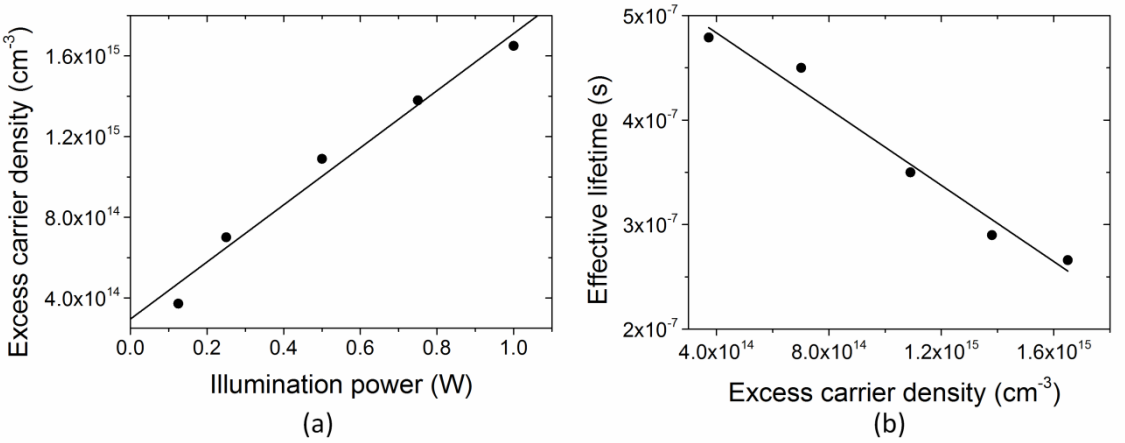

Figure 5.10: NIR illumination power dependence of excess carrier density and (b) the excess carrier density dependence of effective lifetime of *p*-type silicon wafer.

5.4.2 Damaged/rough silicon wafer

5.4.2.1 Measurements with 365 nm (UV) CW light illumination

The silicon wafer with randomly rough surface due to the ion bombardment was also measured. The surface may have influence in the measured optical properties and recombination parameters. Figure 5.11(a) shows the waveforms of the THz pulses transmitted through the sample illuminated by UV light with various powers. The sample properties can then be obtained by analyzing the time-domain waveforms. The results of frequency dependent real part of conductivities are plotted in Fig. 5.11(b). At the same illumination power, conductivity is much smaller compared to the polished wafer. This is because the surface recombination rate at

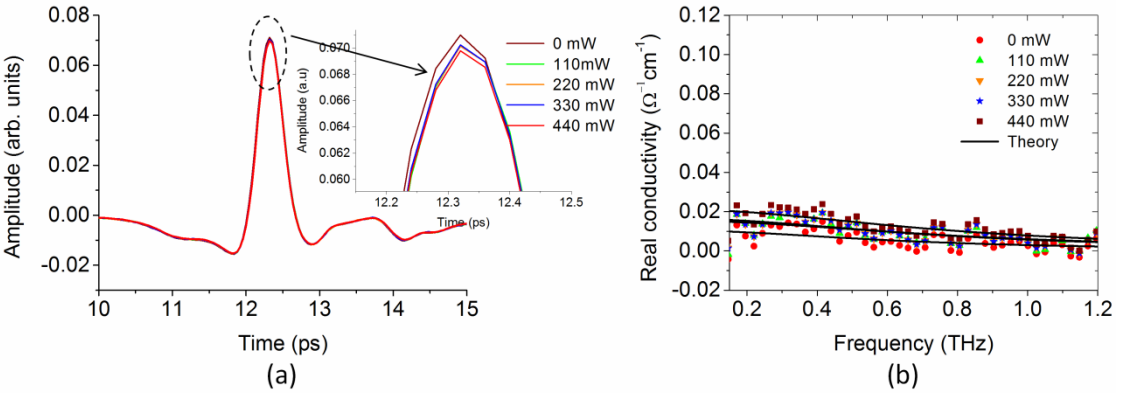

Figure 5.11: (a) Waveforms of the THz pulses transmitted through the damaged silicon wafer illuminated by UV light and (b) the real part of conductivity of the sample fitted by simple Drude model. The excitation powers are listed in the graph.

Table 5.4: Fitting parameters based on simple Drude model at 365 nm with various illumination powers. The excess carrier density Δn (cm^{-3}) determined by σ_{DC} and τ.

Illumination power (mW)	DC conductivity; σ_{DC} ($\Omega^{-1}cm^{-1}$)	Carrier scattering time; τ (ps)	Excess carrier density; Δn (cm^{-3})
110	0.015	0.20	5.96×10^{13}
220	0.016	0.22	5.82×10^{13}
330	0.016	0.21	5.93×10^{13}
440	0.021	0.21	8.14×10^{13}

the rough surface is much faster than that at the polished surface. The solid lines in Fig. 5.11(b) are theoretical fits using simple Drude model. From the fitting results, the carrier density can be calculated and presented in Table 5.4. The carrier density decreased by one order of magnitude compared with polished wafer. As mentioned earlier, the SRV depends not only on the surface charge density but also on the surface trap density. The typical value of surface trap density is 10^{11} cm^{-2} for polished wafer. This value would be higher for the rough surface of the wafer. An estimation of the SRV from the higher surface trap density and the measured excess carrier density using Eq. (5.6) gives much higher SRV for a rough surface of wafer than that of a polished surface of the wafer.

5.5 Summary

In this chapter, the transmission THz-TDS was applied to study the optical properties and recombination parameters of photoexcited carriers in a *p*-type silicon wafer under UV and NIR light illumination. The THz transmission was greatly attenuated by the photoexcited carriers generated both UV and NIR light. From the THz time-domain data, the optical properties such as complex refractive index and conductivity were obtained. The excess carrier density was determined from the fitting results to the real part of conductivity data using simple Drude model. Under UV light illumination, the excess carrier density considered as surface carrier density, and the surface carrier density dependence of SRV was extracted by SRH model. It was found that the SRV is greatly reduced in the presence of UV light and depends strongly on the excess carrier density at the surface region. This phenomenon was explained with the energy band diagram of the *p*-type silicon wafer under UV illumination. The effective lifetime of the excess carriers generated by the NIR illumination was calculated under steady state conditions.

The effective lifetime was found to be ~10^{-7} seconds and depends strongly on the excess carrier density. The excess carrier density was one order of magnitude lower for rough surface than that of polished surface. We also observed high surface recombination for rough silicon surface.

References

1. D. K. Schroder, "Carrier lifetimes in silicon," *IEEE Trans. Electron Devices*, **44**, 160 (1997).
2. J. Linnros, "Carrier lifetime measurements using free carrier absorption transients. I. Principle and injection dependence," *J. Appl. Phys.*, **84**, 275 (1998).
3. J. Schmidt and A. G. Aberle, "Accurate method for the determination of bulk minority-carrier lifetimes of mono- and multicrystalline silicon wafers," *J. Appl. Phys.*, **81**, 6186 (1997).
4. R. A. Sinton and A. Cuevas, "Contactless determination of current-voltage characteristics and minority-carrier lifetimes in semiconductors from quasi-steady-state photoconductance data," *Appl. Phys. Lett.*, **69**, 2510 (1996).
5. E. Yablonovitch, D. L. Allara, C. C. Chang, T. Gmitter and T. B. Bright, "Unusually low surface recombination velocity on silicon and germanium surfaces," *Phys. Rev. Lett.*, **57**, 249 (1986).
6. M. Bail and R. Brendel, "Separation of bulk and surface recombination by steady state photo conductance measurements," *16th European Photovoltaic Solar Energy Conference*, Glasgow (2000).
7. M. Exter and D. Grischkowsky, "Carrier dynamics of electrons and holes in moderately doped silicon," *Phys. Rev. B*, **41**, 12140 (1990).
8. T. Jeon and D. Grischkowsky, "Nature of conduction in doped silicon," *Phys. Rev. Lett.*, **78**, 1106 (1996).
9. J. Dai, J. Zhang, W. Zhang, and D. Grischkowsky, "Terahertz time-domain spectroscopy characterization of the far-infrared absorption and index of refraction of high-resistivity, float-zone silicon," *J. Opt. Soc. Am. B*, **21**, 1379 (2004).
10. A. S. Grove, *Physics and Technology of Semiconductor Devices*, chap. 5, New York: J. Wiley & Sons (1962).
11. D. E. Aspnes and A. A. Studna, "Dielectric functions and optical parameters of Si, Ge, GaP, GaAs, GaSb, InP, InAs, and InSb from 1.5 to 6.0 eV," *Phys. Rev. B*, **27**, 985 (1983).
12. S. M. Sze, *The physics of semiconductor device*, New York: John Wiley and Sons (1981).
13. M. J. Kerr and A. Cuevas, "Very low bulk and surface recombination in oxidized silicon wafers," *Semicond. Sci. Technol.*, **17**, 35 (2002).
14. Z. G. Ling and P. K. Ajmera, "Measurement of bulk lifetime and surface recombination velocity by infrared absorption due to pulsed optical excitation," *J. Appl. Phys.*, **69**, 519 (1991).

15. K. Katayama, Y. Kirino, K. Iba and F. Shimura, “Effect of ultraviolet light irradiation on noncontact laser microwave lifetime measurement,” *Jpn. J. Appl. Phys.*, **30**, 1907 (1991).
16. K. Katayama and F. Shimura, “Mechanism of ultraviolet irradiation effect on Si-SiO_2 interface in silicon wafers,” *Jpn. J. Appl. Phys.*, **31**, 1001 (1992).
17. W. P. Lee, Y. L. Khong, M. R. Muhamad and T. Y. Tou, “The effect of ultraviolet irradiation on the minority carrier recombination lifetime of oxidized silicon wafers,” *J. Electrochem. Soc.*, **144**, 103 (1997).
18. W. P. Lee and Y. L. Khong, “Laser microwave photoconductance studies of ultraviolet-irradiated silicon wafers,” *J. Electrochem. Soc.*, **145**, 329 (1998).
19. Y. Arafat, F. M. Mohammedy, and M. M. S. Hassan, “Optical and other measurement techniques of carrier lifetime in semiconductors,” *Int. J. Optoelect. Eng.*, **2**, 5 (2012).
20. T. D. Dorney, R. G. Baraniuk, and D. M. Mittleman, “Material parameter estimation with terahertz time-domain spectroscopy,” *J. Opt. Soc. Am. A*, **18**, 1562 (2001).

Chapter 6: Reflection THz-TDS study on silicon and solar cells

6.1 Introduction

THz-TDS has already been proven as a powerful tool to measure optical constants of many materials in the time-domain. This system works in either transmission or reflection modes. Transmission THz system is applicable only for transparent materials. This system cannot be used for some materials such as liquids and metallic materials due to their high absorption and reflection. Additionally, some samples are optically thick and therefore cannot transmit radiation in the THz region. Therefore, in the case of samples that are opaque in the THz frequency range, the reflection THz-TDS is required. Moreover, this system has no thickness limitation of the samples because this technique measures only the reflected THz pulse from the surface of the sample. In the reflection system, a reference measurement is also required which can be obtained by using the reflection from a metallic mirror with known reflectivity. There are many materials reported in the literature that have been measured by reflected THz pulses [1-5]. The main difficulty of THz reflection measurement is the phase error due to misplacement of the reflected surface [6]. Any difference between the relative position of the sample and the reference mirror will introduce an error in the phase. This leads to large errors in the determined optical constants [7]. Thus, the sample and the reference mirror have to be placed precisely in the same position. In most of the reported systems, THz pulses illuminate the surface of a sample at a non-normal angle of incidence [8, 9]. However, the geometry of normal incidence [6, 10] is helpful for easy adjustment and data analysis. This geometry is also favorable for both spectroscopy and imaging. Since the solar cells are opaque in the THz radiation, the reflection THz-TDS is suitable for measuring the optical constant. In addition, THz reflection image provide structural information and can detect defects if they are present. In this chapter, reflection THz-TDS with normal incidence was applied to study the optical properties such as reflectance and refractive index in a silicon wafer and single crystalline Si solar cells, and imaging of a polysilicon solar cell.

6.2 Samples

Four samples were used in this work. These include a *p*-type (100) silicon wafer with a resistivity value of 700-2000 Ωcm, two single crystalline Si solar cells and a polysilicon solar

cell. The thickness of the silicon sample was 622 µm. The solar cell samples consist of *p*-type base and *n*-type emitter to create *p*–*n* junction. One single crystalline Si solar cell had no electrodes. Table 6.1 contains the samples and their THz reflection measurement conditions.

Table 6.1 Samples and their measurement conditions

Sample	Surface	THz reflection measurement condition
Silicon wafer	polished surface	no illumination
Single crystalline Si solar cell	front surface	◆ no illumination ◆ 365 nm (UV) illumination ◆ 800 nm (NIR) illumination
Single crystalline Si solar cell (no electrodes)	back surface	no illumination

6.3 Experimental procedure

A reflection terahertz time-domain spectroscopy (reflection THz-TDS) system was used for the measurements. The schematic configuration of the experimental setup for the reflection

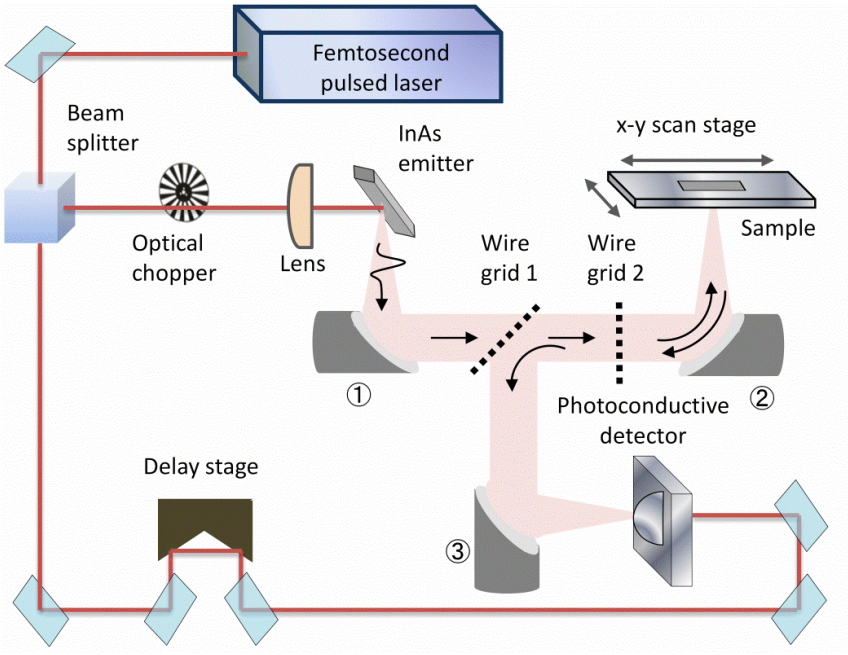

Figure 6.1: Schematic experimental setup for reflection-type THz-TDS employed in the present study

THz-TDS is shown in Fig. 6.1. A mode-lock Ti:sapphire femtosecond laser was used as an optical source. It provided 70 fs pulses and a wavelength of 800 nm at a repetition rate of 82 MHz. The laser beam was split into the pump beam and probe beam by a beam splitter. The pump beam was illuminated a (100) InAs THz emitter at an incident angle of 45° to generate THz pulses. The generated THz pulses were focused on the sample or a gold-coated mirror surface with two parabolic mirrors, and the reflected THz pulses from the surface were guided to the detector by a wire grid (wire grid 1) and a third parabolic mirror. The probe beam passes through a variable time-delay stage and was focused on a photoconductive dipole antenna fabricated on a low-temperature-grown GaAs to detect the THz pulses. The THz signal was read by a lock-in amplifier from the detector at ~2 KHz rate. The THz waveform was obtained by scanning the delay line. For imaging, the time-delay stage was fixed at the maximum amplitude of the THz signal and the reflection image was obtained by two-dimensional scanning of the sample. The detail data analysis procedures are described in section 3.4.2.

Since the phase of the signal depends on the position of the reflected surface, it is necessary to place a sample and a reference mirror exactly in the same position. Otherwise, a small displacement results in a large error in the calculated optical constants [11]. To minimize error due to misplacement, a special movable sample holder was used normal to the THz beam. The reference mirror and sample were placed on the sample holder and changed their positions using a computer controlled *x*-*y* stage. This allows the reflection measurements with almost no phase errors.

6.4 Results and discussion

6.4.1 Measurements of silicon wafer

To check the accuracy of the system, a high resistivity *p*-type silicon wafer was measured. The measurements were carried out at room temperature with regular lab environment. Two types of measurements were performed. For reference measurement, the THz signal reflected from the gold mirror was recorded. Figure 6.2 (a) shows the temporal waveforms measured with the silicon wafer and reference mirror. Figure 6.2 (b) shows their amplitude spectrum in the frequency-domain measured by fast Fourier transform (FFT). The amplitude of the waveforms reflected from the silicon sample and their FFT spectra are attenuated due to frequency dependent absorption and dispersion of the sample.

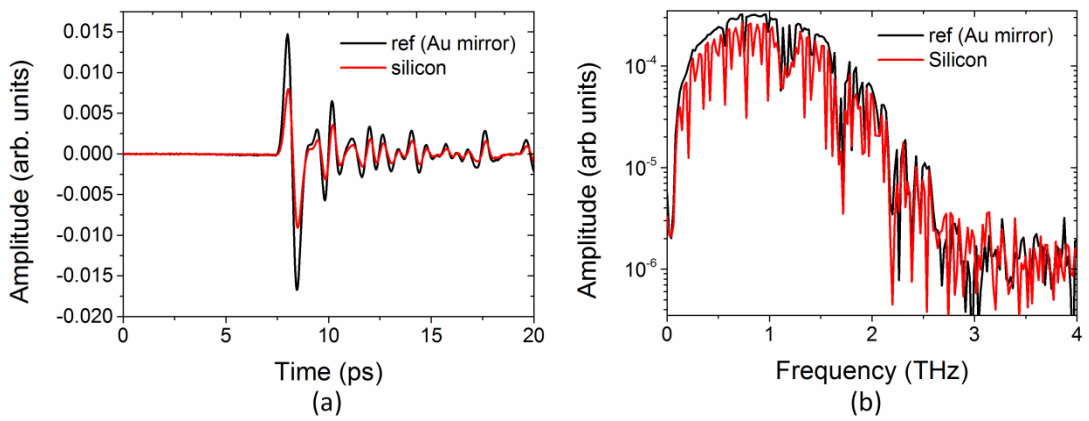

Figure 6.2: (a) Terahertz temporal waveforms of reference and *p*-type high resistivity silicon wafer, and (b) corresponding amplitude spectra in the frequency region.

The reflection coefficient of the sample can be obtained by using the ratio between the reference and the sample amplitude spectra of reflected THz signals by Eq. (3.24). The reflectance can be obtained by squaring the reflection coefficient of the sample. It is noted that the reflectance is independent of misplacement phase error. Figure 6.3 present the reflectance of the experimental data and shows almost flat in the THz frequency range from 0.1 to 1.5 THz. The average magnitude of the reflectance for the *p*-type high resistivity silicon wafer is 0.29. This value is in good accordance with the results for high resistivity silicon previously reported [10].

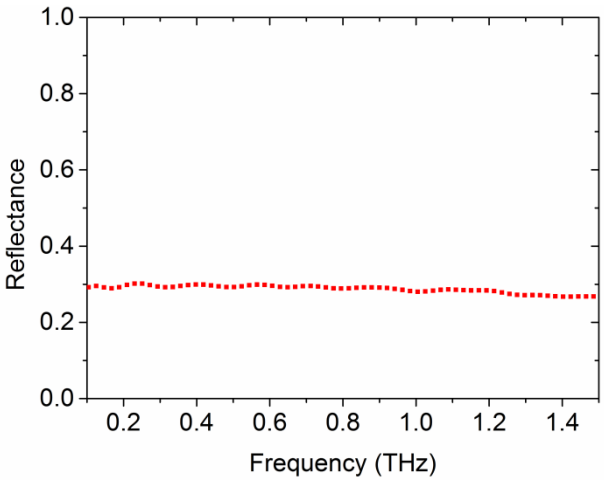

Figure 6.3 Reflectance of the *p*-type high resistivity silicon wafer from the reflection measurement

From the measured reflectance, the complex refractive index of the silicon wafer can be obtained using Eqs. (3.25) and (3.26). The refractive indices of the silicon wafer from the reflection measurement and the transmission measurement are presented in Fig. 6.4 for comparison. The value of refractive index for the transmission measurement is obtained as 3.42 in the THz frequency region between 0.1 and 1.5 THz which is excellent agreement with

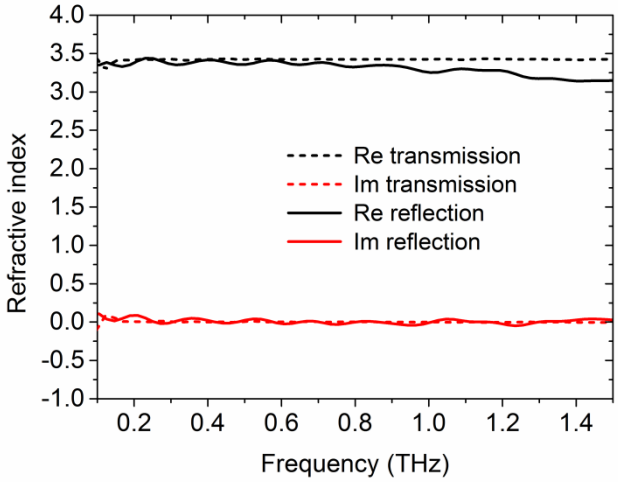

Figure 6.4: Refractive index of high-resistivity *p*-type silicon wafer from the reflection (solid line) and transmission (dash line) measurement.

reported values [12]. The refractive index for the reflection measurement is closer to the value of 3.42. However, at low frequencies (below 0.6 THz), the reported values and experimental data are in good agreement. It can be seen that the extinction coefficient for transmission measurement is good agreement with the reflection measurement. This measurement proves that the capability of the system for accurate measurements.

6.4.2 Measurements of single crystalline Si solar cell (front surface)

A similar measurement for single crystalline Si solar cell from front surface was also performed. Figure 6.5 (a) shows the reference and sample time-domain waveforms when the THz waves are reflected by the aluminum mirror and the single crystalline Si solar cell from front surface, respectively. Using the same analysis procedure used in the previous section, both the reflectance and the complex refractive index as a function of frequency were measured from the front surface of the single crystalline Si solar cell by Eqs. (3.24)-(3.26). The results are shown in Fig. 6.6. It is seen that the reflectance and refractive index of a single crystalline Si solar cell are much higher than that of the results from the silicon wafer. This may be attributed to the reflection from *p*–*n* junction of the solar cell. The emitter (*n*-region) of the solar cell is usually very thin (~0.5 μm), so that the *p*–*n* junction is close to the surface in which the THz signal is reflected from a layer surrounding the *p*–*n* junction and overlap with the reflected signal from the surface, resulting in higher reflectance. The higher reflectance resulted in higher refractive index. These results are needed to verify by developing analysis procedure considering the multiple reflections when processing the raw terahertz reflection data.

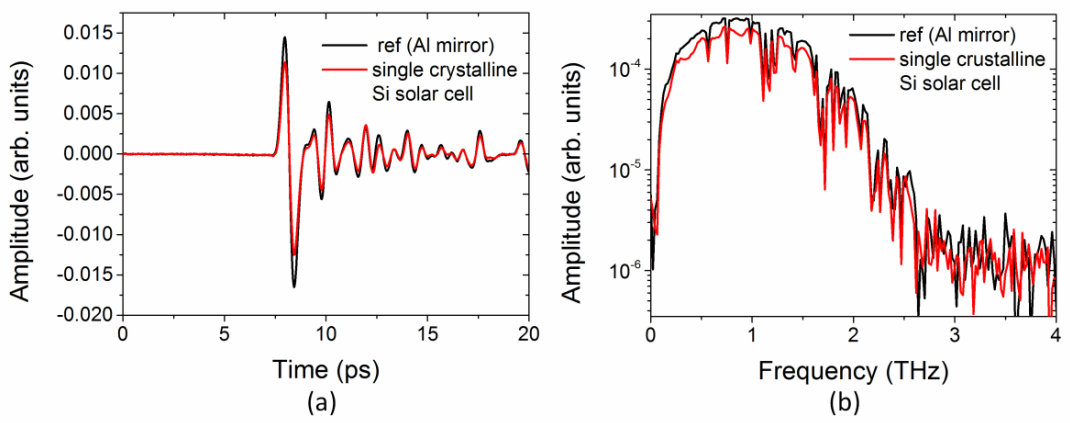

Figure 6.5: (a) Terahertz temporal waveforms of reference and single crystalline Si solar cell from front surface reflection and (b) corresponding amplitude spectra in the frequency region.

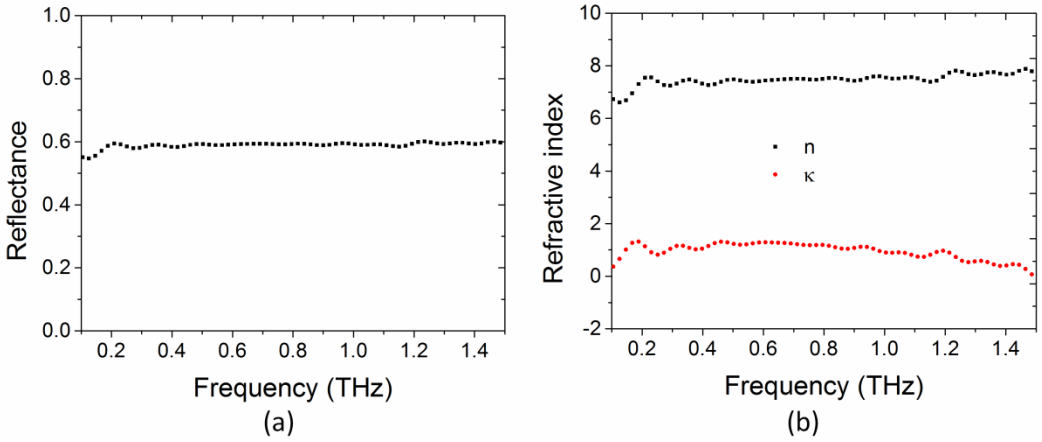

Figure 6.6: (a) Reflectance and (b) complex refractive index of single crystalline Si solar cell measured from front surface reflection.

Similar measurements were done on the solar cell under 365 nm (UV) and 800 nm (NIR) light illumination. Terahertz pulses reflected from the single crystalline Si solar cell illuminated by UV and NIR light at various powers are shown in Figs. 6.7(a) and (b), respectively. Results show that there is no significant reflection change in single crystalline Si solar cell under UV and NIR illumination.

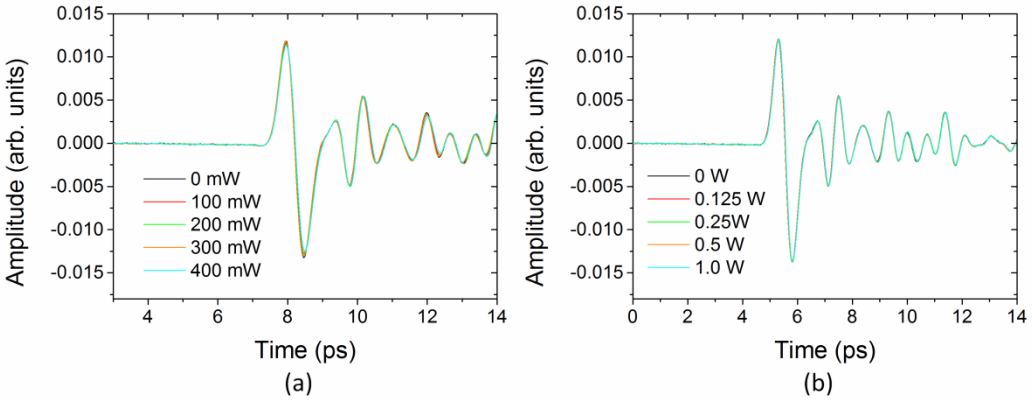

Figure 6.7: Terahertz temporal waveforms of the single crystalline Si solar cell from the front surface under (a) UV and (b) NIR light illumination. The illumination powers are listed in the figures.

6.4.3 Measurements of single crystalline Si solar cell (back surface)

Measurements were also performed on the single crystalline Si solar cell from the back surface. This sample had no metal electrodes on the back surface. The thickness of *n*-emitter and *p*-base were 0.5 μm and 188 μm, respectively. Therefore, we actually measured the THz wave reflected by the base material (*p*-type silicon) of the solar cell. In this measurement, the THz optical path was enclosed and filled with dry nitrogen to reduce absorption by water vapor in the atmosphere. The Terahertz pulses reflected from a gold mirror and back surface of single crystalline solar cell and their amplitude spectra are shown in Figs. 6.8(a) and (b), respectively. The reflectance and complex refractive index were calculated using the analytical method described in section 6.3. Figure 6.9 shows the reflectance and refractive index for base material of single crystalline Si solar cell. The average value of refractive index calculated from the experimental data is 3.37. This value is in good agreement with the value of same sample measured by transmission THz-TDS in Chapter 4.

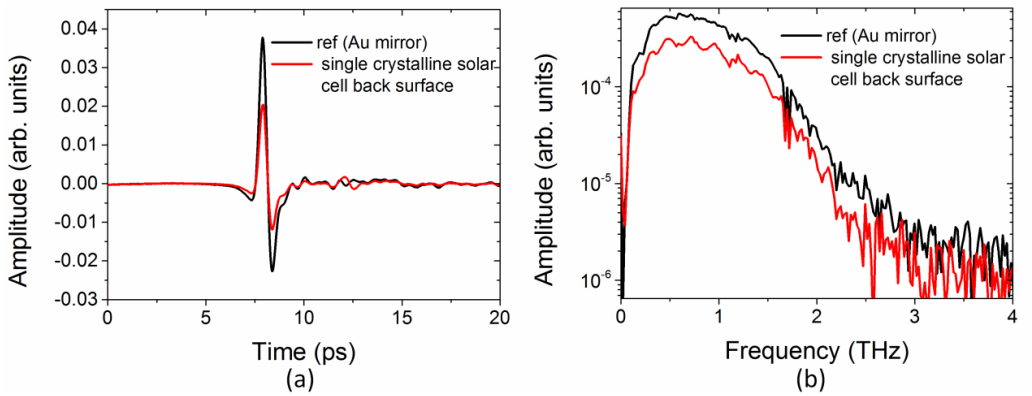

Figure 6.8: (a) Terahertz temporal waveforms of reference and single crystalline Si solar cell from back surface reflection and (b) their amplitude spectra in the frequency region.

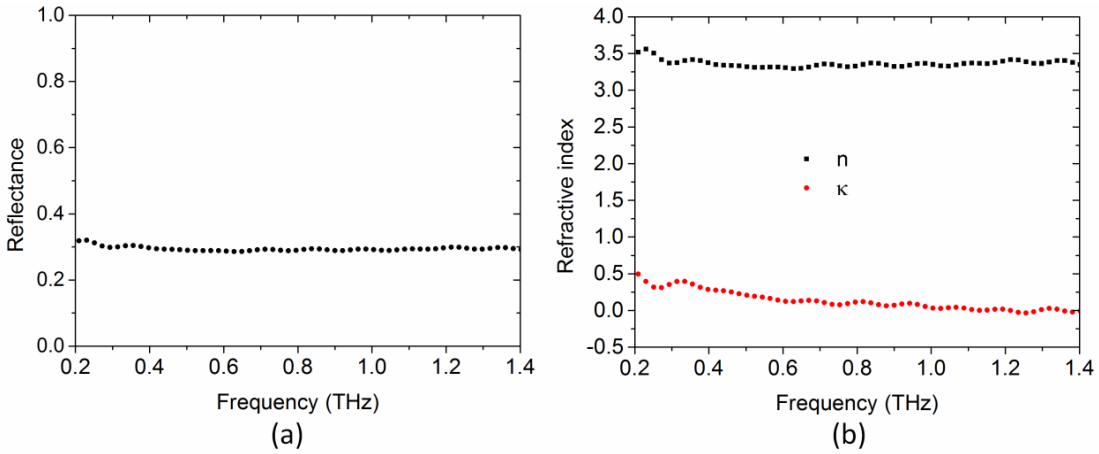

Figure 6.9: (a) Reflectance and (b) complex refractive index of single crystalline Si solar cell measured from back surface reflection.

6.4.4 Imaging of polysilicon solar cell

Terahertz reflection spectroscopic technique can be also applied for imaging of photovoltaic cells. THz reflection image can provide the structural information and detect defects in solar cells. Figure 6.10 shows the photograph of a polysilicon solar cell and the two dimensional THz reflection image of a part of the solar cell. The image in Fig. 6.10(b) mentions several futures. First, the red lines indicate thin finger electrodes which appear with high reflectivity as expected because most of metals act as nearly perfect mirror in the used THz frequencies. Also, the spaces between the electrodes clearly visualized with different reflectivity.

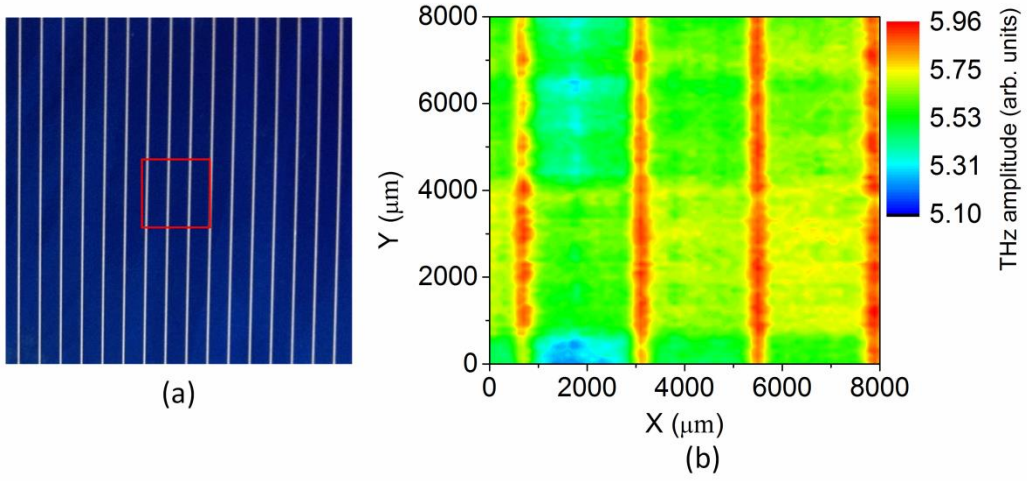

Figure 6.10: (a) Photograph of a polysilicon solar cell and (b) THz reflection image of a part of the polysilicon solar cell.

6.5 Summary

In this chapter, terahertz responses from the high resistivity silicon and crystalline Si solar cells were measured using a reflection THz-TDS with normal incidence. A special sample holder was used which allows the reflection measurements with almost no phase errors. The reflectance and refractive index of the silicon wafer, calculated from analysis of the experimental data, were in good agreement with values reported in the literature. The refractive index measured from the rear surface of the single crystalline Si solar cell was also in good agreement with the value measured by transmission THz-TDS. However, the reflectance and refractive index of single crystalline Si solar cell measured from the front surface were much higher than that of the results from the silicon wafer. This might be due to the fact that the THz signal reflected from a layer of the *p*–*n* junction overlap with the reflected signal from the surface, resulting in higher reflectance and thereby in higher refractive index. These results are needed to verify by developing analysis procedure. In the presence of UV and NIR excitation, a significant change in the THz reflection was not observed. A THz reflection image of a part of the polysilicon solar cell was also acquired which reflects the structure and the reflectivity of the polysilicon solar cell.

References

1. T. Jeon and D. Grischkowsky, "Characterization of optically dense, doped semiconductors by reflection THz time domain spectroscopy," *Appl. Phys. Lett.*, **72**, 3032 (1998).
2. L. Thrane, R. H. Jacobsen, P. Uhd Jepsen, and S.R. Keiding, "THz reflection spectroscopy of liquid water," *Chem. Phys. Lett.*, **240**, 330 (1995).
3. S. C. Howells and L. A. Schlie, "Transient terahertz spectroscopy of undoped InSb from 0.1 to 1.1 THz," *Appl. Phys. Lett.*, **69**, 550 (1996).
4. P. U. Jepsen and B. M. Fischer, "Dynamic range in terahertz time-domain transmission and reflection spectroscopy," *Opt. Lett.*, **30**, 29 (2005).
5. S. J. Oh, J. Kang, I. Maeng, J-S Suh, Y-M, Huh, S. Haam and J-H Son, "Nanoparticle enabled terahertz imaging for cancer diagnosis," *Opt. Express*, **17**, 3469 (2009).
6. S. Nashima, O. Morikawa, K. Takata, and M. Hangyo, "Measurement of optical properties of highly doped silicon by terahertz time-domain reflection spectroscopy," *Appl. Phys. Lett.*, **79**, 3923 (2001).
7. M. Khazan, R. Meissner, and I. Wilke, "Convertible transmission-reflection time-domain terahertz spectrometer," *Rev. Sci. Instrum.*, **72**, 3427 (2001).
8. A. Pashkin, M. Kempa, H. Nemec, F. Kadlec, and P. Kuzel, "Phase-sensitive time-domain terahertz reflection spectroscopy," *Rev. Sci. Instrum.*, **74**, 4711 (2003).
9. D. Hashimshony, I. Geltner, G. Cohen, Y. Avitzour, and A. Zigler, "Characterization of the electrical properties and thickness of thin epitaxial semiconductor layers by THz reflection spectroscopy," *J. Appl. Phys.*, **90**, 5778 (2001).
10. X. Wang, W. Sun and Y. Zhang, "A novel normal reflection terahertz spectrometer," *Optik*, **121**, 1148 (2010).
11. F. D. J. Brunner, A. Schneider, and P. Gunter, "A terahertz time-domain spectrometer for simultaneous transmission and reflection measurements at normal incidence," *Opt. Express*, **17**, 20684 (2009).
12. I. Pupeza, R. Wilk, and M. Koch, "Highly accurate optical material parameter determination with THz time-domain spectroscopy," *Opt. Express*, **15**, 4335 (2007).

Chapter 7: Laser terahertz emission microscope (LTEM) study on solar cell

7.1 Introduction

Laser terahertz emission microscopy (LTEM) is a THz emission imaging technique that can detect and image terahertz pulse emission from a sample excited by femtosecond laser. In this system, the sample itself is the source of THz emission and the THz emission properties such as amplitude and waveform reflects the nature of materials. It can be applied over various electronic materials such as semiconductors, high-critical-temperature superconductors, or ferroelectric materials that emit THz wave pulses when the sample is irradiated by a femtosecond laser [1–5]. The radiated THz intensity is proportional to the local electric field such as external bias field or internal static field which includes the electric field of depletion layer of Schottky junction, *p*–*n* junction, and semiconductor surface. Therefore, the amplitude of THz emission pulses can be used for mapping local electric field distribution in photoexcited materials. LTEM image reflects the dynamic behavior of photoexcited carriers that are accelerated by the local field in the materials or devices. This method has an advantage in spatial resolution to conventional terahertz wave imaging because the spot size of the excitation laser is much smaller than that of terahertz waves. Thus, it is possible to obtain a sub-micrometer order resolution. T. Kiwa et al., originally developed this technique and demonstrated for inspecting electrical faults in semiconductor integrated circuits [6]. Recently, Nakanishi et al., used this technique to generate terahertz wave emission from a solar cell and to produce terahertz-emission image of the solar cell [7]. This technique can also be applied to study charge generation, transport, and photo-response properties, such as charge carrier density, in illuminated solar cells. In this chapter, the effects of light-generated carriers and applied bias on the behavior of a solar cell were examined subjected to illumination by a continuous-wave (CW) light.

7.2 Sample

The sample used in this experiment was a commercially available polycrystalline silicon solar cell (Goldmaster & Everstep Development, open-circuit voltage: 0.5V, short-circuit current: 250 mA). The front surface was textured and covered with antireflection coating (layer of non-absorbing material with lower refractive index). It had a wide bus bar electrode and several

thinner finger electrodes on the surface, and its reverse side was covered with metal electrodes. The solar cell was protected with transparent plastic cover on the front side which was removed before the experiment. A photograph of the sample is shown in Fig. 7.1.

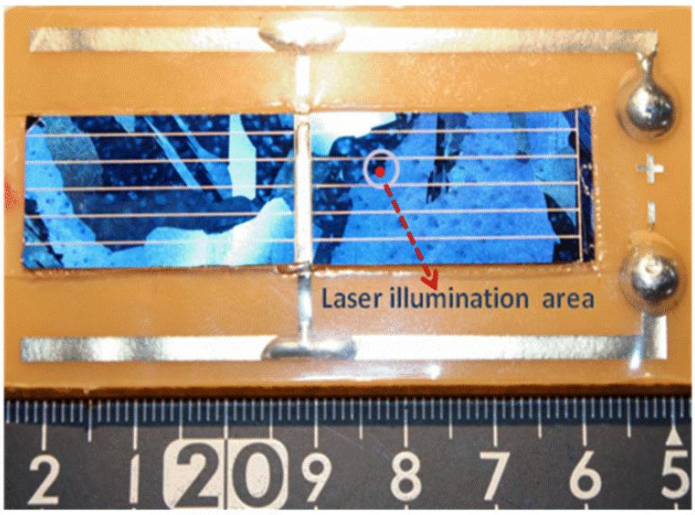

Figure 7.1: Photograph of the polycrystalline Si solar cell

7.3 Experimental procedure

A schematic of the silicon-based solar cell and the THz wave emission from the cell is shown in Fig. 7.2. When femtosecond laser pulses irradiate the solar cell with higher energy than the band gap of the solar cell material, the photoexcited carriers are accelerated by the external bias field or by the built-in electric field in the *p*–*n* junction and then decays with a time constant determined by the lifetime of the photoexcited carriers. This induces a pulsed photocurrent that emits THz radiation according to the classical formula of electrodynamics [8]:

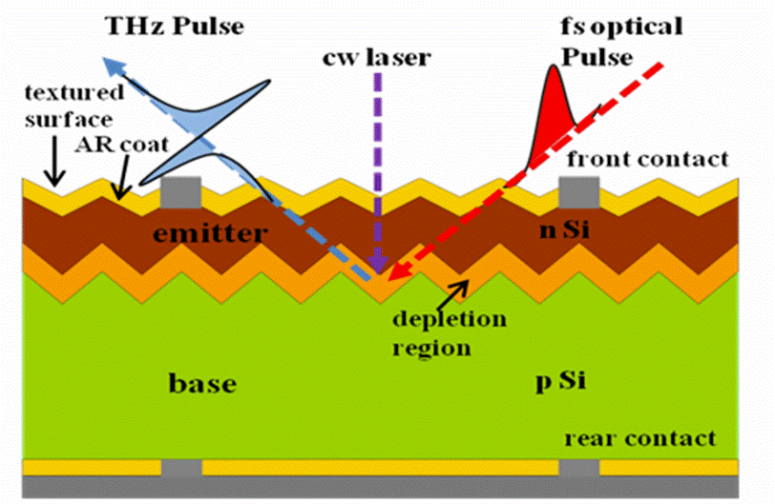

Figure 7.2: Schematic of Si based solar cell and THz wave emission from the solar cell.

$$E_{\mathrm{THz}} \propto \frac{\partial J}{\partial t} \tag{7.1}$$

where E_{THz} is the radiated electric field, J is the photo-induced current.

The experimental setup for LTEM, based on standard terahertz time-domain spectroscopy with scanning capability on the emitter side, is shown schematically in Fig. 7.3. A mode-locked Ti:sapphire laser that produced femtosecond pulses was used as the optical source, operating at a central wavelength of 800 nm, a pulse width of about 100 fs, and a repetition rate of 82 MHz. The femtosecond laser pulse was split into pump and trigger pulses using a beam splitter. The pump pulse passes through a lens and then focused onto the solar cell at an incident angle of 45° to generate THz pulse. The generated THz pulse was collimated and focused by a pair of parabolic mirrors onto the detector. A low-temperature-grown gallium arsenide spiral-type photoconductive antenna was used as the detector. The trigger pulse with an average power of 6.5 mW was excited the photoconductive antenna through an optical delay. By changing the delay and measuring the signal corresponding to each delay, the entire THz waveform can be measured. The delay stage was controlled by a computer. To obtain the THz emission image, the time delay was fixed at the maximum amplitude of the THz signal and the sample was scanned by the pump pulse using a computer-controlled *x*–*y* stage. The diameter of the pump pulse in the

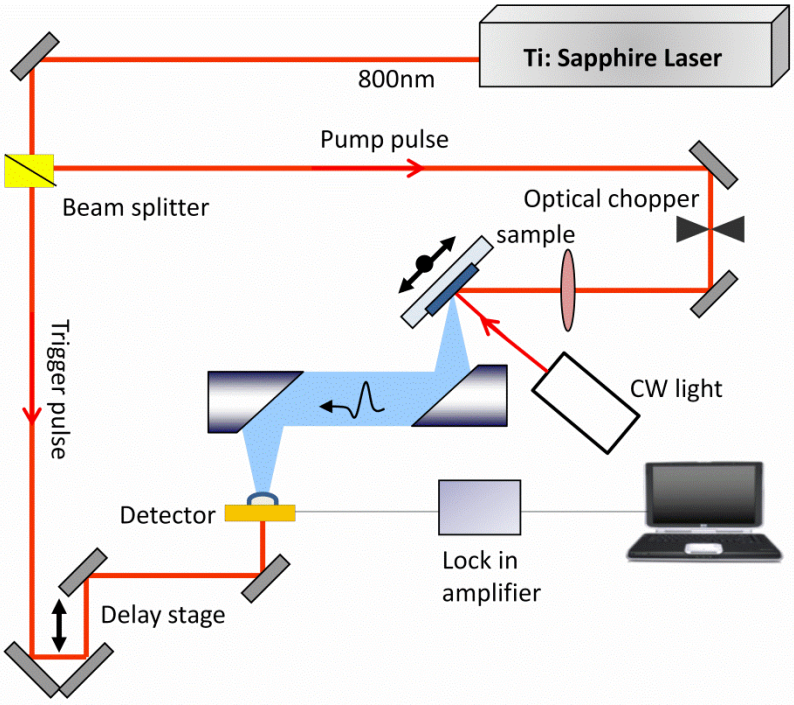

Figure 7.3: Schematic of the experimental setup for laser terahertz emission microscope (LTEM). Additional CW light is introduced on the system to excite the solar cell.

vicinity of the sample was 34 μm, as estimated by using the relationship [9]:

$$\phi = \frac{4\lambda f}{\pi D} \tag{7.2}$$

where λ is the wavelength, f is the focal length of lens, and D is the pump pulse diameter at lens position. In addition, a CW light was directed onto the system normal to the surface of the sample, and the sample was excited at wavelengths of 365 nm (UV) or 808 nm (NIR) at various powers to study the carrier dynamics at the surface and/or inside the solar cell.

7.4 Results and discussion

7.4.1 Terahertz wave emission imaging

LTEM was used to visualize THz wave emission from polycrystalline silicon solar cell illuminated by femtosecond laser. During the measurement the pump laser with an average power of 70 mW was focused at the silicon and/or crystal area on the surface of the solar cell. The time-domain waveforms of THz emission from the cell at various reverse bias voltages are shown in Fig. 7.4(a), and their fast Fourier-transformed spectra are shown in Fig. 7.4(b). The amplitude of the waveform increases with increasing the reverse bias voltage. This is because the transient photocurrent $J(t)$ driven by the electric field in the *p*–*n* junction is directly proportional to the applied bias field E_{bias} [10]. The amplitude of the waveform also depend on the pump laser intensity and increases with increasing the intensity. Figure 7.5 shows the dependence of the peak amplitude of the terahertz wave emission on the reverse bias voltage for bias voltages of 2 to 10 V. The peak amplitude of the terahertz waves depend linearly on the reverse bias voltage.

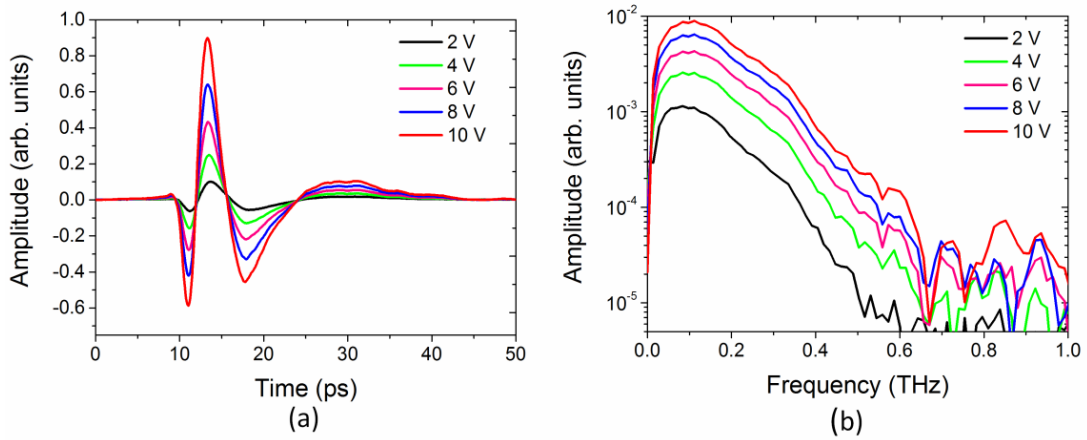

Figure 7.4: (a) Time-domain waveforms of THz emission from polysilicon solar cell at various reverse bias voltages and (b) their first Fourier-transformed spectra.

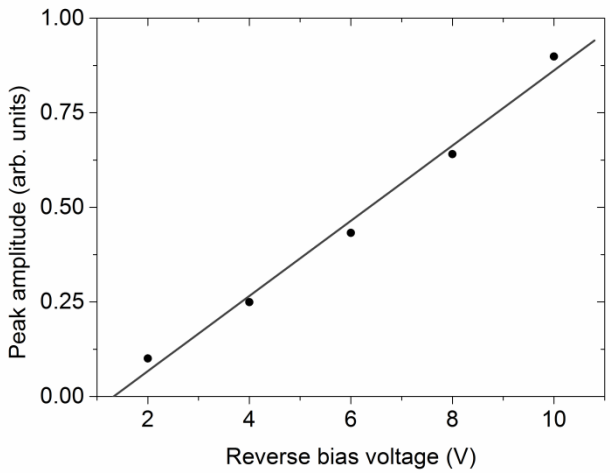

Figure 7.5: Dependence of peak amplitude of the THz wave emission from polysilicon solar cell on the reverse bias voltage for bias voltages of 2 to 10 V.

The two-dimensional THz emission image of a part of the polysilicon solar cell is shown in Fig. 7.6. The image was obtained at the pump laser power of 70 mW and a reverse bias voltage of 12V. The sample was scanned with a spatial resolution of 34 μm, and the scan area was 5×5 mm^2. The red and blue stripes represent the edges of the thin electrodes on the surface with opposite signs of THz emission amplitude which alternates with the direction of the local electric field, and near the electrodes THz emission intensity is higher than that of other area. The THz emission intensity is also stronger in the crystalline grain area, which is clearly visualized by yellow than that of the other (green) area. This result is valuable to study the dynamic behavior of photoexcited carriers in illuminated solar cells.

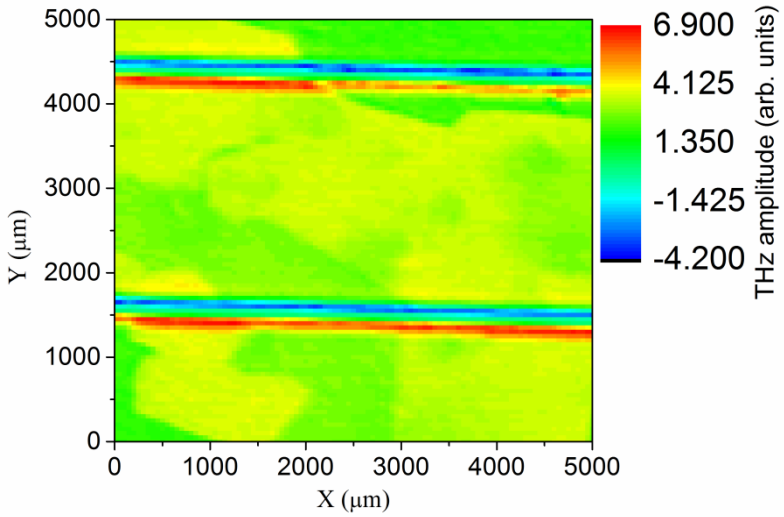

Figure 7.6: THz emission image of a part of the polysilicon solar cell. The image was obtained at the pump laser power of 70 mW and a reverse bias voltage of 12 V.

7.4.2 Measurements with 808 nm (NIR) CW laser illumination

In these measurements, femtosecond laser pump power of 30 mW and reverse bias voltage of 4 V were used to obtain THz wave emission from the solar cell. In addition to the pump laser, the sample was illuminated by NIR CW laser. The NIR laser is deeply absorbed and generates charge carriers in base (*p* region) of the solar cell. Figure 7.7(a) shows the time-domain waveforms of terahertz emission from solar cell under NIR laser illumination at various powers. It can be observed that the amplitude of the waveforms decreases with increasing NIR laser power. This is due to the fact that increased illumination power results in higher photoexcited carriers in the solar cell and thus a greater attenuation of the THz emission. The dependence of THz peak amplitude on the power of NIR illumination is shown in Fig. 7.7(b) was obtained by taking the peak amplitude of the THz wave emission at around 13 ps. Measurements were also carried out with higher reverse bias voltages (6V and 8V), and the results are presented in the same Fig. 7.7(b). The plot shows that the peak amplitude of the terahertz wave emission is inversely proportional to the power of the NIR laser.

THz emission images of the solar cell were obtained under NIR CW laser. The images were taken without and with NIR laser illumination under a reverse bias voltage of 6 V and a femtosecond laser pump power of 45 mW. The scanning area was 2.5×2.5 mm^2 and the data acquisition time was 18 minutes. Figure 7.8(a) shows an optical image of a part of the solar cell where the electrode and crystalline grain structure are visible. The two-dimensional THz emission images of the same area without and with NIR laser illumination at various powers are

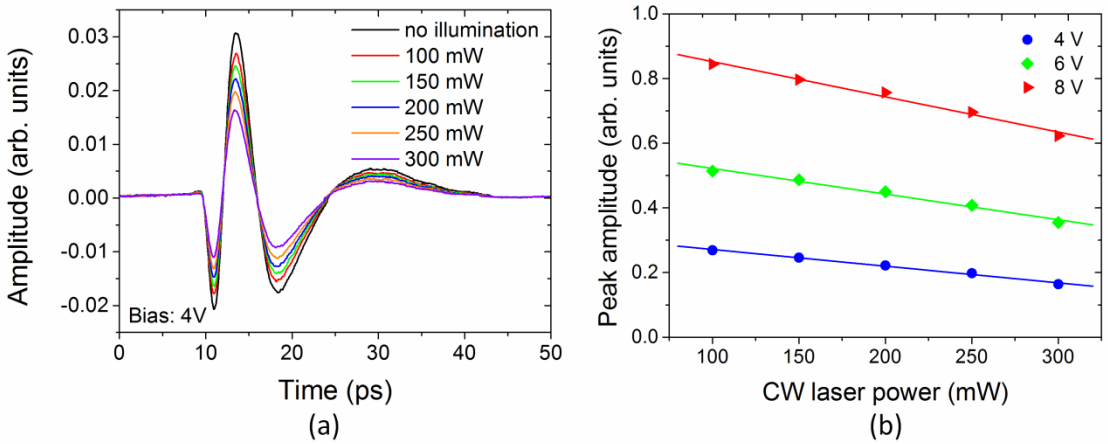

Figure 7.7: (a) Time-domain waveforms of THz wave emission from polysilicon solar cell illuminated by NIR laser at the powers of 0 to 300 mW and (b) dependence of THz peak amplitude on the power of NIR laser at different bias voltages.

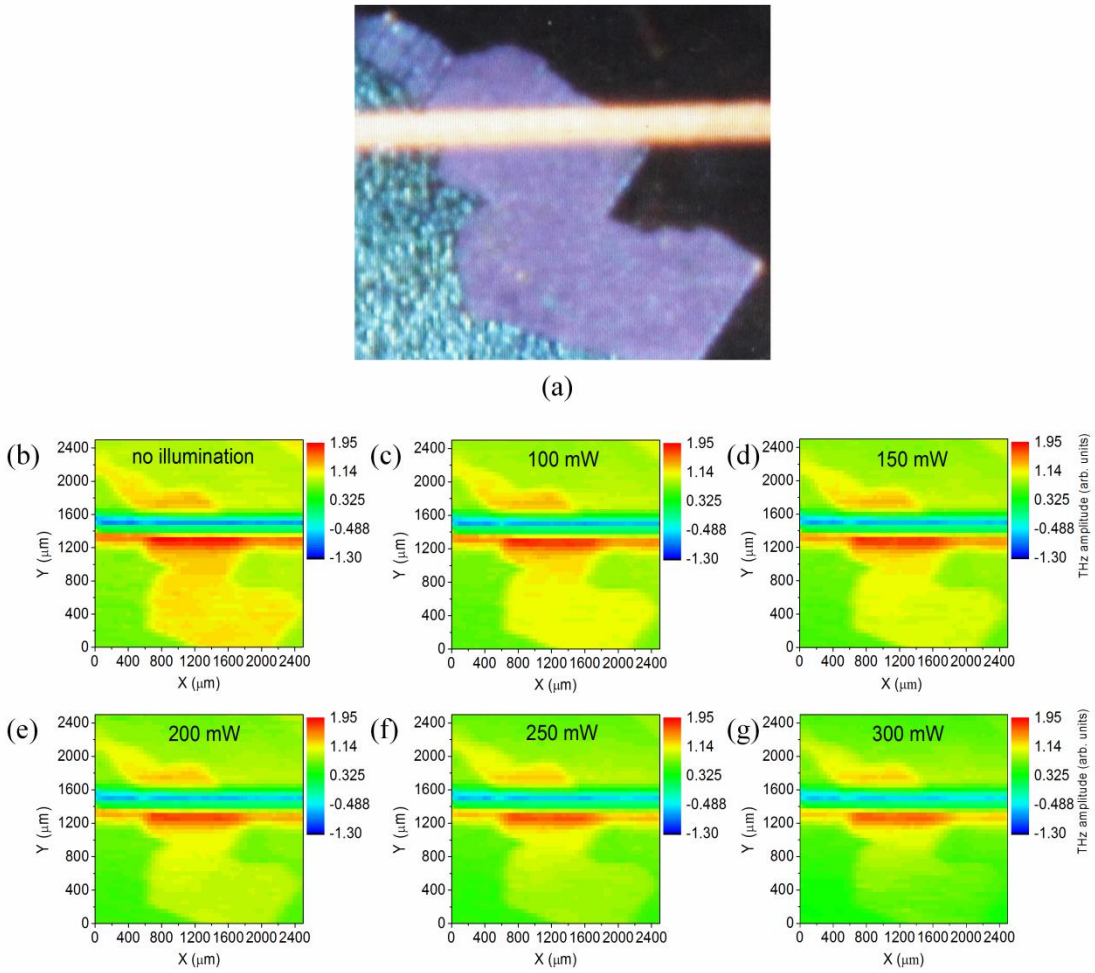

Figure 7.8: (a) Optical image of a part of the polysilicon solar cell, and THz emission images in the absence (b) and in the presence of NIR laser illumination with powers of 100 (c), 150 (d), 200 (e), 250 (f), and 300 mW (g), with a reverse bias voltage of 6 V and femtosecond laser pump power of 45 mW.

shown in Fig.7.8(b)-(g). The image in Fig. 7.8(b) clearly visualized the electrodes by red and blue stripes and the crystalline grain structure by yellow in the absence of NIR laser illumination. When the sample was illuminated by the NIR laser with a power of 100, 150, 200, 250, or 300 mW, the corresponding THz images clearly show that the terahertz emission gradually decreased with increasing illumination power [Figs. 7.8(c)–5(g)].

The above experimental results can be explained by the energy band diagram of a silicon solar cell. A common form of solar cell is the *p*–*n* junction. The energy band diagrams of *p*–*n* junction solar cell in equilibrium and under illumination are shown in Fig. 7.9. When the junction is formed, the *p*–*n* interface losses its neutrality and becomes charged due to diffusion of electrons and holes, yielding a depletion region. An inherent electric field is created by the depletion

region. This situation is shown in Fig. 7.9(a). When femtosecond laser pulse illuminates the solar cell (Fig. 7.9(b)), photons are absorbed, thus creating a number of electron-hole pairs. The *p*–*n* junction field drives the photo-generated carriers to form a transient photocurrent across the field region. The transient photocurrent generates terahertz radiation. When the *p*–*n* junction is illuminated by additional NIR laser, a large number of electron–hole pairs are generated, and the density of minority carriers is greatly increased. Minority carriers must diffuse towards the depletion region, where the inherent electric field injects them across the *p*–*n* junction. However, electrons also accumulate near the junction and create a space charge that increases the width of depletion layer and results in a decrease in the electric field in the depletion layer of the *p*–*n* junction. The decrease in the electric field results in a decrease in the amplitude of the terahertz wave emission.

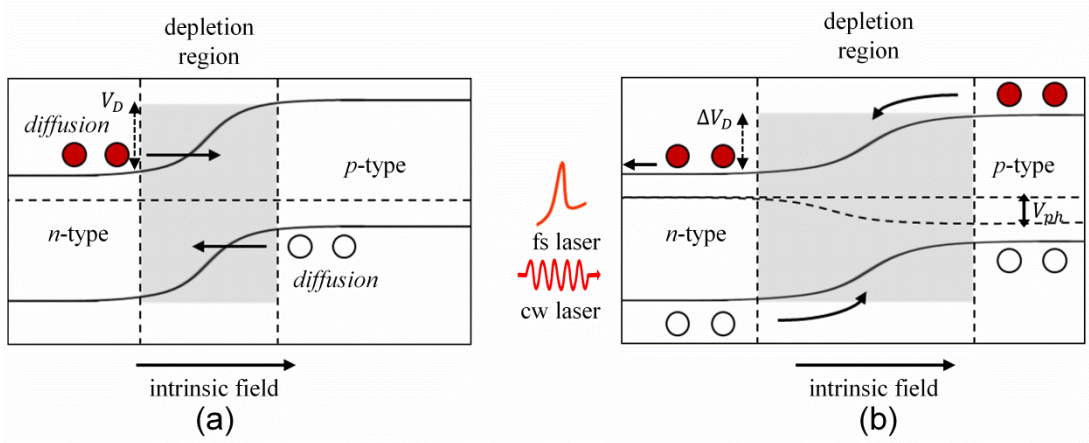

Figure 7.9: Energy-band diagrams of *p*–*n* junction solar cell (a) in equilibrium and (b) under illumination.

7.4.3 Difference of THz amplitude between 365 nm (UV) and 808 nm (NIR) light

The difference of amplitude of THz wave emission at various bias voltages in the absence and presence of UV and NIR light were investigated. The UV and NIR lights are enabled to generate charge carriers at the surface region and the base region of the solar cell, respectively. The peak amplitude of the terahertz wave emission as a function of femtosecond pump laser power at various bias voltages, with and without illumination by the UV and NIR lights, are shown in Figs. 7.10(a) and (b), respectively. Measurements were carried out at fixed illumination power of 300 mW by varying the femtosecond pump laser power at each bias voltage. The solid and dashed curves denote the amplitudes of the terahertz pulse emission in the absence and presence of illumination at various bias voltages. It can be seen that the THz peak amplitude increases

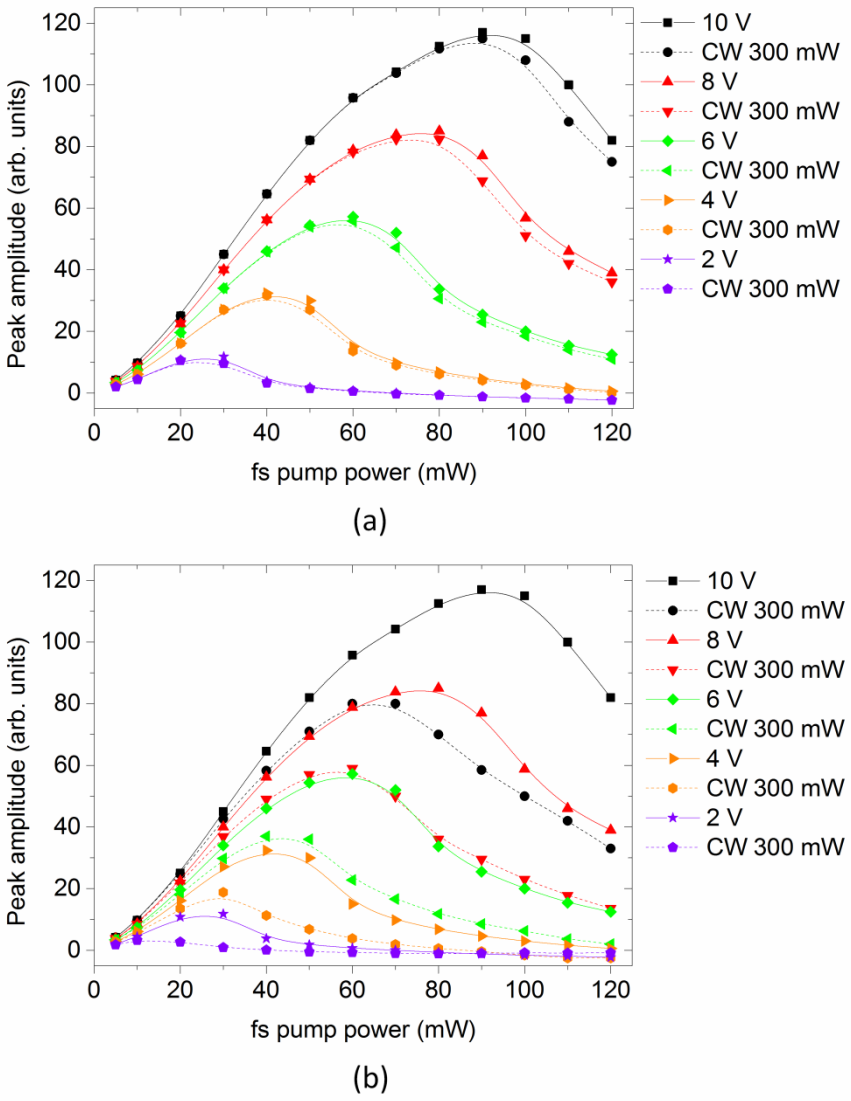

Figure 7.10: Dependence of the amplitude of THz emission from solar cell on the femtosecond laser pump power at various bias voltages in the absence and presence of (a) UV and (b) NIR light illumination. The illuminating light powers and bias voltages are shown in the figures.

with the increasing reverse bias voltages. This is because when applying reverse bias voltage, electrons and holes are pulled away from the junction, causing the width of depletion region to increase, and all the reverse bias voltage appears across the depletion region. The depletion layer widens as the junction is more reverse-biased. As a result, the inherent electric field that accelerates the photoexcited carriers increases with increasing reverse bias voltage. When the femtosecond laser pump power is increased, the terahertz emission amplitude rises up to a certain laser power and then decreased gradually with increasing laser power. At the higher pump illumination power, a large number of electron-hole pairs are generated and the photoexcited carriers are accumulated near the *p*–*n* junction region where they screen each other.

As a result, the electric field in the depletion layer of the junction is reduced. Due to this screening effect, the THz emission amplitude decreases at even higher laser powers. It is also seen from Fig. 7.10(b) that the amplitude of THz wave emission is greatly reduced by NIR illumination. However, under UV light illumination, the amplitude of THz wave emission decreased very slightly (Fig.7.10 (a)) compare to the NIR illumination. These changes are related to number of free carriers in the solar cell and can be explained by considering the penetration depth of the two wavelengths of light.

In semiconductor, the excess carrier density, Δn, is directly related to the carrier lifetime, τ, as described by the expression[11]:

$$\Delta n = G\tau\,, \tag{7.3}$$

where G is the rate of generation of carriers, which can be calculated by using the following expression [11]:

$$G = \Phi(1-R)\frac{1}{\delta}\,' \tag{7.4}$$

where Φ is the photon flux defined as the number of photons per unit time per unit area, δ is the penetration depth of illumination light, and R is the reflectance. The reflectance for normal incidence at an interface between two media of refractive index n_1 and n_2 is defined as follows [12]:

$$R = \left(\frac{n_1 - n_2}{n_1 + n_2}\right)^2 \tag{7.5}$$

An estimation of the photoexcited carrier density at various illumination powers can be made from typical parameters for silicon material, as shown in Table 7.1. The carrier generation rates for 1 mW at UV and NIR light are estimated to be 1.1×10^{21} $cm^{-3}s^{-1}$ and 2.3×10^{19} $cm^{-3}s^{-1}$ respectively. Although the carrier generation rate is higher for UV light, the change in amplitude of THz emission is much smaller than that for NIR light, as can be clearly seen in Figs. 7.10(a) and (b). This behavior can be explained by considering the carrier generation at different depth in the solar cell illuminated by UV and NIR lights. In case of UV illumination, the photoexcited carriers are generated within a penetration depth of 0.01 μm from the surface of the solar cell, and their lifetime must be strongly influenced by the surface recombination effect. The effective carrier lifetime [13] τ_{eff} can be written as follows:

$$\frac{1}{\tau_{\text{eff}}} = \frac{1}{\tau_{\text{bulk}}} + \frac{1}{\tau_{\text{surf}}} \tag{7.6}$$

where τ_{bulk} and τ_{surf} are the lifetime of carriers generated in the bulk and at the surface region, respectively. The value of τ_{surf} can be expressed as follows [13]:

$$\tau_{\mathrm{surf}} = \frac{d}{2S} \tag{7.7}$$

where S is the surface recombination velocity and d is the thickness of the layer in which the carriers exist. In this experiment, the penetration depth δ can be regarded as being equal to d that is 10^{-6} cm for UV light. The surface recombination velocity is largely dependent on the surface conditions, and an exact value for the sample that used in this experiment cannot measure. However, even if quite a low recombination velocity ($S \approx 10\ \mathrm{cms}^{-1}$) is realized by means of a high-quality passivation layer on the surface, the surface lifetime τ_{surf} will be of the order 10^{-7}, as estimated by Eq. (7.7); this value is much smaller than τ_{bulk}.

Table7.1: Typical material parameters of silicon used in the estimation of the carrier generation rate and the photocarrier density. The diffusion lengths of the *n*-type and *p*-type silicon in the solar cell are 14 and 140 μm, respectively [14].

Parameters	365 nm (UV)	808 nm (NIR)
Spot size, φ (mm)	10	3
Refractive index, n [15]	6.5	3.67
Reflectance, R (%)	54	33
Absorption coefficient, α (cm^{-1}) [15]	9.5×10^{5}	6.06×10^{2}
Penetration depth, δ (μm)	0.01	16.5
Carrier generation rate, G for 1 mW ($\mathrm{cm}^{-3}\mathrm{s}^{-1}$)	1.1×10^{21}	2.3×10^{19}

On the other hand, the penetration depth of NIR light is 16.5 μm, which is much greater than the typical thickness of a solar cell emitter (~ 0.5 μm), and therefore the effect of surface recombination is reduced. Therefore, consider that the density of excess carriers, as estimated by Eq. (7.3), when the solar cell is illuminated by the UV light will be less than that when it is illuminated by the NIR light, and that this reduced density of excess carriers is responsible for the smaller change in the terahertz radiation intensity.

7.4.4 Measurements under nonbiased condition

Measurements were performed on the same sample under zero-bias voltage without electrical contacts. In this case, the excitation pump laser was operating at a low power 3 mW and generates THz wave emission due to inherent electric field in the *p*–*n* junction, although the intensity is very low compared to bias conditions results. In addition to the pump laser, the sample was illuminated by the UV light at powers of 75, 150, 225, 300, and 375 mW. The time-domain waveforms of the terahertz emission from solar cell and their frequency spectra in the absence and presence of UV illumination are shown in Fig. 7.11. A difference in the THz peak amplitudes in the presence and absence of illumination could clearly be seen, even with the UV light. Note that any terahertz emission under illumination by the NIR laser could not observed, suggesting that the effect of the NIR laser illumination is enhanced when the power of the femtosecond pump laser is very low.

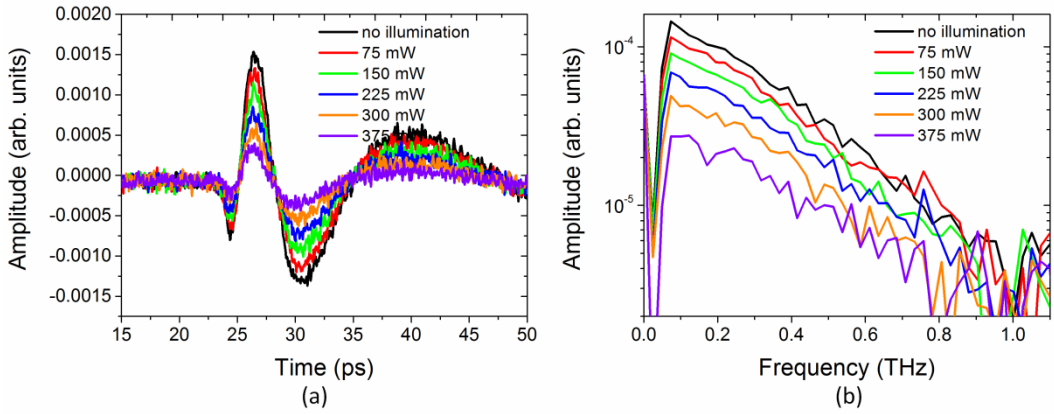

Figure 7.11: (a) Time domain waveforms of terahertz wave emission from the solar cell and (b) their frequency spectra in the absence of a bias voltage, and in the presence and absence of UV light illumination.

THz emission images of the solar cell were also obtained under zero bias without electrical contacts. Figure 7.12 shows the THz emission images of the polysilicon solar cell without and with UV light illumination. The images were recorded without and with UV light with illumination power of 75 mW under the femtosecond laser pump power of 3 mW. The image without UV illumination in Fig. 7.12(a) also clearly reflects the electrode and crystalline grain structure and the distribution of the electric field in the solar cell. Under illumination by UV light, the image in Fig. 7.12(b) shows the loss of THz emission intensity due to the presence of photoexcited carriers in the depletion layer of the *p*–*n* junction. The above results are important in relation to the practical application of LTEM as an inspection technique for solar cells,

because the results show that it might be feasible to perform measurements without electrical contacts by using LTEM.

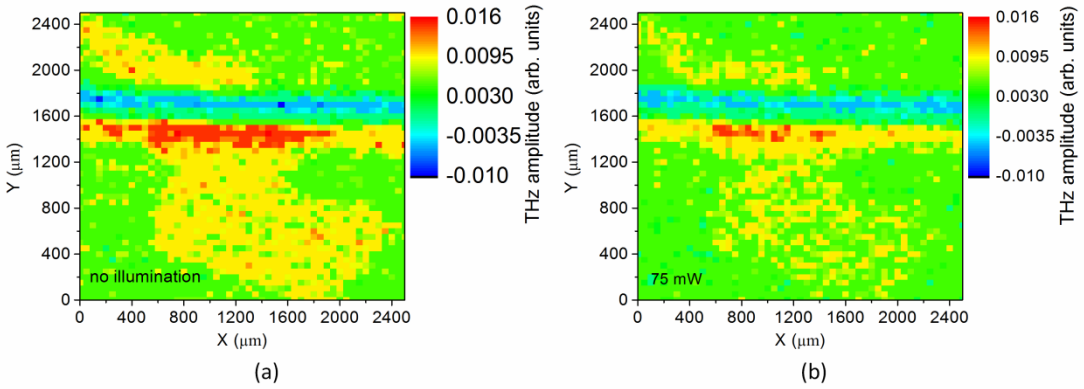

Figure 7.12: THz emission images of a part of polysilicon solar cell (a) in the absence and (b) in the presence of UV light illumination with power of 75 mW under zero bias.

7.5 Summary

Terahertz wave emission properties of a polysilicon solar excited by femtosecond laser pulses were visualized by LTEM. The effects on terahertz emission from the solar cell illuminated by CW UV and NIR lights were examined under conditions of reverse and zero bias. The results showed that the amplitude of terahertz wave emission was attenuated in the presence of illumination by UV or NIR light. The images of the solar cell also clearly showed that the THz emission gradually decrease with increasing illumination powers. These changes were related to the numbers of photoexcired carriers in the solar cell and were explained by the band structure of the illuminated solar cell. At high excitation pump laser (femtosecond laser) powers, the amplitude of the THz emission was decreased with increasing laser powers. This phenomenon was explained by the screening of the electric field (screening effect) in the depletion layer of the *p*–*n* junction as a result of the presence of photoexcited carriers. The amplitude of THz emission depends on the wavelength of the illumination light and smaller for UV light than that for NIR light was observed. These changes were explained by considering the penetration depth of the two wavelengths of illumination light. THz emission image under zero bias without electrical contacts was also obtained. These findings indicate that LTEM might be useful technique for the evaluation and inspection of solar cells.

References

1. M. Yamashita, K. Kawase, C. Otani, T. Kiwa, M. Tonouchi, "Imaging of large-scale integrated circuits using laser-terahertz emission microscopy," *Opt. Express*, **13**, 115, (2005).
2. M. Hangyo, S. Tomozawa, Y. Murakami, M. Tonouchi, M. Tani, Z. Wang, K. Sakai, and S. Nakashima, "Terahertz radiation from superconducting $YBa_2Cu_3O_{7-\delta}$ thin films excited by femtosecond optical pulses," *Appl. Phys. Lett*., **69**, 2122 (1996).
3. K. Takahashi, N. Kida and M. Tonouchi, "Terahertz radiation by an ultrafast spontaneous polarization modulation of multiferroic $BiFeO_3$ thin films," *Phys. Rev. Lett.*, **96**, 117402 (2006).
4. H. Murakami and M. Tonouchi, "Laser terahertz emission microscopy," *C. R. Phys*., **9**, 169 (2008).
5. N. Kida and M. Tonouchi, "Terahertz radiation from magnetoresistive $Pr_{0.7}Ca_{0.3}MnO_3$ thin films," *Appl. Phys. Lett*., **78**, 4115 (2001).
6. T. Kiwa, M. Tonouchi, M. Yamashita and K. Kawase, "Laser terahertz-emission microscope for inspecting electrical faults in integrated circuits," *Opt. Lett.*, **28**, 2058 (2003).
7. H. Nakanishi, S. Fujiwara, K. Takayama, I. Kawayama, H. Murakami, M. Tonouchi, "Imaging of a polycrystalline silicon solar cell using a laser terahertz emission microscope," *Appl. Phys. Express*, **5**, 112301 (2012).
8. K. Sakai (Ed.), *Terahertz Optoelectronics* (pp. 70), Berlin: Springer (2005).
9. M. Tonouchi, N. Uchida, S. Kim, R. Inoue, H. Murakami, "Laser terahertz emission microscope," *Terahertz Science and Technology*, **1**, 28 (2008).
10. M. R. Stone, M. Naftaly, R. E. Miles, J. R. Fletcher, D. P. Steenson, "Electrical and radiation characteristics of semi large photoconductive terahertz emitters," *IEEE Trans. Microwave Theory Tech*., **52**, 2420 (2004).
11. S.M. Sze, *Physics of Semiconductor Devices*, 3nd edition, p.726, J. Wiley & Sons (1981).
12. S. O. Kasap, *Principles of Electronic Materials and Devices*, Tata McGraw-Hill, Special Indian Edition (2007).
13. Y. Arafat, F. M. Mohammedy, and M. M. S. Hassan, "Optical and other measurement techniques of carrier lifetime in semiconductors," *Int. J. Optoelect. Eng.*, **2**, 5 (2012).
14. J. Nelson, *The Physics of Solar Cells*, London: Imperial College Press (2003).
15. M. H. Jones and S. H. Jones "Optical Properties of Silicon", http://www.univie.ac.at/photovoltaik/vorlesung/ss2014/unit4/optical_properties_silicon.pdf

Chapter 8: Conclusions

In this thesis, the optical properties and the dynamics of photoexcited carriers in silicon and silicon-based solar cells have been studied using THz spectroscopy and imaging techniques. The charge carriers in the samples were generated by 800 nm near infrared (NIR) and 365 nm ultraviolet (UV) continuous-wave (CW) light. The photoexcited carriers affect a number of material parameters such as complex refractive index, conductivity, and mobility. The lifetime and surface recombination velocity (SRV) of photoexcited carriers also affect the overall performance of a solar cell. Working conditions for the solar cell was simulated by illumination with CW light, and the different material parameters were then examined without the need of electrical contacts using THz-TDS. The dynamic behaviors of photoexcited carriers in solar cell under CW light were also inspected using LTEM. Three THz experimental systems were constructed to achieve this goal. The major experimental results of this work are summarized below:

Transmission THz-TDS was used to investigate the optical properties of single crystalline solar cells (semi-finished) with and without AR-coating layer during photoexcitation by NIR and UV light. NIR and UV light generate charge carriers in the base (*p* region) and in the emitter (*n* region) of the solar cell, respectively. In the case of NIR excitation, the transmission in both samples was greatly reduced by the absorption of the photoexcited carriers. By analyzing the transmission data, the complex refractive index and complex conductivity were determined. In both samples, Drude model was used to analyze the conductivity data in the THz frequency range. From the fitting results, the excess carrier density and mobility were extracted. The excess carrier density was higher for AR coating sample because the AR coating increases the absorption of light by reducing the reflection. In both samples with and without AR coating layer, the mobility of the excess carriers increases nonlinearly with the illumination power and tends to saturate at higher illumination power for NIR laser. This phenomenon was explained by the carrier trapping effect in the impurity region in the bandgap of the solar cell. For UV light illumination, the transmission of the sample was only slightly reduced due to short carrier lifetime affected by the surface recombination. The difference in the measured response of the samples was explained by the difference in the penetration depth of the NIR and UV light.

Using similar experimental system and conditions, the minority carrier lifetime and SRV in silicon were investigated. In this measurement, excess carriers generated by UV light at the

surface region were considered as the surface carrier density, and then SRV on this density was extracted using the SRH model. The SRV observed on the silicon surface was greatly reduced and depends strongly on the excess carrier density at the surface region, which means that UV illumination passivates the surface of the silicon wafer. This phenomenon was explained with the energy band diagram of the silicon wafer under UV light illumination. On the other hand, the NIR light has longer penetration depth and generates charge carriers in the bulk and is therefore less sensitive to the surface states. The effective lifetime of the excess carriers was calculated under steady state conditions and was found to be ~10^{-7} seconds and depends strongly on the excess carrier density.

The finished single crystalline Si solar cell and thick silicon are opaque to the THz radiation. The optical properties of these samples were measured using reflection THz-TDS. In the time-domain THz reflectivity measurement, the common problem is that the phase error due to the misplacement of the reflected reference or sample surface. The phase error leads to the large error in the calculated optical constants. To overcome this problem, a special movable sample holder was used in which the position of the reference mirror and the sample were changed using a computer controlled *x*-*y* stage. This sample holder allowed the measurement of reflected THz waves with almost no phase errors. The reflectance and the refractive index of high resistivity doped silicon were in good agreement with the reported values. On the other hand, the reflectance and the refractive index measured from the front surface of the single crystalline Si solar cell were much higher than that of silicon results. This might be due to the fact that the THz signal reflected from a layer of the *p*–*n* junction overlap with the reflected signal from the surface, resulting in higher reflectance and thereby in higher refractive index. These primary results are needed to verify by developing analysis procedure considering the multiple reflections when processing the raw THz reflection data. Measurements were also carried out on the solar cell illuminated by NIR and UV light and a significant change in the THz reflection was not observed. These results indicate that the reflection THz-TDS might not suitable for the study of photoexcited carrier in solar cells. THz reflection image of a part of the solar cell was also acquired using this system.

Next, laser terahertz emission microscope (LTEM) was employed to visualize THz wave emission properties of a polysilicon solar cell when illuminated by a femtosecond laser. The THz wave emission properties such as amplitude and waveform reflect the nature of the solar cell. The effects on the THz wave emission from the solar cell illuminated by additional NIR and UV CW light were also examined under reverse bias and zero bias. In the absence of CW

light illumination, the amplitude of the THz wave emission from the solar cell increased with increasing reverse bias voltage. This was because the transient photocurrent driven by the electric field of the *p–n* junction is directly proportional to the external bias field. The THz emission image showed that the crystalline grain structure, electrodes and also visualized the local electric field distribution in the solar cell. Under NIR illumination, the amplitude of the THz wave emission was decreased with the illumination power. The images of the solar cell also clearly showed that the THz wave emission gradually decreased with increasing illumination power. These changes were due to the photoexcited carriers in the solar cell, and were explained using the band structure of the illuminated solar cell. At high excitation laser (femtosecond laser) powers, the screening of the electric field (screening effect) in the depletion layer of the *p–n* junction was observed. In the presence of UV light illumination, the amplitude of the THz wave emission was smaller compared to the NIR light illumination. The wavelength dependence of THz wave emission was explained by considering their penetration depth. Similar results were also obtained in the presence of UV light under zero bias voltage without electrical contacts. These results prove the practical applications of LTEM for solar cell studies.

The findings in the above experiments suggest that THz-TDS and LTEM are promising techniques for the evaluation and inspection of solar cells and related materials without electrical contacts at the beginning, during the fabrication process, as well as for finished solar cells.

Achievements

Journal papers

1. K. A. Salek, I. Kawayama, H. Murakami and M. Tonouchi, "Evaluation of solar cell using terahertz time domain spectroscopy," *Physical Science International Journal*, Vol. **6**, No. 2, 96-102 (2015).
2. Y. Sano, I. Kawayama, M. Tabata, K. A. Salek, H. Murakami, M. Wang, R. Vajtai, P. M. Ajayan, J. Kono, and M. Tonouchi, "Imaging molecular adsorption and desorption dynamics on graphene using terahertz emission spectroscopy," *Scientific Report*, Vol. **4**, No. 6046, 1-5 (2014).
3. K. A. Salek, K. Takayama, I. Kawayama, H. Murakami and M. Tonouchi, "Evaluation of surface carrier recombination of optically excited silicon using terahertz time-domain spectroscopy," *Terahertz Science and Technology*, Vol. **7**, No. 2, 100-107 (2014).
4. K. A. Salek, H. Nakanishi, A. Ito, I. Kawayama, H. Murakami and M. Tonouchi, "Laser terahertz emission microscopy studies of a polysilicon solar cell under the illumination of continuous laser light," *Optical Engineering*, Vol. **53**, No. 3, 0312041-6 (2014).

International conferences

1. K. A. Salek, K. Takayama, I. Kawayama, H. Murakami and M. Tonouchi, "Surface carrier recombination of optically excited silicon studied by terahertz time-domain spectroscopy," The 10th conference on Lasers and Electro-Optics Pacific Rim (CLEO-PR 2013), WPC-6, Kyoto, Japan (Jun. 30-July 4, 2013).
2. K. A. Salek, H. Nakanishi, I. Kawayama, H. Murakami and M. Tonouchi, "Terahertz radiation from solar cell observed by Laser Terahertz Emission Microscope," Terahertz dynamics in carbon based nanostructures, Poster, Dresden, Germany (Mar. 5-7, 2012).
3. K. A. Salek, H. Nakanishi, A. Ito, I. Kawayama, H. Murakami and M. Tonouchi, "Laser terahertz emission microscopy studies of a polysilicon solar cell illuminated by continuous laser light," 3rd International Workshop on Terahertz Nanoscience (TeraNano III), P-17, Hawaii, USA (Dec. 10-12, 2012).
4. K. A. Salek, K. Takayama, I. Kawayama, H. Murakami and M. Tonouchi, "Surface carrier recombination of optically excited silicon," International Workshop on Optical Terahertz Science and Technology (OTST 2011), MF19, Santa Barbara, USA (Mar. 13-17, 2011).

5. K. A. Salek, K. Takayama, I. Kawayama, H. Murakami and M. Tonouchi, " Evaluation of characteristics of photoexcited silicon wafer by terahertz time-domain spectroscopy," 2nd Global COE Student Conference on Innovative Electronic Topics (SCIENT 2010), Po-5, Osaka, Japan (July 28-29, 2010).
6. K. A. Salek, R. Kinjo, K. Asahi, I. Kawayama, H. Murakami and M. Tonouchi, "Terahertz time-domain spectroscopy for $SrRuO_3$ thin films," International Workshop on Terahertz Technology (TeraTech 2009), 2P-51, Osaka, Japan (November 30- December 3, 2009).
7. K. A. Salek, R. Kinjo, K. Asahi, I. Kawayama, H. Murakami and M. Tonouchi, "Evaluation of characteristics of $SrRuO_3$ thin films in a THz frequency region," 5th Handai Nanoscience and Nanotechnology International Symposium, P2-41, Osaka, Japan (September 1-3, 2009).

National conferences

1. K. A. Salek, Y. Sano, I. Kawayama, H. Murakami, M. Wang, R. Vajatai, J. Kono, P. M. Ajayan, M. Tonouchi, "Effect of CW light illumination on terahertz emission from Graphene-coated InP, The Japan Society of Applied Physics (JSAP), Autumn meeting, Kyoto, Japan (Sep. 16-20, 2013).